Fundamental Study on Wide-Bandgap-Semiconductor MEMS and Photodetectors for Integrated Smart Sensors

February 2013

Naoki WATANABE

Electronic Science and Engineering
Kyoto University

Abstract

During the past several decades, microelectromechanical systems (MEMS) have attracted much attention and have had major impacts on vast fields. A large number of MEMS devices have been utilized in many environments, and the use in harsh environments characterized as locations of high temperature, high pressure, strong radiation, and corrosive environments have come to be required. An increasing demand for MEMS that can operate in harsh environments stimulated the search for new structural materials. The promising candidates of the material for harsh-environment MEMS are wide bandgap semiconductors, e.g., silicon carbide (SiC) and group-Ⅲ nitrides such as gallium nitride (GaN), because of their superior mechanical strength and chemical inertness in harsh environments. Electrical properties of wide bandgap semiconductors are excellent as well, leading to high-temperature operation of semiconductor-based sensor devices such as photodetectors. The combination of excellent electrical and mechanical properties offers many opportunities for using the wide bandgap semiconductors as a material for integrated sensor systems of MEMS and semiconductor devices in applications featuring harsh environments. On the other hand, the utilization of wide bandgap semiconductors can also introduce new functions in MEMS. The wide bandgap semiconductors have excellent functionalities, e.g., visible-range transparency which is one of the unique characteristics of the wide bandgap semiconductors, enabling to realize novel optical MEMS devices. Moreover, by combining such novel optical MEMS with wide-bandgap-semiconductor sensor devices, high functional and high performance "smart" devices can be realized.

However, there are few investigations on this field. To realize the integrated smart sensors and the monolithically integrated sensor systems operating up to high temperature, it is necessary to investigate the material properties of constituent materials up to high temperature, fabrication process of microstructures in wide bandgap semiconductors, and device fabrication and characterization of wide-bandgap-semiconductor MEMS and sensors. In this thesis, three main topics are extensively investigated: 1) determination of the optical properties of SiC, GaN, and AlN from room temperature (RT) to very high temperature, 2) investigation on SiC micromachining process and fabrication of all-single-crystalline SiC MEMS devices, and 3) investigation on high-temperature operation of SiC pn photodiodes.

In Chapters 2 and 3, temperature dependence of the optical properties of SiC, GaN, and aluminum nitride (AlN) up to high temperature is described. In Chapter 2, the author

determines the thermo-optic coefficients, i.e., the temperature dependence of the refractive indices, of SiC, GaN, and AlN up to 500°C over a wide spectral range from infrared (1700 nm) to ultraviolet near the bandgaps of those materials (392 nm for SiC, 367 nm for GaN, and 217 nm for AlN), toward realizing wide-bandgap-semiconductor-based tunable optical filters. The author also carries out optical simulation of a GaN-based tunable filter at RT and 500°C by using the refractive indices and the thermo-optic coefficients of GaN and AlN obtained in this study, demonstrating that the modulation of the transparent wavelength of the filter is suitable for tunable filter application. In Chapter 3, determination of temperature dependence of the absorption coefficient of SiC for device design of SiC photodetectors at high temperature is presented. The temperature dependence of the absorption coefficient of SiC is determined precisely in wide range of wavelength based on the optical transmission measurement.

In Chapter 4, fabrication process of SiC MEMS devices and demonstration of all-single-crystalline SiC MEMS devices are presented. The author describes the device design of SiC MEMS and fabrication process including reactive ion etching process of for device patterning and photoelectrochemical (PEC) and electrochemical (EC) etching processes for doping-type selective etching, which can realize sacrificial-layer process. Suspended SiC bridge structures using PEC etching are fabricated. The bridge has a sub-micron gap between the bridge and the bottom. The width w, the length l, and the thickness d of the bridges are 4-10 μm, 50-200 μm, and 100 nm, respectively. Electrostatic actuation of the bridge is demonstrated by applying bias voltage of 20 V. SiC cantilever structures are also fabricated with EC etching, and resonance characteristics of fabricated devices are investigated. The dimensions of the cantilevers are w = 15 μm, l = 80-140 μm, and d = 900 nm. The SiC cantilever shows extremely high quality factor about 230,000, demonstrating the advantage of all-single-crystalline SiC MEMS devices, leading to high-sensitivity sensors.

In Chapter 5, high-temperature operation of SiC pn photodiodes is investigated. This chapter includes two parts: 1) detailed study on the temperature dependence of the photoresponse and 2) investigation on the electrical characteristics of fabricated pn photodiodes up to 600°C. For the investigations, the author fabricates mesa-type 4H-SiC pn photodiodes with the device area from 0.09 to 4 mm^2. In the first part, the author demonstrates that the device shows small temperature dependence at certain wavelength illumination and that the targeted wavelength can be adjusted on the same device by controlling the reverse-bias voltage. In the second part, the author shows the origin of the reverse leakage current of fabricated devices and reduction of the leakage current by inventing the surface passivation process. By employing the passivation process of dry thermal oxidation followed by nitric oxide annealing, which is utilized to reduce interface trap density for SiC metal-oxide-semiconductor field-effect transistors, the leakage current of SiC pn diodes is significantly reduced by a factor of 20, compared with conventional surface passivation. Finally, the author successfully demonstrates the operation of the photodiode up to 500°C.

In Chapter 6, conclusions of this study and suggestions for future work are presented.

Acknowledgements

The study presented in this thesis was done at Kyoto University in Japan, where I did my Ph.D. studies. I owe very important debt to many people who have supported and encouraged me in various ways during that time, and I am deeply grateful to all of them. First of all, I would like to express my deepest gratitude to Professor Tsunenobu Kimoto for providing me the opportunity to accomplish this work and for his supervision, continuous guidance, invaluable advice, and ceaseless encouragement through fruitful discussions. I would particularly like to appreciate to Associate Professor Jun Suda for his continuous guidance concerning experimental details, helpful suggestions, and constructive discussions as well as constant encouragement through this work.

I am indebted to Professor Yoichi Kawakami for his fruitful suggestions and stimulating comments on this thesis. I would like to thank Associate Professor Yasuhito Gotoh for his helpful advices and valuable discussions. I acknowledge Assistant Professor Yusuke Nishi for meaningful comments and supports in my daily work.

I am grateful to Professor Takashi Hikihara and Associate Professor Nobuo Satoh for their kind introduction to the structural analysis of microelectromechanical systems (MEMS) using finite element method (FEM) and constructive discussion of MEMS vibration. I also received generous support from Mr. Masataka Minami and Mr. Atsushi Yao for maintaining MEMS simulation software.

I would like to express my gratitude to Dr. Hiroshi Yamaguchi and Dr. Hajime Okamoto in NTT Basic Research Laboratories. They generously provided the measurement system of resonance characteristics of MEMS structures. I received generous support for the measurement as well as insightful suggestions.

Mr. Ryohei Kanno, Mr. Kouhei Adachi, and Mr. Kousei Sato gave me meaningful time to discuss wide-bandgap-semiconductor MEMS and kindhearted support for fabricating and characterizing the MEMS devices. I also would like to express my appreciation to Dr. Bernd Zippelius, Dr. Hironori Yoshioka, Dr. Hiroki Miyake, Mr. Yuichiro Nanen, Mr. Naoya Morioka, Mr. Takafumi Okuda, Mr. Hiroki Niwa, and Mr. Naoki Kaji for their fruitful comments and valuable discussions about device fabrication and characterization as well as generous instruction of the experimental procedures.

I would like to thank Dr. Gan Feng, Dr. Hironori Okumura, Mr. Toru Hiyoshi, Mr. Kazuki Yamaji, and Mr. Koutarou Kawahara for their careful instruction of the instru-

ments as well as helpful advices. I also wish to appreciate Dr. Atsushi Koizumi, Dr. Hiromi Kaneko, Dr. Giovanni Alfieri, Dr. Masato Noborio, Dr. Masahiro Horita, Mr. Toshihiko Hayashi, Mr. Tatsuya Iwata, Mr. Shunsaku Ueta, Mr. Yibo Zhang, Mr. Yuichirou Hayashi, Mr. Muneharu Kato, Mr. Ryosuke Kikuchi, Mr. Sho Sasaki, Mr. Hirofumi Yamamoto, Mr. Daisuke Horie, Mr. Seigo Mori, and Mr. Mitsuaki Kaneko for their constructive suggestions and discussions.

I wish to thank Ms. Yoriko Ohnaka and Ms. Mizuki Yamada for kindly supporting my daily work. Special thanks are also due to Mr. Kei Senga, Mr. Ryota Suzuki, Mr. Satoru Nakagawa, Mr. Takeshi Fujimoto, Mr. Xiaowei Song, Mr. Daisuke Harata, Mr. Naoki Okimoto, Mr. Shuhei Ichikawa, Mr. Seiya Nakazawa, Mr. Chihiro Kawahara, Mr. Hajime Tanaka, Mr. Takahiro Higashi, Mr. Zeho Youn, and all of the Semiconductor Science and Engineering Laboratory for their kindness and support.

This work was supported in part by the Japan Society for the Promotion of Science (JSPS) through the Grant-in-Aid for Research Fellow (22·5864). This work was also financially supported by the Ministry of Education, Culture, Sports, Science and Technology, Japan, through the Global Center of Excellence (Global COE) Program (C09) and by the Funding Program for World-Leading Innovative R&D on Science and Technology (FIRST Program).

Finally, I sincerely wish to thank my parents, my brother, and all of my friends for their understanding, support, and heartfelt encouragement.

February, 2013
Naoki WATANABE

Contents

Chapter 1

Introduction

1.1 Background

Over the past several decades, science and technology have been explosively developed. The great success of the semiconductor industry has contributed to this advance. Following the invention of the transistor effect led by Shockley, Bardeen, and Brattain at Bell Labs in 1947 [1, 2], semiconductor devices have been growing in performance and spread on vast amount of fields. Currently, semiconductor devices are used in computers, communications equipment, home electronics, and all electric devices. Semiconductor industry has been a core part in evolution of the society, economics and our daily life.

One of the most important milestones in semiconductor industry is the invention of integrated circuits (IC). Kilby at Texas Instruments demonstrated the first IC on a piece of germanium (Ge) in 1958 [3]. At the same time, Noyce at Fairchild introduced planer technology, wiring individual devices such as transistors, capacitors, and resistors together on silicon (Si) wafer surface [4]. This planer technology on a Si wafer is still employed today. Following these inventions of IC technology, the IC industry has been growing mainly based on "miniaturization" which enables to integrate larger amount of devices on a single chip. Miniaturization of devices can enhance the performance of IC devices, i.e., processing large information, storing large amount of memories, and high-speed communication with smaller space and lower energy consumption.

On the other hand, integrating other functional components should lead to the new aspect of the technology. In recent years, microelectromechanical systems (MEMS) have attracted much attention to realize novel functional small devices. MEMS are integrated of miniaturized mechanical and electrical components. The combination use of these components creates new application of miniaturized devices and gives high functionality to electric devices. The MEMS technology should become a key role of our society.

The MEMS field has emerged on the coattails of the IC industry. MEMS constituted mostly mechanical types of devices with at least one or more of their dimensions in the micrometer range. These microscopic mechanical devices, e.g., beams, cantilevers, gears, and

membranes, have been fabricated by using the materials and processes of microelectronics. Si substrates are selectively etched to leave behind the desired geometry. The term "micromachining" has come into use to name the fabrication processes of miniaturized mechanical structures, which are essentially three-dimensional. Although micromachining is rather different from planer IC microstructuring, the general feature of defining a structure utilizing the photolithographic technology remains. Therefore, MEMS have attracted much attention as integrated components of miniaturized mechanical structures with microelectronics, mainly for sensing and actuating applications. This integration can make the system faster, more reliable, cheaper, and capable of incorporating more complex functions [5]. Nowadays, MEMS have been utilized in a large number of fields such as information and communication technology, automotive and electronics industry, and even medical and biotechnology applications.

1.2 Current Status of MEMS

The first impetus for the use of single-crystalline Si as a micromechanical element in MEMS can be traced to the discovery of its large piezoresistance. Pfann proposed a Si piezoresistive sensors for the measurement of stress, strain, and pressure in 1961 [6]. As early as 1962, Tufte and coworkers made a thin Si piezoresistive diaphragm for pressure sensors using a combination of wet isotropic etching, dry etching, and oxidation [7]. To achieve better sensitivity and stability than possible with piezoresistive pressure sensors, capacitive pressure sensors were first demonstrated by Angell around 1977 [8]. In addition, Si accelerometers were reported in 1979 [9].

Following these passive microsensor devices, innovative micromachined structures began to be explored. Mehregany and colleagues, in 1987, demonstrated miniaturized gears and motors [10], which led to the concept of microscopic actuators on a Si substrate. Subsequently, microactuator devices, e.g., micromotors [11, 12] and comb-drive actuators [13], were demonstrated. Inkjet nozzle arrays were produced by IBM [14–16]. An integrated gas chromatograph system on a Si substrate was demonstrated in 1979 [17]. This application would lead to micro total analytical systems on a chip (μTAS). Optical MEMS (e.g., optical switches [18–20] and scanning micromirrors [21]), rf-MEMS for high-speed wireless communication [22, 23], and power MEMS devices [24] are also very attractive applications of MEMS.

Although the MEMS micromachining technology has emerged from the microstructuring for IC electronics, the micromachining technology came to be different. While IC fabrication processes are essentially planer and the depth of structuring is generally below 1 μm, the structures of microsystems are essentially three-dimensional. In addition, microsystems need a great variety of structures which determine the performance and the functions of microsystems. Therefore, manifold micromachining methods have been devel-

oped. Anisotropic etching, which etches materials with directional preferences, is the most common method for microstructuring [25–27]. As shown in Fig. 1.1, this method can fabricate microstructures which are defined by the slow etching planes. Anisotropic etching for Si MEMS typically performed using potassium hydroxide (KOH) solution. Another micromachining technology, surface micromachining [28–30] uses a sacrificial layer as shown in Fig. 1.2. The structural layer remains and is set free when the sacrificial layer is removed. The sacrificial layer is typically silicon oxide, which can be removed by a hydrogen fluoride (HF) solution. Combining these micromachining technologies and other micromachining methods, e.g., lithographie galvanoformung und abformung (LIGA) process [31], anodic bonding [32], and deep dry etching with high aspect ratio [33], with standard IC microstructuring processes, a great variety of MEMS structures have been realized.

Materials typically used for MEMS devices are shown in Table 1.1. Although various materials such as Si, sapphire, polymers, and ceramics are used for microsystems, the most common material for MEMS technology is Si, which is mostly used in microelectronics industry. Si is cost-effective, easy to fabricate MEMS devices, and also reasonably durable and elastic. The combined use of mechanical structures and electronic devices of Si has been applied toward the development of a vast variety of miniaturized sensor and actuator applications.

A large number of MEMS devices have been utilized in many environments, and a demand for MEMS that can operate in harsh environments characterized as locations of high temperature, high pressure, strong radiation, and corrosive environments has emerged. MEMS devices operating in harsh environments are required in many applications such as automobile, aerospace, nuclear, and chemical industries. However, Si cannot be used as a both structural and electrical material of MEMS devices operating in harsh environments because of its characteristic limitations. Si cannot work as electronic devices over 250°C [34] and it loses yield strength at 500°C [35, 36]. Si is also attacked by corrosive environments. Therefore, an increasing demand for MEMS that can operate at harsh environments stimulated the search for alternatives to Si. The promising candidates of the material for harsh-environment MEMS are wide bandgap semiconductors, e.g., silicon carbide (SiC) and group-Ⅲ nitrides such as gallium nitride (GaN), because of their superior electrical properties, mechanical strength, and chemical inertness in harsh environments [37–39].

1.3 Wide-Bandgap-Semiconductor MEMS and Sensors

1.3.1 Properties of Wide Bandgap Semiconductors

The wide bandgap semiconductors, i.e., SiC and group-Ⅲ nitrides, exhibit excellent mechanical and electrical properties such as high hardness and Young's modulus, low intrin-

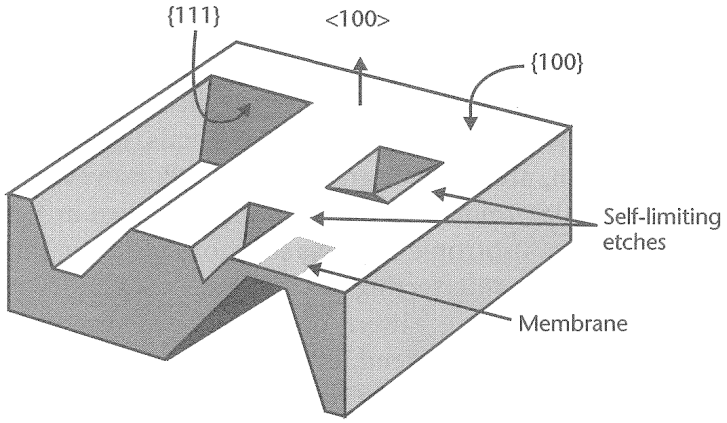

(a) {100}

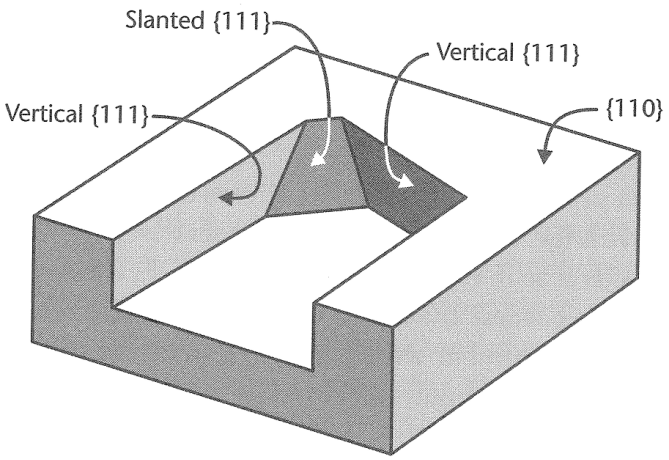

(b) {110}

Figure 1.1: Schematic drawings of the anisotropic etching in (a){100}- and (b){110}-oriented Si [40].

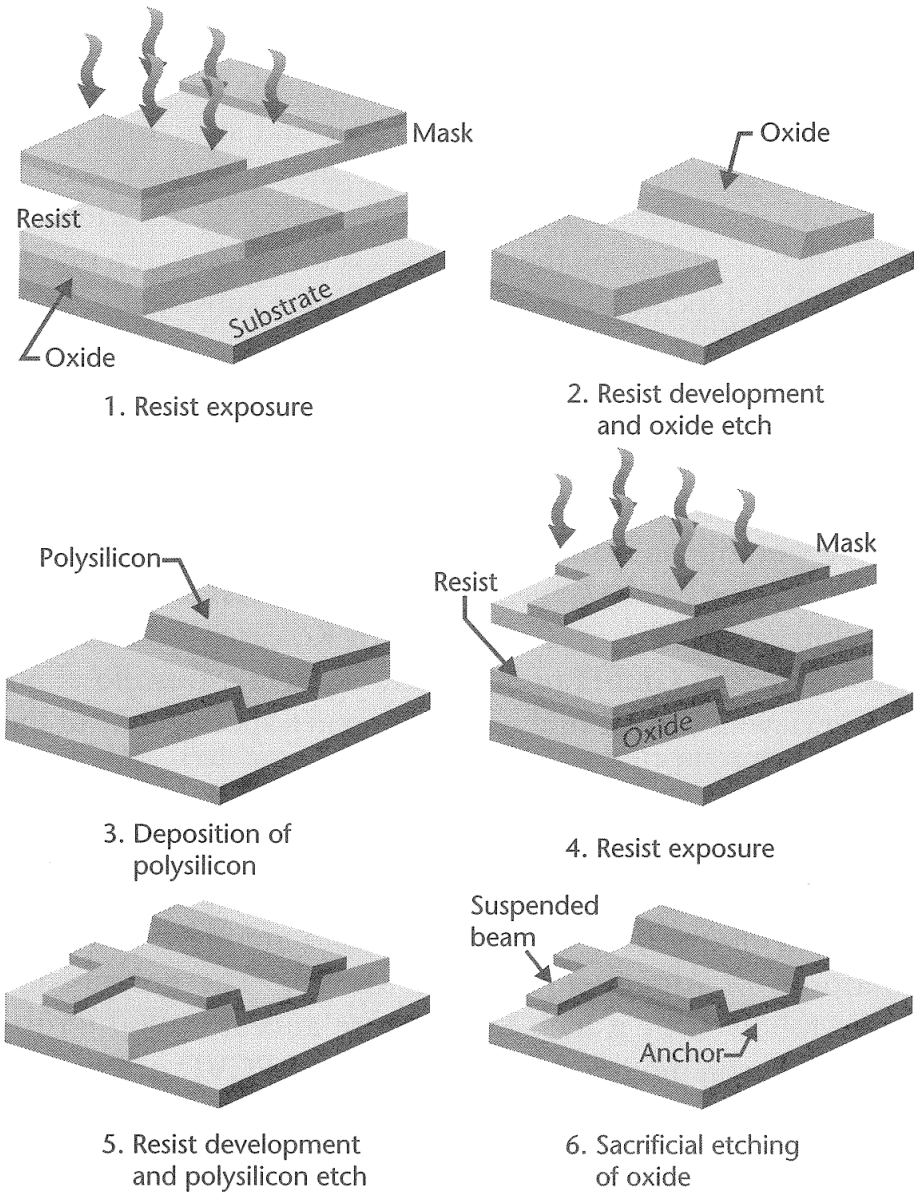

Figure 1.2: Schematic drawings of basic process steps in surface micromachining [40].

Table 1.1: Properties of selected materials typically used for MEMS at 300 K [40].

Properties	Si	SiO_2	Si_3N_4	92% Al_2O_3	GaAs	Polyimide	PMMA
Relative permittivity (ε_r)	11.7	3.9	4-8	9	13.1	–	–
Breakdown field (V/cm $\times$ 10^6)	0.3	5-10	5-10	11.6	0.35	1.5-3	0.17
Electron mobility (cm^2/V·s)	1500	–	–	–	8800	–	–
Hole mobility (cm^2/V·s)	400	–	–	–	400	–	–
Bandgap (eV)	1.12	8-9	–	–	1.42	–	–
Young's modulus (GPa)	160	73	323	275	75	2.5	3
Yield/fracture strength (GPa)	7	8.4	14	15.4	3	0.23	0.06
Poisson's ratio	0.22	0.17	0.25	0.31	0.31	0.34	–
Density (g/cm^3)	2.4	2.2	3.1	3.62	5.3	1.42	1.3
Coefficient of thermal expansion (10^{-6}/K)	2.6	0.55	2.8	6.57	5.9	20	70
Thermal conductivity (W/m·K)	157	1.4	19	36	46	0.12	0.2
Specific heat (J/g·K)	0.7	1.0	0.7	0.8	0.35	1.09	1.5
Melting temperature (°C)	1415	1700	1800	1800	1237	380	90

sic carrier density, and a high breakdown electric field. Brief explanations of the properties of these materials are described in this section. Some basic properties of the materials are listed in Table 1.2.

1.3.1.1 Silicon Carbide

SiC is a group IV–IV compound semiconductor composed of tetrahedrally bonded Si and carbon (C) atoms, which can crystalize in more than 200 different structures with the same stoichiometry, crystal structures of which are called polytypes. The polytypes are commonly identified using the Ramsdell notation [41]. Polytypes can be described as the number of Si–C bilayers in the unit cell and the type of crystal structure, i.e., C for cubic and H for hexagonal. 3C, 4H, and 6H polytypes are most relevant for SiC applications. Schematic structures of 3C-, 4H-, and 6H-SiC are shown in Fig. 1.3. All polytypes of SiC are highly resistant to chemical corrosion.

The elastic constants of 3C-, 4H-, and 6H-SiC can be found in several reports [42–45]. The Young's modulus of SiC ranges between 380 and 700 GPa depending on the polytype and measurement method [39]. These values are shown to be 2-4 times higher than that of Si (190 GPa [46]). For the hardness, Mohs hardness is roughly 9, Knoop hardness was reported to be 2480 kg/mm [46] for 3C-SiC, and microhardness for 6H-SiC is 25 GPa [47]. The temperature dependence of the Young's modulus was determined to be about -0.02 GPa/K for 3C- and hexagonal polycrystalline SiC up to 1000°C [48, 49]. The yield strength is predicted as 0.3 GPa even at 1000°C while the yield strength of Si was reported to be 0.05 GPa at 500°C [50].

In terms of the electrical properties, 4H- and 6H-SiC are commonly used for SiC electronic devices because of the availability of high quality crystals. The bandgaps of 4H- and 6H-SiC are 3.26 and 3.02 eV at room temperature (RT), respectively. Compared with that of Si, the values are 3 times higher so that the low intrinsic carrier density is obtained in SiC. This feature makes it possible to operate SiC electronic devices and sensors at high temperatures above 500°C. The low intrinsic carrier density also gives a far reduced reverse leakage current in SiC pn junction, providing extremely low dark current in SiC photodetectors. The breakdown electric field of 3 MV/cm is 10 times higher than that of Si, allowing the high blocking voltage at a reverse-connected pn junction. This junction can be used to obtain electrical isolation in SiC MEMS devices.

Apart from the use for MEMS and sensor devices, SiC is promising material for power semiconductor devices because of its large breakdown electric field. The breakthrough of "step-controlled epitaxy" has made it possible to grow a high-quality epitaxial layer without any inclusions on a SiC substrate [51, 52]. Both n-type and p-type doping can be controlled in a wide range from 10^{14} to 10^{19} cm^{-3}, and selective conductivity control can be also available by employing ion implantation technique. Thus there have been many reports on SiC power devices such as Schottky barrier diodes [53–55]. Switching devices such as metal-oxide-semiconductor field-effect transistors [56–59] and bipolar junction transistors [60–62]

Table 1.2: Properties of SiC, GaN, and AlN at 300 K [39, 40, 63–69]. Note that GaN and AlN listed in this table are wurtzite (2H).

Properties	Si	3C-SiC	4H-SiC	6H-SiC	GaN	AlN
Relative permittivity (ε_r)	11.7	9.72	9.66 ($\perp c$ axis)		8.9	8.5
Breakdown field (V/cm $\times$ 10^6)	0.3	$\sim$1	3-5	3-5	$\sim$3.3	5
Electron mobility (cm^2/V·s)	1500	1000	1000	450	1500	300
Hole mobility (cm^2/V·s)	400	100	120	90	200	14
Bandgap (eV)	1.12	2.36	3.26	3.02	3.39	6.2
Young's modulus (GPa)	160		380-700		250-330	308-339
Yield/fracture strength (GPa)	7	–	–	21	–	16
Poisson's ratio	0.22	–	0.21	–	0.23	0.287
Density (g/cm^3)	2.4		3.21		6.15	3.23
Coefficient of thermal expansion (10^{-6}/K)	2.6	3.8	–	4.3 ($\perp c$ axis)	3.17 ($\perp c$ axis)	5.3 ($\perp c$ axis)
Thermal conductivity (W/m·K)	157		490		130	285
Specific heat (J/g·K)	0.7		0.69		0.49	0.6
Melting temperature (°C)	1415		$\sim$2800 (at 35 atm)		2500	2750 (at 100 atm)

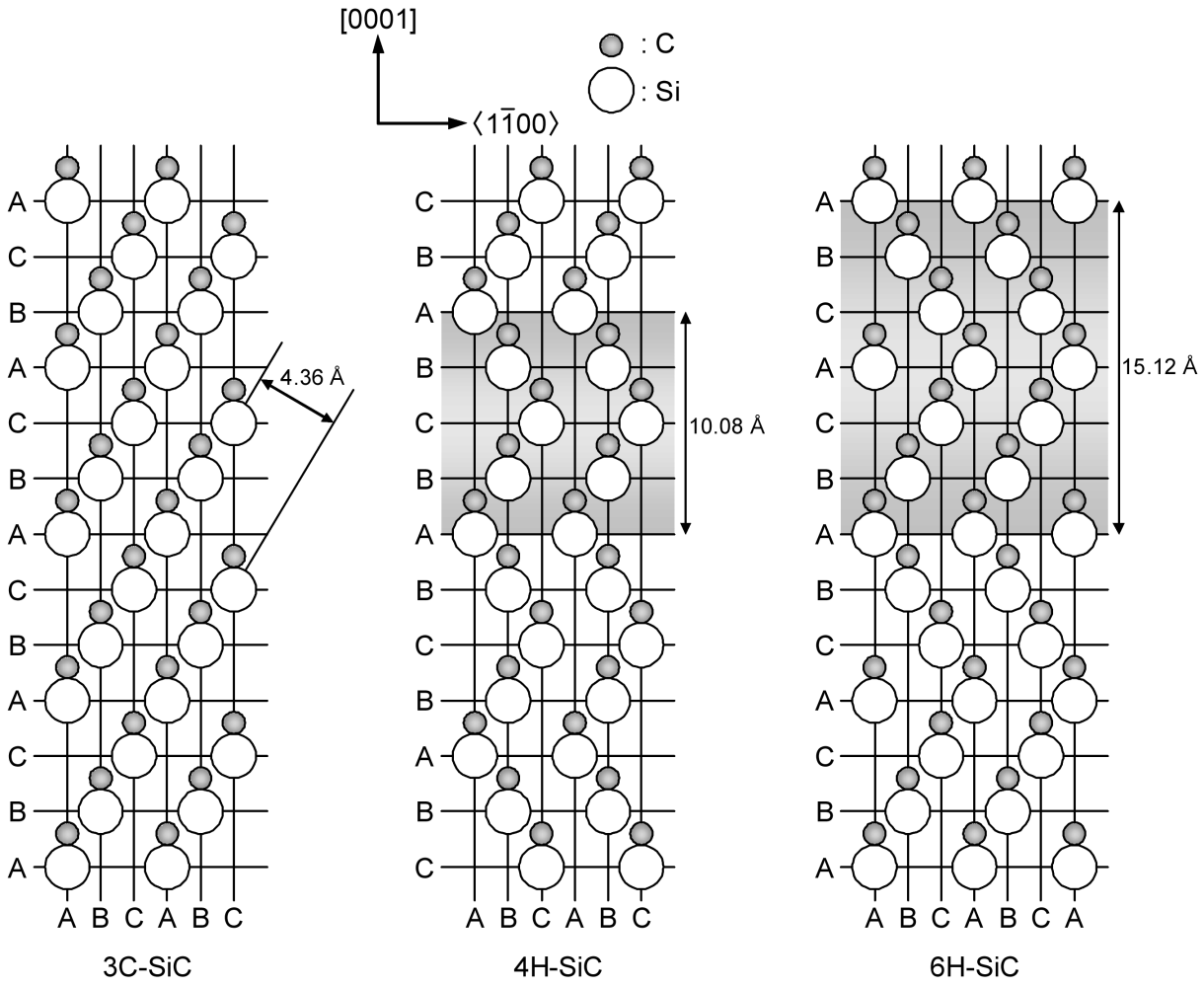

Figure 1.3: Stacking orders along [0001] (c-axis) for 3C-, 4H-, and 6H-SiC. Open and filled circles represent Si and C atoms, respectively.

have been also extensively investigated with SiC.

1.3.1.2 Group-Ⅲ Nitrides

Group-Ⅲ nitrides, i.e., GaN, aluminum nitride (AlN), and indium nitride (InN), are Ⅲ–V compound semiconductors composed of tetrahedrally bonded cation and anion atoms. All three binaries and their alloys crystallize in both hexagonal (2H, or wurtzite) and cubic (3C, or zincblende) structures. Schematic structure of a wurtzite crystal is shown in Fig. 1.4.

Mechanical properties of group-Ⅲ nitrides, especially GaN and AlN, are excellent as well as these of SiC. The elastic constants of GaN [70–72] and AlN [72, 73] have been reported. The microhardness was reported to be 10.2-12 and 14 GPa for GaN and AlN, respectively [64, 74]. Although these values are about 2 times lower than those of SiC, these are comparable to that of Si (9 GPa [64]), and the microhardness of GaN at 1000°C has been reported to be around 3 GPa, which is much larger than that of Si (0.5 GPa) [74]. The Young's modulus of GaN was reported to be 250-330 GPa [64–66], and that of AlN was 308-339 GPa [68, 69]. Moreover, group-Ⅲ nitrides, in particular AlN, exhibit excellent piezoelectric properties [75].

Group-Ⅲ nitrides are also strongly investigated as a material of optoelectronic and power switching devices. High-quality GaN epitaxial growth with low-temperature AlN buffer layers was invented in 1986 [76], and p-type doping for GaN was realized by the invention of low-energy electron beam irradiation in 1989 [77]. Following these inventions, group-Ⅲ-nitride-based optoelectronic devices such as light emitting diodes [78–81] and laser diodes [82, 83], devices which can be operated at the spectral range from the green to the ultra-violet region, have been reported. Power switching devices such as high-electron-mobility transistors made of group-Ⅲ nitrides have been investigated as well [84–86].

1.3.2 Advantages of Wide Bandgap Semiconductors for MEMS and Sensor Applications

The main advantages of the wide bandgap semiconductors include the extremely high mechanical, thermal, and chemical stability, advantages of which enable MEMS devices to work in harsh environments. In addition, higher Young's modulus of the wide bandgap semiconductor should achieve higher frequencies and higher quality factors in resonant MEMS devices at the same geometrical dimensions in comparison with Si. The high Young's modulus can also realize MEMS devices which can better maintain a linear relationship between applied load and induced deformation.

Electrical properties of the wide bandgap semiconductors are excellent as well. SiC and group-Ⅲ nitrides have also attracted much attention as a material for electronic devices and have been intensively investigated [87–90]. The large bandgap of these materials should lead to high-temperature operation of semiconductor devices, including sensors such as gas and photo detectors. The combination of excellent electrical and mechanical properties

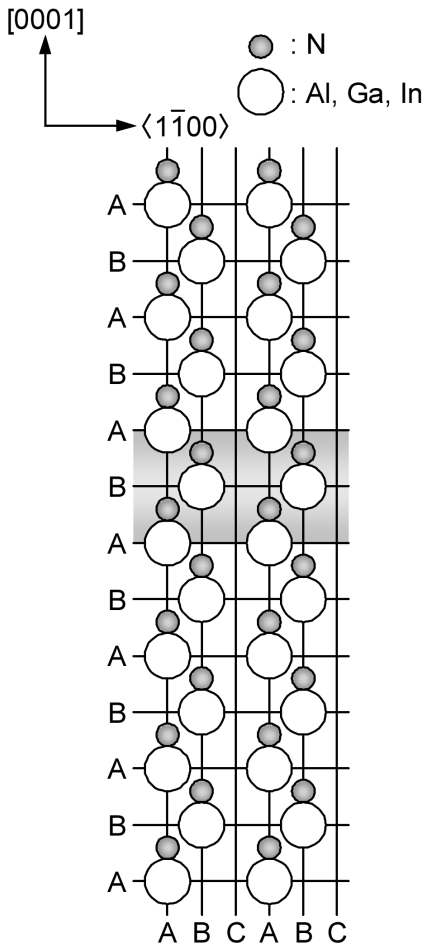

Figure 1.4: Stacking orders along [0001] (c-axis) for 2H-Ⅲ-N (Ⅲ: Al, Ga, In). Open and filled circles represent Ⅲ and N atoms, respectively.

offers many opportunities for using the wide bandgap semiconductors as a material for integrated sensor systems of MEMS and semiconductor devices in applications featuring harsh environments.

On the other hand, the utilization of wide bandgap semiconductors can introduce new functions for microsystems. The wide bandgap semiconductors have excellent functionalities, such as piezoresistivity which particularly favors group-Ⅲ nitrides, as well as superior material properties. Despite some of these functions can be realized with functional ceramics such as lead zirconate titanate (PZT) for piezoelectric applications, the high structural quality and the dimensional control up to the monolayer level for group-Ⅲ nitrides favor their application. Visible-range transparency, which is one of the unique characteristics of the wide bandgap semiconductors, enables to realize novel optical MEMS devices when they are used as dielectric materials for optical lenses, filters, and photonic crystals. For example, the transparent wavelength of an optical band-pass filter with a monolithically-integrated microheater can be controlled by varying the refractive index through the thermo-optic effect, i.e., the temperature dependence of the refractive index. When such tunable filters are fabricated using wide bandgap semiconductors, the operating wavelength regions can be expanded from infrared to the visible and ultraviolet regions because of their large bandgap.

Moreover, by combining such novel optical MEMS with wide-bandgap-semiconductor MEMS and sensor devices, high functional and high performance smart devices can be realized. For example, I propose the combination of a tunable optical filter and a wide-bandgap-semiconductor-based photodiode. The combination can realize a very small spectrometer. A schematic drawing of the micro spectrometer is shown in Fig. 1.5 utilizing SiC as a material for the photodiode and GaN for the tunable filter. A wide range of operating temperatures of wide-bandgap-semiconductor-based photodiodes allows a wide-temperature-range modulation resulting in a wide range of tunable wavelengths.

1.3.3 Key Issues in Wide-Bandgap-Semiconductor MEMS and Sensors

As described in the previous sections, the wide bandgap semiconductors have superior characteristics compared with Si so that harsh-environment MEMS can be realized using these materials, in particular SiC. In 1992, Tong and coworkers reported suspended 3C-SiC diaphragms fabricated with Si micromachining techniques [91]. MEMS devices such as resonators [92], comb drives [93] and micromotors [94] made with 3C- or polycrystalline SiC thin films on a Si substrate were demonstrated. These SiC films possess many advantages compared with Si. However, single-crystalline SiC free of structural defects, i.e., homoepitaxially-grown 4H- and 6H-SiC, is expected to lead to far superior device performance. MEMS devices with high-quality single-crystalline SiC is expected to extend the range of applicability to harsh-environment MEMS. Furthermore, the other constituent components of SiC film MEMS devices, e.g., substrates and spacer layers, are commonly

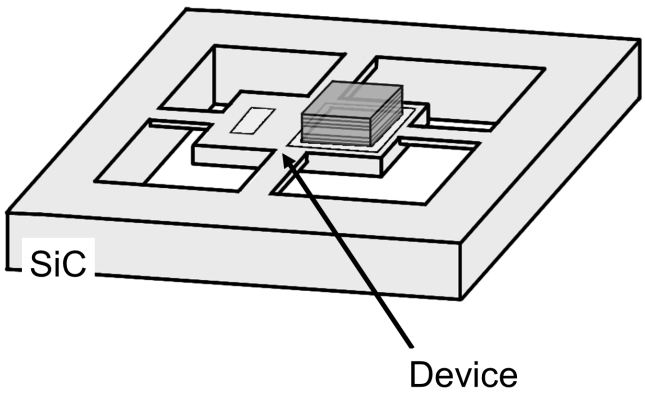

(a) Bird's-eye view

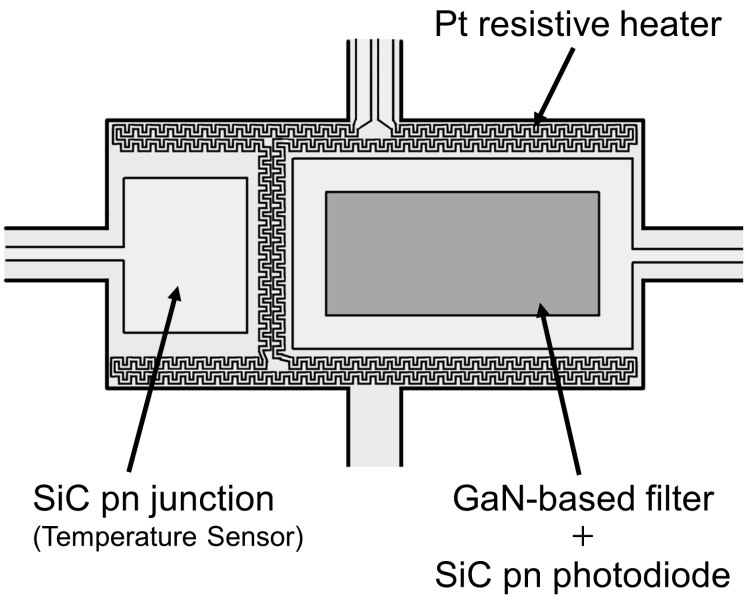

(b) Top view of device part

Figure 1.5: Schematic drawing of a proposed very small spectrometer which is the combination of a tunable optical filter and a wide-bandgap-semiconductor-based photodiode. GaN is used for a material of the tunable filter and SiC is used for the photodiode in this drawing. SiC pn junction is also utilized to meaqsure the device temperature. In addition, a platinum (Pt) resistive heater is formed to elevate the device temperature for the modulation of the transparent wavelength.

fabricated with conventional structural materials such as Si and silicon oxides. Even if SiC films can resist harsh environmental conditions, the actual range of operating conditions is restricted by the limitations of the conventional materials. Therefore, MEMS devices which consist of entirely single-crystalline SiC should be investigated. However, it is difficult to fabricate devices composed entirely of SiC due to its chemical inertness and mechanical hardness. One of microfabrication processes, dry reactive ion etching (RIE) of SiC has been investigated, and some MEMS devices such as piezoresistive accelerometers were demonstrated [95]. RIE process, however, does not have selectivity which is necessary for the fabrication of complex structures. SiC micromachining processes should be investigated to realize all-single-crystalline SiC MEMS devices.

As for wide-bandgap-semiconductor sensors, gas sensors [96] and ultraviolet photodetectors [97–100] fabricated with SiC were reported. Focusing on photodetectors, several groups have extensively investigated with various wide bandgap semiconductors as described in a review [101]. In the case of 6H-SiC, Edmond and coworkers reported high quantum efficiency of pn photodiodes up to 350°C [99, 100]. However, there have been no detailed studies on the temperature dependence of the photoresponse of SiC pn photodiodes. Small temperature dependence of the photoresponse should be required in order to operate the devices in a wide range of temperatures, at which only wide-bandgap-semiconductor-based devices can work. Furthermore, there has been few detail studies about high temperature operation of SiC electronic devices up to extremely high temperature. For example, to operate SiC pn junction devices properly at high temperature, it is necessary to understand the electrical characteristics of SiC pn junction at high temperature. It should be noted that knowledge of the high-temperature electronics of SiC pn junction is also important for all-single-crystalline SiC MEMS devices which employ SiC pn junctions as electrical isolation layers.

In addition, to utilize wide bandgap semiconductors for microsystems with high functionality and high performance, the material properties of the wide bandgap semiconductors should be revealed. However, the knowledge available at the present time is not enough. For example, as proposed in the previous section, wide bandgap semiconductors can be used for tunable optical filters utilizing the thermo-optic effect. Although the refractive indices and their temperature dependence of SiC, GaN, and AlN are essential, investigations of the thermo-optic effect of these materials are very limited. In photodetectors made of SiC, the temperature dependence of the absorption coefficient of the constituent material is crucial to design the devices operating up to high temperature while there are few reports about that of SiC.

To realize high functional and high performance smart devices made of wide bandgap semiconductors, these issues must be solved.

1.4 Outline of This Thesis

In this thesis, 1) determination of the optical properties of SiC, GaN, and AlN from RT to very high temperature, 2) investigation of SiC micromachining process and fabrication of all-single-crystalline SiC MEMS devices, and 3) investigation of high-temperature operation of SiC pn photodiodes, are performed toward the realization of integrated smart sensors made of wide bandgap semiconductors.

In Chapters 2 and 3, temperature dependence of the optical properties of SiC, GaN, and AlN up to high temperature is described. In Chapter 2, The thermo-optic coefficients, i.e., the temperature dependence of the refractive indices, of SiC, GaN, and AlN are determined up to 500°C toward realizing wide-bandgap-semiconductor-based tunable optical filters. Optical simulation of a GaN-based tunable band-pass filter at RT and 500°C are also carried out by using the refractive indices and the thermo-optic coefficients of GaN and AlN obtained in this study. In Chapter 3, determination of temperature dependence of the absorption coefficient of SiC for device design of SiC photodetectors at high temperature is presented.

In Chapter 4, fabrication process of SiC MEMS devices and demonstration of all-single-crystalline SiC MEMS devices are presented. I describe the device design of SiC MEMS and fabrication processes including RIE process for device patterning and photoelectrochemical and electrochemical etching processes for doping-type selective etching which can realizes the sacrificial-layer process. Suspended SiC bridge structures using photoelectrochemical etching are fabricated and electrostatic actuation of the device is demonstrated. In addition, SiC cantilever structures are fabricated with electrochemical etching and resonance characteristics of fabricated devices are investigated.

In Chapter 5, investigations for high-temperature operation of SiC pn photodiodes are presented. This chapter includes two parts: 1) detailed study of the temperature dependence of the photoresponse and 2) investigation of the electrical characteristics of fabricated pn photodiodes up to 600°C to operate the devices properly at such high temperature. In the first part, I demonstrate that the device showed small temperature dependence at certain wavelength illumination, and I propose that the targeted wavelength can be adjusted on the same device by controlling the reverse-bias voltage. In the second part, the origin of the reverse leakage current of fabricated devices and reduction of the leakage current inventing the surface passivation process are presented. I evaluate the photoresponse of the fabricated device for various wavelengths up to 500°C.

In Chapter 6, conclusions of this study and suggestions for future work are presented.

References

[1] J. Bardeen and W. H. Brattain, Phys. Rev. Lett. **74**, 230 (1948).

[2] J. Bardeen and W. H. Brattain, US Patent 2524035 (1950).

[3] J. S. Kilby, US Patent 3138743 (1959).

[4] R. N. Noyce, US Patent 2981877 (1959).

[5] V. K. Varadan, Proc. SPIE **5062**, 20 (2003).

[6] W. G. Pfann, Solid State Electron. **3**, 261 (1961).

[7] O. N. Tafte, P. W. Chapman, and D. Long, J. Appl. Phys. **33**, 3322 (1962).

[8] J. B. Angell, S. C. Terry, and P. W. Barth, Sci. Am. **248**, 44 (1983).

[9] L. M. Roylance and J. B. Angell, IEEE Trans. Electron Devices **26**, 1911 (1979).

[10] M. Mehregany, K. J. Gabriel, and W. S. N. Trimmer, Sens. Actuators **12**, 341 (1987).

[11] L. -S. Fan, Y. -C. Tai, and R. S. Muller, Sens. Actuators **20**, 41 (1989).

[12] Y. C. Tai and R. S. Muller, Sens. Actuators **20**, 49 (1989).

[13] W. C. Tang, T. C. H. Nguyen, and R. T. Howe, Sens. Actuators **20**, 25 (1989).

[14] E. Bassous, H. H. Taub, and L. Kuhn, Appl. Phys. Lett. **31**, 135 (1977).

[15] L. Kuhn, E. Bassous, and R. Lane, IEEE Trans. Electron Devices **25**, 1257 (1978).

[16] K. Petersen, Proc. IEEE **70**, 135 (1977).

[17] S. C. Terry, J. H. Jerman, and J. B. Angell, IEEE Trans. Electron Devices **26**, 1880 (1979).

[18] L. Y. Lin, E. L. Goldstein, and R. W. Tkach, IEEE J. Sel. Top. Quant. Electron. **5**, 4 (1999).

[19] C. Marker and N. F. de Rooij, J. Lightwave Tech. **15**, 587 (2003).

[20] P. Helin, T. Bourouina, L. Houlet, G. Reyne, and H. Fujita, IEEE J. Sel. Top. Quant. Electron. **8**, 58 (2002).

[21] P. F. van Kessel, L. J. Hornbeck, R. Meier, and M. R. Douglass, Proc. IEEE **86**, 1687 (1998).

[22] C. T. -C. Nguyen, L. P. B. Katehi, and G. M. Rebeiz, Proc. IEEE **86**, 1756 (1998).

[23] W. M. van Spengen, R. Puers, R. Mertens, and I. De Wolf, J. Micromech. Microeng. **14**, 514 (2004).

[24] A. H. Epstein and S. D. Senturia, Science **276**, 1211 (1997).

[25] E. Bassous, IEEE Trans. Electron Devices **25**, 1178 (1978).

[26] H. Seidel, L. Csepregi, A. Heuberger, and H. Baumgärtel, J. Electrochem. Soc. **137**, 3612 (1990).

[27] F. Rudolf and J. Bergqvist, Microelectron. Eng. **15**, 399 (1991).

[28] R. T Howe, J. Vac. Sci. Technol. **B6**, 1809 (1988).

[29] H. Guckel, J. J. Sniegowski, T. R. Christenson, S. Mohney, and T. F. Kelly, Sens. Actuators **20**, 117 (1989).

[30] L. -S. Fan, Y. -C. Tai, and R. S. Muller, IEEE Trans. Electron Devices **35**, 724 (1988).

[31] E. W. Becker, W. Ehrfeld, P. Hagmann, A. Maner, and D. Münchmeyer, Microelectron. Eng. **4**, 35 (1986).

[32] G. Wallis and D. I. Pomerantz, J. Appl. Phys. **40**, 3946 (1969).

[33] F. Läermer and A Schilp, German Patent DE 4241045 (1994).

[34] R. Hull, *Properties of Crystalline Silicon*, (Institution of Engineering and Technology, Hertfordshire, 1999).

[35] M. Omri, C. Tête, J. -P. Michel, and A. George, Philos. Mag. A **55**, 601 (1987).

[36] J. Castaing, P. Veyssière, L. P. Kubin, and J. Rabier, Philos. Mag. A **44**, 1407 (1981).

[37] V. Cimalla, J. Pezoldt, and O. Ambacher, J. Phys. D: Appl. Phys. **40**, 6386 (2007).

[38] M. Mehregany, C. A. Zorman, S. Roy, A. J. Fleischman, C. H. Wu, and N. Rajan, Int. Mater. Rev. **45**, 85 (2000).

[39] C. A. Zorman and R. J. Parro, Phys. Stat. Sol. B **245**, 1404 (2008).

[40] N. Maluf and K. Williams, *An Introduction to Microelectromechanical Systems Engineering, 2nd Edition*, (Artech House Publishers, Boston, 2004).

[41] L. S. Ramsdell, Amer. Min. **32**, 64 (1947).

[42] K. Karch, P. Pavone, W. Windl, O. Schütt, and D. Strauch, Phys. Rev. B **50**, 17054 (1994).

[43] A. P. Mirogorodsky, M. B. Smirnov, E. Abdelmounim, T. Merle, and P. E. Quintard, Phys. Rev. B **52**, 3993 (1995).

[44] K. Kamitani, M. Grimsditch, J. C. Nipko, C. -K. Loong, M. Okada, and I. Kimura, J. Appl. Phys. **82**, 3152 (1997).

[45] W. R. L. Lambrecht, B. Segall, M. Methfessel, and M. van Schilfgaarde, Phys. Rev. B **44**, 3685 (1991).

[46] K. E. Petersen, Proc. IEEE **70**, 420 (1982).

[47] A. Kakanakova-Georgieva, E. P. Trifonova, R. Yakimova, M. F. McMillan, and E. Janzén, Cryst. Res. Technol. **34**, 943 (1999).

[48] Z. Li and R. C. Bradt, J. Mater. Sci. **22**, 2557 (1987).

[49] Z. Li and R. C. Bradt, Int. J. High Technol. Ceram. **4**, 1 (1988).

[50] T. Suzuki, I. Yonenaga, and H. O. K. Kirchner, Phys. Rev. Lett. **75**, 3470 (1995).

[51] T. Kimoto, A. Itoh, and H. Matsunami, Phys. Stat. Sol. B **202**, 247 (1997).

[52] H. Matsunami and T. Kimoto, Mater. Sci. Eng. R **20**, 125 (1997).

[53] T. Kimoto, T. Urushidani, S. Kobayashi, and H. Matsunami, IEEE Electron Device Lett. **14**, 548 (1993).

[54] A. Itoh, T. Kimoto, and H. Matsunami, IEEE Electron Device Lett. **16**, 280 (1995).

[55] K. J. Schoen, J. M. Woodall, J. A. Cooper, *Jr.*, and M. R. Melloch, IEEE Trans. Electron Devices **45**, 1595 (1998).

[56] J. W. Palmour, J. A. Edmond, H. S. Kong, and C. H. Carter, *Jr.*, Inst. Phys. Conf. **137**, 499 (1994).

[57] H. Yano, F. Katafuchi, T. Kimoto, and H. Matsunami, IEEE Trans. Electron Devices **46**, 504 (1999).

[58] H. Yano, T. Hirao, T. Kimoto, and H. Matsunami, Appl. Phys. Lett. **78**, 374 (2001).

[59] M. Noborio, J. Suda, S. Beljakowa, M. Krieger, and T. Kimoto, Phys. Stat. Sol. A **206**, 2374 (2009).

[60] S. -H. Ryu, A. K. Agarwal, R. Singh, and J. W. Palmour, IEEE Electron Device Lett. **22**, 124 (2001).

[61] H. -S. Lee, M. Domeij, C. -M. Zetterling, M. Östling, F. Allerstam, and E. Ö. Sveinbjörnsson, IEEE Electron Device Lett. **28**, 1007 (2007).

[62] H. Miyake, T. Kimoto, and J. Suda, IEEE Electron Device Lett. **32**, 285 (2011).

[63] M. E. Levinshtein, S. L. Rumyantsev, and M. S. Shur (*eds.*), *Properties of Advanced Semiconductor Materials: GaN, AlN, InN, BN, SiC, SiGe*, (John Wiley & Sons, Toronto, 2001).

[64] M. D. Drory, J. W. Ager, T. Suski, I. Grzegory, and S. Porowski, Appl. Phys. Lett. **69**, 4044 (1996).

[65] Z. Yang, R. N. Wang, S. Jia, D. Wang, B. S. Zhang, K. M. Lau, and K. J. Chen, Appl. Phys. Lett. **88**, 041913 (2006).

[66] T. Zimmermann, M. Neuburger, P. Benkart, F. J. Hernández-Guillén, C. Pietzka, M. Kunze, I. Daumiller, A. Dadgar, A. Krost, and E. Kohn, IEEE Electron Device Lett. **27**, 309 (2006).

[67] C. Kisielowski, J. Krüger, S. Ruvimov, T. Suski, J. W. Ager, Ⅲ, E. Jones, Z. Liliental-Weber, M. Rubin, and E. R. Weber, Phys. Rev. B **54**, 17745 (1996).

[68] D. Gerlich, S. L. Dole, and G. A. Slack, J. Phys. Chem. Solids **47**, 437 (1986).

[69] C. Deger, E. Born, H. Angerer, O. Ambacher, M. Stutzmann, J. Hornsteiner, E. Riha, and G. Fischerauer, Appl. Phys. Lett. **72**, 2400 (1998).

[70] V. A. Savastenko and A. U. Sheleg, Phys. Stat. Sol. A **48**, K135 (1978).

[71] A. Polian, M. Grimsditch, and I. Grzegory, J. Appl. Phys. **79**, 3343 (1996).

[72] A. F. Wright, J. Appl. Phys. **82**, 2833 (1997).

[73] L. E. McNeil, M. Grimsditch, and R. H. French, J. Am. Ceram. Soc. **76**, 1132 (1993).

[74] I. Yonenaga, T. Hoshi, and A. Usui, Jpn. J. Appl. Phys. **39**, L200 (2000).

[75] A. D. Bykhovski, B. L. Gelmont, and M. S. Shur, J. Appl. Phys. **81**, 6332 (1996).

[76] H. Amano, N. Sawaki, I. Akasaki, and Y. Toyoda, Appl. Phys. Lett. **48**, 353 (1986).

[77] H. Amano, M. Kito, K. Hiramatu, and I. Akasaki, Jpn. J. Appl. Phys. **28**, L2112 (1989).

[78] S. Nakamura, T. Mukai, and M. Senoh, Jpn. J. Appl. Phys. **30**, L1998 (1991).

[79] S. Nakamura, M. Senoh, N. Iwasa, and S. Nagahama, Jpn. J. Appl. Phys. **34**, L797 (1995).

[80] Y. Taniyasu, M. Kasu, and T. Makimoto, Nature **441**, 325 (2006).

[81] H. Hirayama, T. Yatabe, N. Noguchi, T. Ohashi, and N. Kamata, Appl. Phys. Lett. **91**, 071901 (2007).

[82] S. Nakamura, M. Senoh, S. Nagahama, N. Iwase, T. Yamada, T. Matsushita, H. Kiyoku, and Y. Sugimoto, Jpn. J. Appl. Phys. **35**, L74 (1996).

[83] S. Sota, H. Sakai, T. Tanaka, M. Koike, and H. Amano, Electron. Lett. **32**, 1105 (1996).

[84] M. Asif Khan, A. Bhattarai, J. N. Kuznia, and D. T. Olson, Appl. Phys. Lett. **63**, 1214 (1993).

[85] S. T. Sheppard, K. Doverspike, W. L. Pribble, S. T. Allen, J. W. Palmour, L. T. Kehias, and T. J. Jenkins, IEEE Electron Device Lett. **20**, 161 (1999).

[86] Y. -F. Wu, A. Saxler, M. Moore, R. P. Smith, S. Sheppard, P. M. Chavarkar, T. Wisleder, U. K. Mishra, and P. Parikh, IEEE Electron Device Lett. **25**, 117 (2004).

[87] H. Morkoç, S. Strite, G. B. Gao, M. E. Lin, B. Sverdlov, and M. Burns, J. Appl. Phys. **76**, 1363 (1994).

[88] M. Ruff, H. Mitlehner, and R. Helbig, IEEE Trans. Electron Devices **41**, 1040 (1994).

[89] C. E. Weitzel, J. W. Palmour, C. H. Carter, *Jr.*, K. Moore, K. J. Nordquist, S. Allen, C. Thero, and M. Bhatnagar, IEEE Trans. Electron Devices **43**, 1732 (1996).

[90] S. N. Mohammad, A. A. Salvador, and H. Morkoç, Proc. IEEE **83**, 1306 (1995).

[91] L. Tong, M. Mehregany, and L. G. Matus, Appl. Phys. Lett. **60**, 2992 (1992).

[92] L. Jiang, R. Cheung, M. Hassan, A. J. Harris, J. S. Burdess, C. A. Zorman, and M. Mehregany, J. Vac. Sci. Technol. B **21**, 2998 (2003).

[93] A. J. Fleischman, X. Wei, C. A. Zorman, and M. Mehregany, Mater. Sci. Forum **264-268**, 885 (1998).

[94] A. A. Yasseen, C. H. Wu, C. A. Zorman, and M. Mehregany, IEEE Electron Device Lett. **21**, 164 (2000).

[95] A. R. Atwell, R. S. Okojie, K. T. Kornegay, S. L. Roberson, and A. Beliveau, Sens. Actuators A **104**, 11 (2003).

[96] A. L. Spetz, A. Baranzahi, P. Tobias, and I. Lundström, Phys. Stat. Sol. A **162**, 493 (1997).

[97] R. B. Campbell and H. C. Chang, Solid State Electron. **10**, 949 (1967).

[98] P. Glasow, G. Ziegler, W. Suttrop, G. Pensl, and R. Helbig, Proc. SPIE **868**, 40 (1987).

[99] D. M. Brown, E. T. Downey, M. Ghezzo, J. W. Kretchmer, R. J. Saia, Y. S. Liu, J. A. Edmond, G. Gati, J. M. Pimbley, and W. E. Schneider, IEEE Trans. Electron Devices **40**, 325 (1993).

[100] J. Edmond, H. Kong, A. Suvorov, D. Waltz, and C. Carter, *Jr.*, Phys. Stat. Sol. A **162**, 481 (1997).

[101] E. Monroy, F. Omnès, and F. Calle, Semicond. Sci. Technol. **18**, R33 (2003).

Chapter 2

Determination of Thermo-Optic Coefficients of SiC, GaN, and AlN for Tunable Filter Application

2.1 Introduction

For the proper design of optoelectronic devices, knowledge of the refractive index of constituent materials is required. The refractive index of any material depends on temperature. This effect, known as the thermo-optic effect, should be considered for devices operating in a wide temperature range. For example, since the junction temperature of a laser diode (LD) is well above room temperature (RT) under operating conditions [1], failure to consider the thermo-optic effect results in a suboptimal LD waveguide design.

Wide bandgap semiconductors, silicon carbide (SiC), gallium nitride (GaN), and aluminum nitride (AlN), have attracted much attention as materials for optoelectronic devices, such as light emitters and photodetectors, in a spectral range from the visible to the ultraviolet (UV) region [2–7]. To design wide-bandgap-semiconductor-based optoelectronic devices properly, the temperature dependences of the refractive indices of these materials should be revealed. Wide bandgap semiconductors also have superior thermal stability and are capable of operation at very high temperature. For example, the operation of SiC UV photodiodes up to 350°C has been demonstrated [6], and it was reported that GaN-based photodiodes are capable of operation at temperatures much higher than 400°C [7], owing to their large bandgap. Therefore, investigation of the refractive indices of SiC, GaN, and AlN and their temperature dependence is necessary to design such high-temperature devices.

On the other hand, the thermo-optic effect can be used to actively modulate device characteristics by changing temperature. For example, the transparent wavelength of an optical band-pass filter with a monolithically-integrated microheater can be controlled by varying the refractive index through the thermo-optic effect. Such devices as tunable filters for the infrared (IR) region have been fabricated using silicon [8], and when tunable filters are

fabricated using SiC, GaN, or AlN, the operating wavelength region can be expanded from the IR to the visible and UV regions because of their large bandgap. By combining such an optical filter with a wide-bandgap-semiconductor-based photodiode, a very small spectrometer can be realized. A wide range of operating temperature of the photodiodes allows a wide-temperature-range modulation resulting in a wide range of tunable wavelengths.

Although the refractive indices and their temperature dependence of SiC, GaN, and AlN are essential, investigations of the thermo-optic effect of these materials are very limited. Della Corte and coworkers reported the thermo-optic coefficient given by $\partial n/\partial T$, where n is the refractive index and T is the temperature, of 6H-SiC at a wavelength of 1.5 μm [9]. And Riza and colleagues reported the thermo-optic coefficient of 6H-SiC at a wavelength of 1.55 μm [10]. Although these works are very useful for applications of optical telecommunication, the wavelength range should be extended to the visible and UV regions for the applications which are mentioned above. For group-Ⅲ nitride, Tisch and coworkers measured the refractive indices of GaN and aluminum gallium nitride ($Al_xGa_{1-x}N$) by spectroscopic ellipsometry (SE) from RT to 300°C [11]. Although the data of the refractive index up to 300°C are adequate for LD design, the data set should be extended to higher temperatures. In addition, the optical anisotropy of GaN and AlN inherent in their crystal structure (wurtzite) should be considered. Tisch and coworkers did not consider the anisotropy in their work.

In this chapter, I have determined the thermo-optic coefficients of 4H-SiC, GaN, and AlN by optical interference measurements employing a vertical-incidence configuration to evaluate the ordinary refractive index (light propagation along the c-axis). The temperature range of the measurements is from RT to about 500°C. The wavelength range is from the IR region (1700 nm) to near the band edge of each material. Recently, wide bandgap semiconductors have been regarded as dielectrics for the IR region, because two-photon absorption is suppressed owing to its large bandgap. The importance of this phenomenon is pronounced in the case of photonic crystals [12]. Thus it is also important to know the thermo-optic coefficients in the IR region as well as the visible and UV regions.

2.2 Theoretical Model

The dispersion of the refractive index in a semiconductor at the transparent region can be described by the interaction between external photons and electrons inside a semiconductor. One of the simplest models of the refractive index dispersion is the single oscillator model proposed by Wemple and DiDomenico [13]. This model considers an effective oscillator at certain energy, in other words, the energy dispersion of extinction coefficient $k(E)$ of the material is assumed to be a delta function at energy E_p:

$$k(E) = \frac{\pi E_\mathrm{d}}{2\delta(E - E_\mathrm{p})} \tag{2.1}$$

where E_{d} is the strength of an effective oscillator at energy E_{p}. Introducing this equation into the Kramers-Kronig relations, we obtain the energy dispersion of the refractive index $n(E)$:

$$n(E)^2 - 1 = \frac{E_{\mathrm{p}} E_{\mathrm{d}}}{E_{\mathrm{p}}^2 - E^2}. \tag{2.2}$$

From the single oscillator model shown in Eq. (2.2), the temperature dependence of the refractive index near the band-edge region can be deduced. The following equation can be given by changing Eq. (2.2):

$$n(E)^2 = 1 + \frac{E_{\mathrm{d}}}{E_{\mathrm{p}} - E^2/E_{\mathrm{p}}}. \tag{2.3}$$

Assuming the near-band-edge region, i.e., $E \sim E_{\mathrm{p}}$, Eq. (2.3) can be changed as follow:

$$n(E)^2 \sim 1 + \frac{E_{\mathrm{d}}}{E_{\mathrm{p}} - E}. \tag{2.4}$$

Changing the temperature, the bandgap E_{g} of the material will change, and therefore the energy of an effective oscillator E_{p} will change similar to the bandgap. As a result, the dispersion of the refractive index will be shifted by the change of E_{p} which is caused by changing the temperature. In other words, the dispersion of the refractive index will be shifted by the change of the bandgap with a change in a temperature $\partial E_{\mathrm{g}}/\partial T$.

Replacing $B \equiv E_{\mathrm{d}}/E_{\mathrm{p}}$ and $C \equiv hc/E_{\mathrm{p}}$ where c is the velocity of light and h is Planck's constant and employing a constant A which represents other factors for the refractive index, we can obtain the following equation from Eq. (2.2):

$$n(\lambda)^2 = A + \frac{B\lambda^2}{\lambda^2 - C^2} \tag{2.5}$$

where λ is the light wavelength. This equation is known as the Sellmeier equation, which is based on an empirical relationship [14, 15]. This equation can be expanded as follow by assuming multiple oscillators:

$$n(\lambda)^2 = A + \sum_{j=1}^{k} \frac{B_j \lambda^2}{\lambda^2 - C_j^2}. \tag{2.6}$$

The thermo-optic coefficient $\partial n/\partial T$ can be given by differentiating the Sellmeier equation shown in Eq.(2.6) with respect to the temperature T:

$$\frac{\partial n}{\partial T} = -\frac{1}{2n} \sum_{j=1}^{k} \frac{B_j \lambda^2}{\lambda^2 - C_j^2} \frac{1}{E_{\mathrm{p},j}} \left(1 + \frac{2C_j^2}{\lambda^2 - C_j^2}\right) \frac{\partial E_{\mathrm{p},j}}{\partial T}. \tag{2.7}$$

Assuming long wavelength $\lambda \sim \infty$, the thermo-optic coefficient at the long-wavelength region can be expressed as

$$\frac{\partial n}{\partial T} \sim -\frac{1}{2n} \sum_{j=1}^{k} \frac{B_j}{E_{\mathrm{p},j}} \frac{\partial E_{\mathrm{p},j}}{\partial T}. \tag{2.8}$$

2.3 Experimental Procedure

Fig. 2.1 shows a schematic layout of the experimental setup for the measurement of the refractive index and its temperature dependence. Thin-film reflection interference spectrum was measured with a vertical-incidence configuration to determine the ordinary refractive index of the sample. A specular reflection probe (Ocean Optics QR450-7-XSR), which is a bundle comprising one optical fiber for light collection and six surrounding optical fibers for illumination, was used for the interference measurement. The optical fibers consisted of a pure silica core and fluorine-doped silica cladding. The light source was a combination of a deuterium lamp and a halogen lamp (Hamamatsu Photonics L10290). Three different spectrometers, which are based on a charge-coupled device (CCD), were employed to measure reflection spectra of the UV, visible, and IR regions (UV, Ocean Optics USB4000 with grating No. 5; visible, Ocean Optics USB4000 with grating No. 3; IR, Hamamatsu Photonics C9913GC). The entire range of measurement wavelengths was from 200 to 1700 nm. The wavelength errors determined from the line spectrum of mercury were less than 0.2 nm for the UV region, 0.5 nm for the visible region, and 0.8 nm for the IR region.

The measurement was performed at RT and elevated temperatures up to about 500°C utilizing a small hotplate. To perform high-temperature measurements with high uniformity and accuracy, the sample was set into a small self-made copper chamber with a 0.43-mm-thick sapphire window. The temperature of the copper chamber and that of the inside (atmosphere) of the chamber were measured by using type-K thermocouples (pairs of chromel and alumel). The temperature of the sample was between these two temperatures. The difference between these temperatures was confirmed to be less than 3°C even at 512°C, ensuring a good temperature uniformity within the measured sample. The error of type-K thermocouples used in this study (T. M. Electronics KA02) was ±0.25 %, and the error of the thermometer (Yokogawa Meters and Instruments TX1003) was ±(0.2 % + 1°C). Consequently, total error at 500°C was ±3.25°C, which was small enough for this study.

The reflection interference spectrum was measured in air. The reference of the reflectance was an aluminum-coated plane mirror. The distance between the sample and the reflection probe was about 20 mm. The refractive index dispersion curve was calculated from the peak and valley wavelengths of the interference with the layer thickness. Thin-film interference with vertical incidence is described as $2n(\lambda)t = m\lambda$, where λ is the wavelength of incident light, t is the thickness of the thin film, and m is the order of interference, as described in Appendix A. The refractive index of a substrate does not affect the calculation as long as the dispersion of the reflectance at the thin film/substrate interface is small enough. A

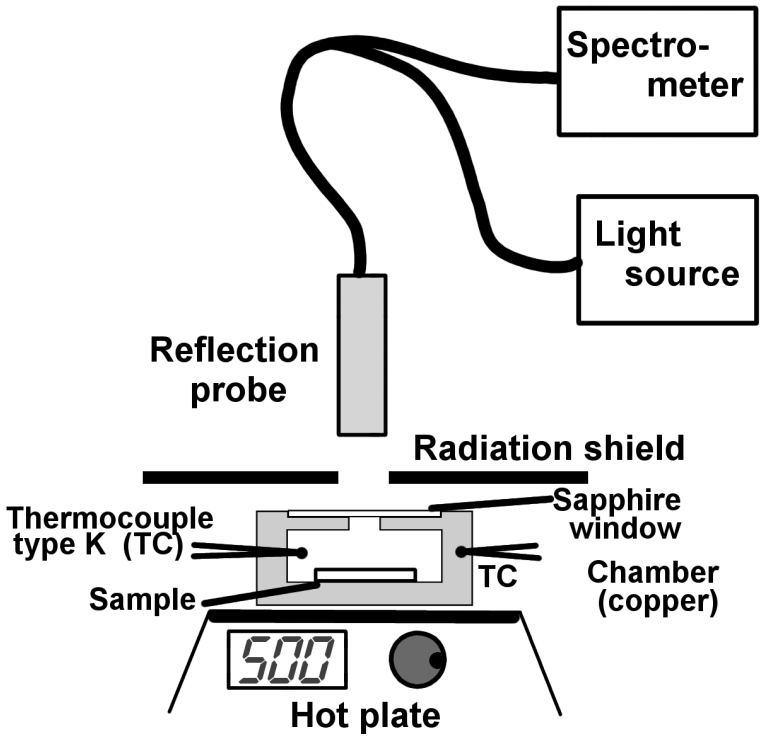

Figure 2.1: Schematic layout of experimental setup used for temperature-dependent interference spectrum measurement.

numerical simulation was performed, and the result confirmed that the effect of the substrate can be ignored for all samples in this study. Photoabsorption of the samples was ignored because the measurement wavelength was longer than the band-edge wavelength of each sample.

For elevated temperatures, the change of the layer thickness caused by the thermal expansion of both epitaxial layers and substrates was taken into account. The employed parameters [16–19] are summarized in Table 2.1. Since the strain state of epilayers depends on many factors, there should be an error in estimation of thickness change with temperature. However, even if the effect of the thermal expansion is ignored, difference in calculated thermo-optic coefficients is only 7 %. The error of thickness change therefore should have minor effect, i.e., much smaller than 7 %.

2.4 Sample Preparation

Thin-film interference spectra were measured to determine the dispersions of the refractive index of the samples. For the measurement, thin-film materials with uniform thickness are necessary. The samples used in this study are summarized in Table 2.2.

2.4.1 SiC

Commercially available single-crystalline 4H-SiC (0001) with 8°-off toward the [11-20] direction was used in this study. To realize thin-film interference measurement of 4H-SiC, a membrane structure of 4H-SiC was fabricated. The fabrication of the SiC membrane structure for pressure sensor application utilizing photoelectrochemical etching as a deep-etching method has been reported [20]. However, this conventional method is not suitable in this study because a membrane with high thickness uniformity, which is required for thin-film interference measurement, cannot be obtained. In this study, the doping-type selectivity of photoelectrochemical etching of SiC was utilized to fabricate such membrane structure.

Fabrication process of the membrane structure of 4H-SiC is shown in Fig. 2.2. Only n-type SiC was etched by this photoelectrochemical etching [21]. The detail of photoelectrochemical etching of SiC is described in Chapter 4. An n-type 4H-SiC substrate with a p-type 4H-SiC epitaxial layer was used for the fabrication. The doping concentration of the p-type epitaxial layer was 2.5×10^{16} cm^{-3}. Reactive ion etching was carried out from the backside [$(000\bar{1})$ face] to roughly remove the n-type SiC substrate, following which only the n-type SiC substrate was etched by photoelectrochemical etching. As a result, the p-type epitaxial layer remained as a membrane. Since the membrane was very fragile, it was impossible to measure the thickness by cross-sectional scanning electron microscopy (SEM) observation. The thickness of the SiC membrane was determined by fitting the obtained dispersion of the refractive index of SiC at RT to the reported data [22]. The determined thickness is 4.84 μm. This is a reasonable value since an estimated thickness of the p-type

Table 2.1: Parameters used in this study.

	Thermal expansion, a-axis (K^{-1})	Thermal expansion, c-axis (K^{-1})	Poisson's ratio
GaN	5.59×10^{-6} a)	3.17×10^{-6} a)	0.23 c)
AlN	4.2×10^{-6} a)	5.3×10^{-6} a)	0.287 a)
sapphire	7.5×10^{-6} b)		
6H-SiC	4.3×10^{-6} a)		
4H-SiC		4.06×10^{-6} d)	

a) Ref. 16, b) Ref. 17, c) Ref. 18, d) Ref. 19

Table 2.2: Samples used in this study.

	SiC (4H)	GaN	AlN
Thickness	4.84 μm	5.18 μm	9.23 μm
Substrate	Nothing (Air)	Sapphire	6H-SiC

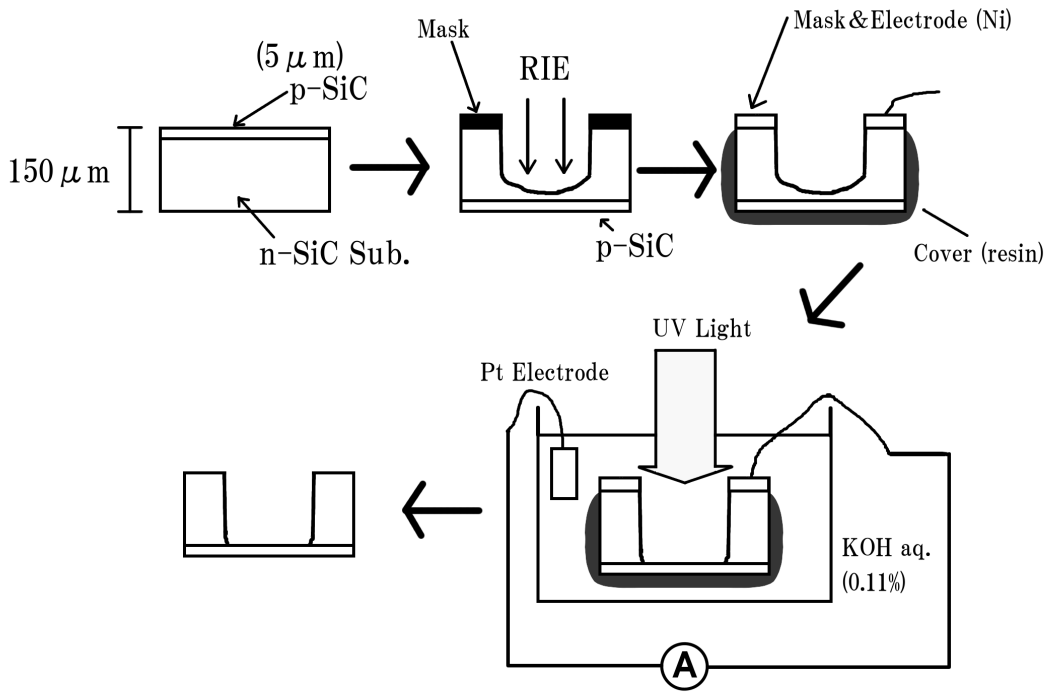

Figure 2.2: Fabrication process of an SiC membrane structure with uniform thickness by using photoelectrochemical (PEC) etching. Reactive ion etching is carried out from the backside to roughly remove the n-type SiC substrate, following which only the n-type SiC substrate is etched by PEC etching. As a result, the p-type epitaxial layer remains as a membrane.

epitaxial layer from its growth condition is 5 μm $\pm$ 10 %.

2.4.2 GaN and AlN

In group-Ⅲ nitrides, GaN and AlN, thin-film samples with uniform thickness are easily obtained by the heteroepitaxial growth. In this study, a commercially available GaN layer grown on a (0001)-oriented sapphire substrate by metal-organic vapor phase epitaxy (MOVPE) and an AlN layer grown on a (0001)-oriented 6H-SiC substrate by hydride vapor phase epitaxy (HVPE) were used. The thicknesses of the GaN and AlN layers are 5.18 and 9.23 μm, respectively. The thickness of the samples was determined by cross-sectional SEM using a magnification calibration standard (Geller Microanalytical Laboratory MRS-3). The uncertainty of the thickness measurement was less than 2 %.

2.5 Temperature Dependence of Refractive Index

2.5.1 SiC

Fig. 2.3(a) shows the measured dispersion curves of the refractive index of 4H-SiC at 26, 250, and 502°C in the wavelength range from 392 to 1700 nm. The data near 1400 nm were not obtained because of the absorption of optical fibers used in this study. At RT, the measured curve of SiC fairly agreed with the reported dispersion curve [22]. Especially in the near-band-edge region, as shown in the inset of Fig. 2.3(a), the dispersion curve of the refractive index of SiC shifted to longer wavelength with increasing temperature. As a result, the refractive index increases with increasing temperature at a certain wavelength. In Fig. 2.3(a), solid curves represent curve fits using the second-order Sellmeier equation [Eq. (2.6) with $k = 2$]. A good fitting was obtained at the wavelength region from near the band edge to 1000 nm. Since a good fitting was not obtained by the first-order Sellmeier equation, the second-order equation used to express the refractive index dispersion. The fitting parameters of the Sellmeier equation for the refractive index of SiC are listed in Table 2.3.

The refractive indices of 4H-SiC at 400, 450, 600, 800, and 1500 nm are plotted in Fig. 2.3(b) as a function of temperature. The refractive index increases almost linearly with increasing temperature up to 500°C, except for the near-band-edge region below 410 nm. It suggests that the thermo-optic coefficient of 4H-SiC can be calculated from the slope of the relation between the refractive index and the temperature in this temperature range except for the near-band-edge region.

The refractive index of 4H-SiC at RT after elevating temperature to 502°C was also measured and the result fairly agreed with the data at RT before heating, suggesting that SiC is thermally stable up to about 500°C and thus SiC can be used in such temperature range.

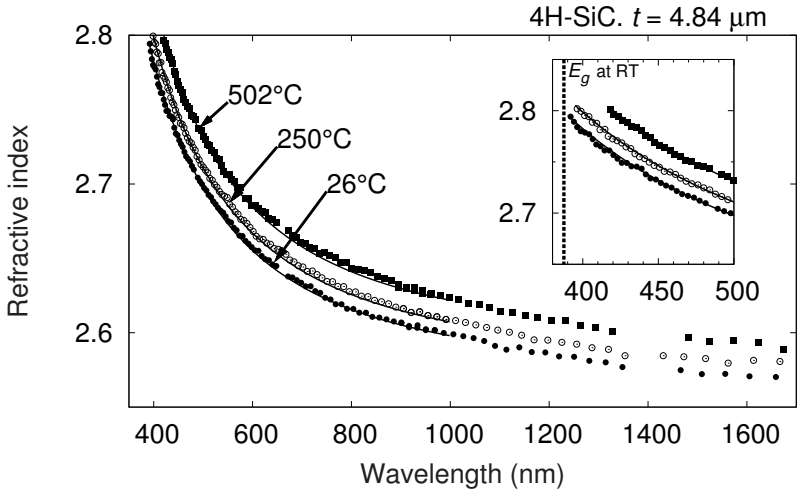

(a) Dispersions of refractive index

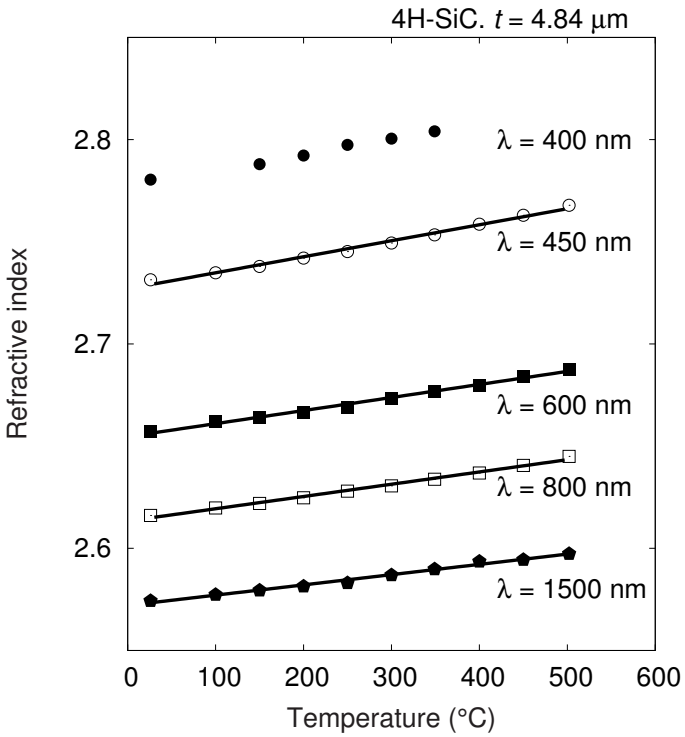

(b) Refractive indices as a function of temperature

Figure 2.3: (a) Dispersions of refractive index of 4H-SiC at room temperature and elevated temperatures. Solid curves represent curve fits to the Sellmeier equation [Eq. (2.6) with $k = 2$]. Inset shows the dispersion curves near the bandgap. (b) Refractive indices of 4H-SiC as a function of temperature at 400, 450, 500, 800, and 1500 nm. Solid lines are linear fits.

Table 2.3: Best-fit parameters of the second-order Sellmeier equation [Eq. (2.6) with $k = 2$] for refractive index of 4H-SiC at room temperature and elevated temperatures. The deduced refractive index of SiC from the Sellmeier equation with these parameters fairly agreed with measured data at the wavelength range from near the band edge to 1000 nm. Note that parameters A, B_1, and B_2 are dimensionless, while C_1 and C_2 are in nanometer units.

Temperature (°C)	A	B_1	C_1 (nm)	B_2	C_2 (nm)
26	4.667×10^{-4}	2.852	111.0	3.740	177.0
100	5.349×10^{-4}	3.131	108.5	3.475	182.5
150	5.184×10^{-4}	2.944	109.4	3.672	179.8
200	5.676×10^{-4}	3.029	108.2	3.598	182.2
250	3.292×10^{-4}	2.028	111.5	4.606	170.8
300	3.143×10^{-4}	1.707	112.0	4.941	167.9
349	3.014×10^{-4}	1.736	111.1	4.925	169.2
400	6.720×10^{-4}	3.438	102.7	3.244	193.9
450	2.430×10^{-4}	1.089	110.7	5.597	165.6
502	4.639×10^{-4}	2.747	105.6	3.955	185.1

2.5.2 GaN

Fig. 2.4(a) shows the measured dispersion curves of the refractive index of GaN at 24, 251, and 506°C in the wavelength range from 367 to 1700 nm. At RT, the measured curve of GaN fairly agreed with the reported dispersion curve [23, 24]. Closing to the band-edge region [shown in the insets of Fig. 2.4(a)], the change in the refractive index of GaN was relatively sharp compared with SiC [shown in the insets of Fig. 2.3(a)]. This result is related to the difference between the direct and indirect bandgaps. Similar to SiC, the dispersion curve of the refractive index of GaN shifted to longer wavelength with increasing temperature especially at the near-band-edge region, resulting in the increase of the refractive index at a certain wavelength. In Fig. 2.4(a), solid curves represent curve fits using the second-order Sellmeier equation. A good fitting was obtained at the wavelength region from near the band edge to 1000 nm. The fitting parameters of the Sellmeier equation for the refractive index of GaN are listed in Table 2.4.

The refractive indices of GaN at 380, 400, 500, 700, and 1500 nm are plotted in Fig. 2.4(b) as a function of temperature. The refractive index increases almost linearly with increasing temperature up to 500°C, except for the near-band-edge region below 420 nm. The thermo-optic coefficient of GaN can be calculated from the slope in this temperature range as well as that of SiC.

After elevating temperature, the refractive index of GaN at RT was measured again and the measured data was in good agreement with the data at RT before heating, confirming that GaN is thermally stable up to about 500°C.

2.5.3 AlN

Fig. 2.5(a) shows the measured dispersion curves of the refractive index of AlN at 24, 253, and 512°C in the wavelength range from 217 to 1700 nm. At RT, the measured curves of AlN fairly agreed with the reported dispersion curve [25]. The change in the refractive index of AlN by closing to the band edge, as shown in the insets of Fig. 2.5(a), was relatively sharp as well as that of GaN, compared with SiC. The dispersion curve of the refractive index of AlN shifted to longer wavelength with increasing temperature especially at the near-band-edge region, resulting in the increase of the refractive index at a certain wavelength. In Fig. 2.5(a), solid curves depict curve fits using the second-order Sellmeier equation. A good fitting was obtained at the wavelength region from near the band edge to 1000 nm. The fitting parameters of the Sellmeier equation for the refractive index of AlN are listed in Table 2.5. After elevating temperature, the refractive index of AlN at RT was measured again and the measured data was in good agreement with the data at RT before heating, confirming that AlN is thermally stable up to about 500°C.

The refractive indices of AlN at 220, 250, 300, 500, and 1500 nm are plotted in Fig. 2.5(b) as a function of temperature. The refractive index increases almost linearly with increasing temperature up to 500°C, except for the near-band-edge region below 230 nm. The thermo-

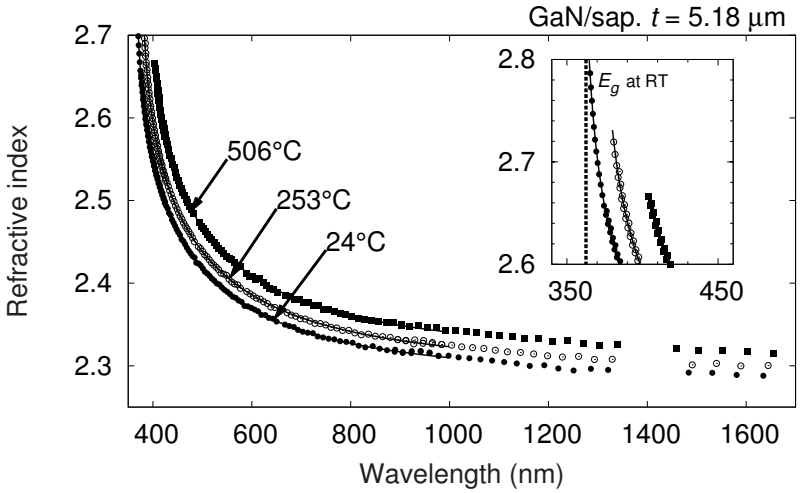

(a) Dispersions of refractive index

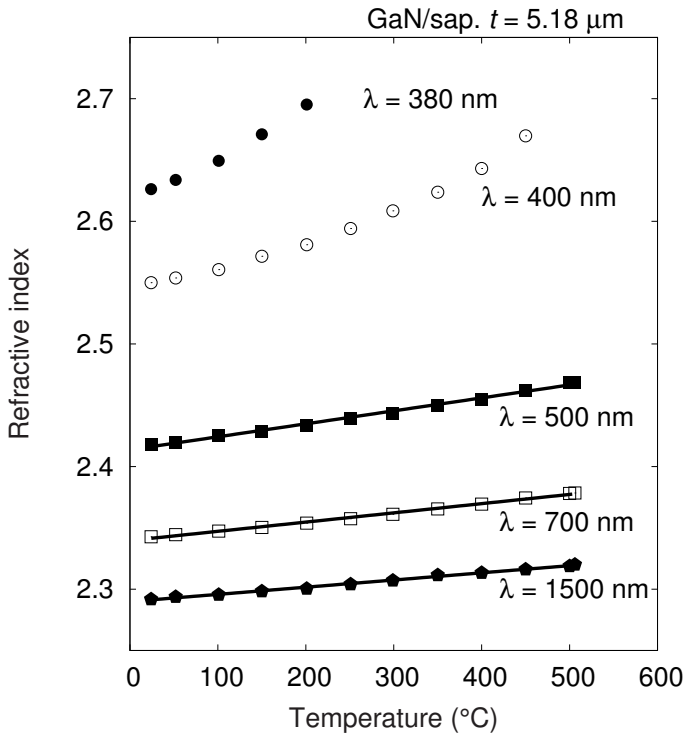

(b) Refractive indices as a function of temperature

Figure 2.4: (a) Dispersions of refractive index of GaN on a sapphire substrate at room temperature and elevated temperatures. Solid curves represent curve fits to the Sellmeier equation [Eq. (2.6) with $k = 2$]. Inset shows the dispersion curves near the bandgap. (b) Refractive indices of GaN as a function of temperature at 380, 400, 500, 700, and 1500 nm. Solid lines are linear fits.

Table 2.4: Best-fit parameters of the second-order Sellmeier equation [Eq. (2.6) with $k = 2$] for refractive index of GaN on a sapphire substrate at room temperature and elevated temperatures. The deduced refractive index of GaN from the Sellmeier equation with these parameters fairly agreed with measured data at the wavelength range from near the band edge to 1000 nm. Note that parameters A, B_1, and B_2 are dimensionless, while C_1 and C_2 are in nanometer units.

Temperature (°C)	A	B_1	C_1 (nm)	B_2	C_2 (nm)
24	2.880	2.260	225.4	0.06424	355.7
52	2.950	2.200	228.1	0.06286	357.1
101	2.574	2.566	213.6	0.08023	357.2
150	2.698	2.456	218.2	0.07992	359.4
201	2.574	2.588	214.9	0.08202	362.1
253	2.460	2.713	211.9	0.08345	364.9
299	2.278	2.900	206.5	0.09018	366.7
350	2.369	2.823	209.5	0.09256	369.1
400	2.393	2.817	211.5	0.08908	372.9
450	2.903	2.360	234.8	0.05284	382.7
506	2.177	3.054	207.3	0.09448	379.1

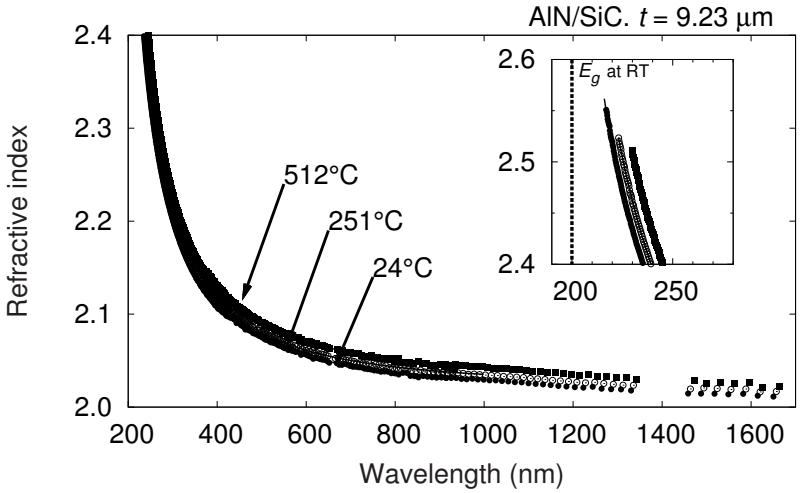

(a) Dispersions of refractive index

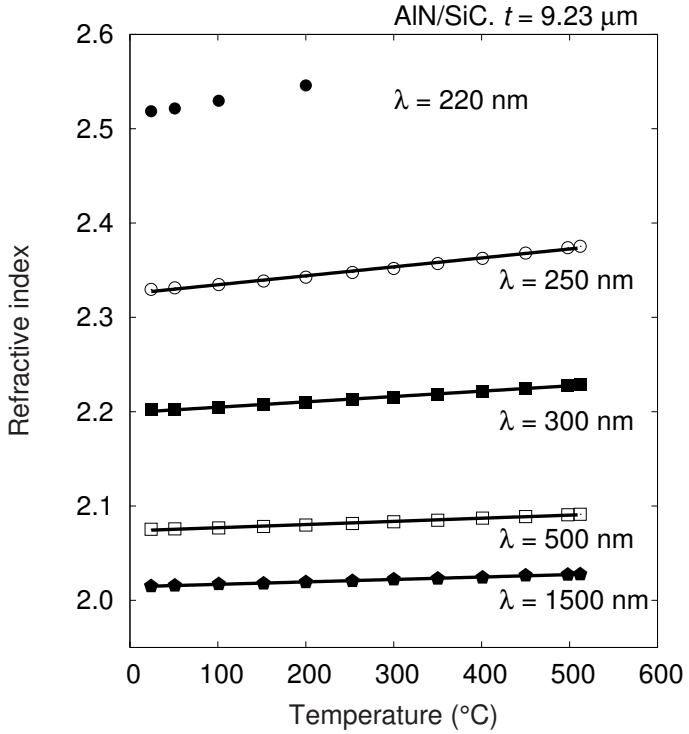

(b) Refractive indices as a function of temperature

Figure 2.5: (a) Dispersions of refractive index of AlN on an SiC substrate at room temperature and elevated temperatures. Solid curves represent curve fits to the Sellmeier equation [Eq. (2.6) with $k = 2$]. Inset shows the dispersion curves near the bandgap. (b) Refractive indices of AlN as a function of temperature at 220, 250, 300, 500, and 1500 nm. Solid lines are linear fits.

Table 2.5: Best-fit parameters of the second-order Sellmeier equation [Eq. (2.6) with $k = 2$] for refractive index of AlN on an SiC substrate at room temperature and elevated temperatures. The deduced refractive index of AlN from the Sellmeier equation with these parameters fairly agreed with measured data at the wavelength range from near the band edge to 1000 nm. Note that parameters A, B_1, and B_2 are dimensionless, while C_1 and C_2 are in nanometer units.

Temperature (°C)	A	B_1	C_1 (nm)	B_2	C_2 (nm)
24	0.1153	3.210	95.89	0.7400	180.5
51	0.5586	2.835	105.1	0.6732	181.8
101	0.1288	3.220	96.78	0.7223	181.7
152	0.07858	3.271	95.91	0.7260	182.3
200	1.021	2.507	117.6	0.5538	186.2
251	0.4656	2.994	105.371	0.6270	185.8
300	0.3141	3.124	102.1	0.6531	186.2
350	0.3621	3.103	103.5	0.6324	187.5
401	0.04695	3.417	98.79	0.6402	188.5
450	0.2930	3.215	103.9	0.6018	190.1
498	0.2028	3.333	103.5	0.5799	191.7
512	0.1702	3.373	103.4	0.5732	192.2

optic coefficient of AlN can be calculated from the slope in this temperature range as well as that of SiC and GaN.

2.5.4 Thermo-Optic Coefficients of SiC, GaN, and AlN

Fig. 2.6 shows the thermo-optic coefficients for 4H-SiC, GaN, and AlN obtained in this study. At 450 nm, the thermo-optic coefficients of 4H-SiC, GaN, and AlN were determined to be 7.8×10^{-5}, 1.6×10^{-4}, and 3.6×10^{-5} K^{-1}, respectively. The reported thermo-optic coefficients of 6H-SiC at a single wavelength of about 1.5 μm [9, 10] and the thermo-optic coefficient of GaN reported by Tisch and coworkers [11] are also plotted in Fig. 2.6. In the case of SiC, both of the reported values agree with the value determined in this work. The reported value of GaN, however, is larger than the experimental data in this study over the entire wavelength range. The discrepancy is probably attributed to the fact that Tisch *et al.* have not separated the ordinary (n_o) and extraordinary (n_e) indices in their measurements, while only the ordinary index has been evaluated in this study. Assuming that the data in both reports are accurate, it can be deduced that the thermo-optic coefficient $\partial n_e/\partial T$ is larger than $\partial n_o/\partial T$ in GaN.

For the temperature range from RT and 500°C and the wavelength ranges from 420, 450, and 250 to 1700 nm for SiC, GaN, and AlN, respectively, experimental polynomial fits of the thermo-optic coefficients were obtained as follows:

$$\partial n/\partial T(\lambda)_{\mathrm{SiC}} = 4.611 \times 10^{3}\lambda^{-3} - 1.446 \times 10^{1}\lambda^{-2} + 2.933 \times 10^{-2}\lambda^{-1} + 3.423 \times 10^{-5} \text{ (for 420-1700 nm)}, \quad (2.9)$$

$$\partial n/\partial T(\lambda)_{\mathrm{GaN}} = 3.800 \times 10^{4}\lambda^{-3} - 1.308 \times 10^{2}\lambda^{-2} + 1.634 \times 10^{-1}\lambda^{-1} - 2.957 \times 10^{-6} \text{ (for 450-1700 nm)}, \quad (2.10)$$

$$\partial n/\partial T(\lambda)_{\mathrm{AlN}} = 3.519 \times 10^{3}\lambda^{-3} - 1.656 \times 10^{1}\lambda^{-2} + 2.997 \times 10^{-2}\lambda^{-1} - 1.154 \times 10^{-5} \text{ (for 250-1700 nm)}. \quad (2.11)$$

The thermo-optic coefficient of different-thickness GaN, i.e., 10.6-μm-thick GaN, was also evaluated from near the band edge to 1000 nm. The result fairly agreed with that of 5.18-μm-thick GaN within 5 % error, implying an accurate and precise determination of the thermo-optic coefficient.

It is noted that the thermo-optic coefficients of GaN and AlN increased sharply as the wavelength approached the band edge, while the change in the thermo-optic coefficient of SiC was relatively gradual.

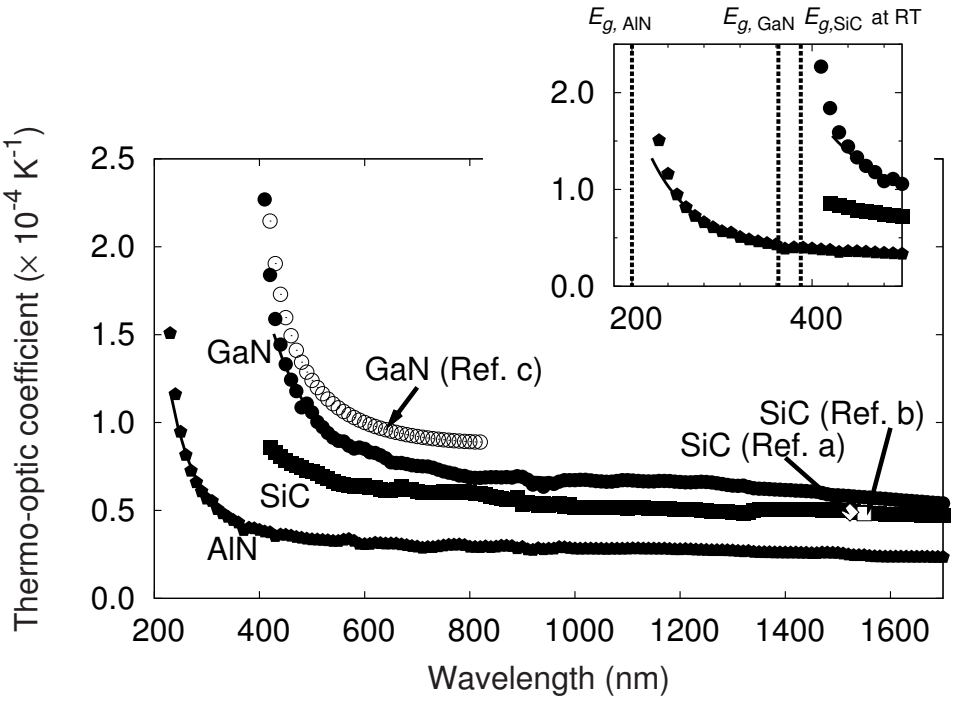

Figure 2.6: Thermo-optic coefficients of 4H-SiC, GaN, and AlN compared with reported data from Della Corte *et al.* (Ref. a) [9] and Riza *et al.* (Ref. b) [10] for 6H-SiC and Tisch *et al.* (Ref. c) for GaN [11]. Solid curves are polynomial fits of the thermo-optic coefficients of SiC, GaN and AlN from near the band edge (420, 450, and 250 nm for SiC, GaN, and AlN, respectively) to 1700 nm expressed in Eqs. (2.9), (2.10), and (2.11), respectively.

2.5.5 Discussion

At the near-band-edge region, the dispersion curves of the refractive index of SiC, GaN, and AlN were shifted to longer wavelength with increasing temperature. It is cause by the decrease of the bandgap of each material as indicated in Eq. (2.4). Nepal and coworkers reported the temperature dependence of the bandgap of GaN and AlN grown on sapphire substrates [26]. Based on this report, the redshifts at the band edge from 24 to 500°C are estimated to be 34 and 18 nm for GaN and AlN, respectively. For GaN, the shift of the dispersion curve of 32 nm, as shown in the inset of Fig. 2.4(a), is in good agreement with the result of Ref. 26. On the other hand, Fig. 2.5(a) depicts that the shift of the dispersion curve of AlN is 12 nm between 24 and 512°C, while the redshifts at the band edge is calculated to be 18 nm. The difference suggests different values of the built-in strain in AlN layers grown on different substrates. The AlN samples used in this study were grown on 6H-SiC, while sapphire substrates were used in Ref. 26.

As for SiC, the redshift from 26 to 500°C is estimated to be 23 nm at the band edge by the bandgap decrease [16]. As shown in the inset of Fig. 2.3(a), the shift of the dispersion curve of SiC was 43 nm, which is significantly larger than the estimated value. This disagreement is caused by the optical transition of SiC, i.e., indirect transition with phonon assistance. Dispersion of the refractive index near the band edge is determined by the interband transition, thus the temperature dependence of the refractive index dispersion of SiC is affected by the temperature effect on the phonon assistance. The temperature dependence of optical absorption in SiC is discussed in Chapter 3. The measurement in that chapter depicts that the dispersion curve of the absorption coefficient of SiC shifted to longer wavelength with increasing temperature and that the shift is larger than the redshift of the bandgap.

At the long-wavelength region, the thermo-optic coefficient is given by Eq. (2.8). Since the temperature dependence of E_p given by the obtained fitting parameter C of the Sellmeier equation is uncertain, $\partial E_\mathrm{p}/\partial T$ is assumed to be the same as the temperature dependence of the bandgap $\partial E_\mathrm{g}/\partial T$ for each material. In SiC, the average thermo-optic coefficient of each temperature is deduced to be 4.4×10^{-5} K^{-1} from Eq. (2.8) with parameters listed in Table 2.3. $\partial E_\mathrm{g}/\partial T$ of 4H-SiC have been employed to be -2.8×10^{-4} eV/K [16]. Note that $\partial E_\mathrm{g}/\partial T$ is assumed to be constant in this temperature range. In GaN and AlN, the average thermo-optic coefficients are deduced to be 6.2×10^{-5} K^{-1} and 8.4×10^{-5} K^{-1}, respectively, employing parameters listed in Tables 2.4 and 2.5. $\partial E_\mathrm{g}/\partial T_\mathrm{GaN} = -6.0 \times 10^{-4}$ eV/K and $\partial E_\mathrm{g}/\partial T_\mathrm{AlN} = -9.6 \times 10^{-4}$ eV/K [26] are employed for the deduction. The deduced thermo-optic coefficients of SiC and GaN at the long-wavelength region have fairly agreed with experimental data at 1700 nm, while that of AlN is significantly different from the experimental result. It is probably caused by the difference in the band edge. Since the Sellmeier equation is based on the oscillation at the band edge, the deduction should be inaccurate at the far-band-edge region. Larger bandgap of AlN (6.2 eV at RT) compared

with SiC and GaN (3.2 and 3.4 eV at RT, respectively) causes the failed deduction at the long-wavelength region.

At the near-band-edge region, the thermo-optic coefficients of GaN and AlN increased sharply as the wavelength approached the band edge. The change in the thermo-optic coefficient of SiC was, however, relatively gradual. In this region, the main origin of the thermo-optic coefficient is the redshift of the bandgap with increasing temperature. As mentioned above, the dispersion of the refractive index of SiC is much smaller than those of GaN and AlN, resulting in a small change in the thermo-optic coefficient with the change in wavelength.

The devices based on the thermo-optic effect, such as tunable filters, require a large thermo-optic coefficient. It can be realized using GaN, AlN, and AlGaN near the band edge. It is noted that the band edge of AlGaN can be tuned by adjusting the composition of AlGaN. On the other hand, SiC is more useful than GaN for the thermo-optic devices operated in a wide range of wavelengths because of the small dispersion of its thermo-optic coefficient.

2.6 Optical Simulation of GaN-Based Tunable Filters

2.6.1 Temperature Dependence of Transparent Wavelength

The temperature dependence of the transparent wavelength of band-pass filters based on Fabry-Pérot etalon can be deduce from the thermo-optic coefficient of a constituent material. As described in Appendix A, The phase difference δ between each succeeding reflection of a thin-film optical resonator with a vertical-incident configuration is

$$\delta = \frac{4\pi n d}{\lambda} \tag{2.12}$$

where n is the refractive index of the constituent material, d is the thickness of the thin-film resonator, and λ is the wavelength of incident light.

Differentiating this equation with respect to the temperature T,

$$\frac{\partial \delta}{\partial T} = \frac{4\pi d}{\lambda}\left(\frac{\partial n}{\partial T} - \frac{n}{\lambda}\frac{\partial \lambda}{\partial T} + \alpha n\right) \tag{2.13}$$

where α is the coefficient of thermal expansion ($\partial d/\partial T = \alpha t$). Considering the interference of the thin film at a certain order m, δ can be considered as a constant value, i.e., $\partial\delta/\partial T = 0$, and thus the following equation can be obtained:

$$\frac{\partial \lambda}{\partial T} = \frac{\lambda}{n}\frac{\partial n}{\partial T} + \alpha\lambda. \tag{2.14}$$

The amount of shift of the transparent wavelength of a tunable filter can be estimated with Eq. (2.14). It is noted that this estimation is rough since $\partial\lambda/\partial T$ is varied with changing

the wavelength especially at the near-band-edge region, where the thermo-optic coefficient $\partial n/\partial T$ sharply changes with changing the wavelength.

2.6.2 Simulation Details

The transmittance of a GaN-based optical band-pass filter was calculated at different temperatures, i.e., RT (21°C) and 500°C. The simulation was carried out with optical thin-film calculation software (Software Spectra TFCalc). Fig. 2.7 shows a schematic drawing of an optical filter used by the simulation. GaN was used as a resonator dielectric. To design the center of the transparent wavelength to 405.5 nm at RT, the thickness of the GaN resonator was determined to be 455 nm. $Al_xGa_{1-x}N$/GaN distributed Bragg reflectors (DBRs) were also used at the both side of the GaN resonator in order to enhance the finesse of the filter. $Al_xGa_{1-x}N$/GaN DBR can be formed simultaneously with a GaN dielectric by heteroepitaxial growth of group-Ⅲ nitrides. The DBRs consisted of the 50-pair of 42.77-nm-thickness $Al_{0.34}Ga_{0.66}N$ and 40.62-nm-thickness GaN.

In the previous section, the refractive indices and the thermo-optic coefficients of GaN and AlN have been determined. However, the refractive index of $Al_xGa_{1-x}N$ for each temperature are required for the calculation. To interpolate the temperature dependence of $Al_xGa_{1-x}N$, the following procedure is employed. By comparing the curves of the thermo-optic coefficients of GaN and AlN in Fig. 2.6, the curve moves to the shorter wavelength and also moves to the smaller value from GaN to AlN. The blueshift corresponds to difference of the bandgaps of GaN and AlN. To estimate the curve for $Al_xGa_{1-x}N$, the curve of GaN was shifted to shorter wavelength corresponding to the difference of the bandgaps of GaN and $Al_xGa_{1-x}N$. Brunner and coworkers have extensively studied the refractive index of $Al_xGa_{1-x}N$ at RT [27]. I utilized their data as the refractive index of $Al_xGa_{1-x}N$ at RT.

2.6.3 Simulation Results

The simulation results of the transmittance spectrum are shown in Fig. 2.8. The width of pass band was about 0.1 nm. The redshift of the transparent wavelength from RT to 500°C was calculated to be about 9 nm, which is much larger than the width of pass band. Although temperature dependence of transmittance spectrum depends on the structures of filters, the simulation results show that temperature-controlled tunable optical filters are possible in GaN systems with high performance and high tunability for applications which require high resolution, e.g., Raman spectroscopy.

2.6.4 Discussion

The estimated shift of the transparent wavelength from Eq. (2.14) between RT and 500°C is 15 nm. Since the wavelength used in this simulation is near the band edge of GaN, this

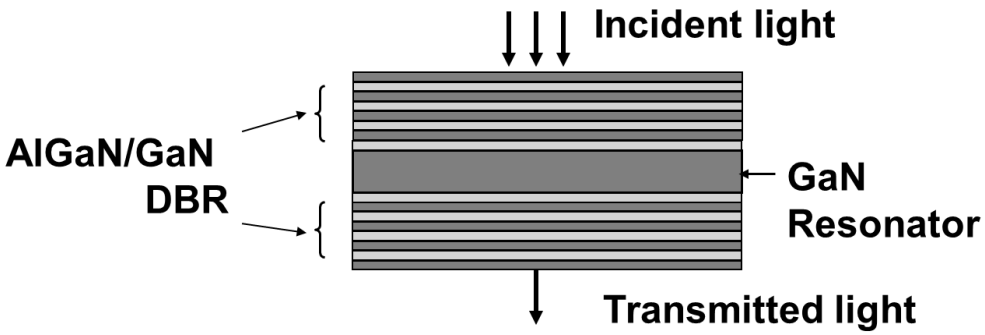

Figure 2.7: Schematic drawing of GaN tunable band-pass filter used in the simulation. $Al_xGa_{1-x}N$/GaN distributed Bragg reflectors (DBRs) are also used at the both side of the GaN resonator in order to enhance the finesse of the filter.

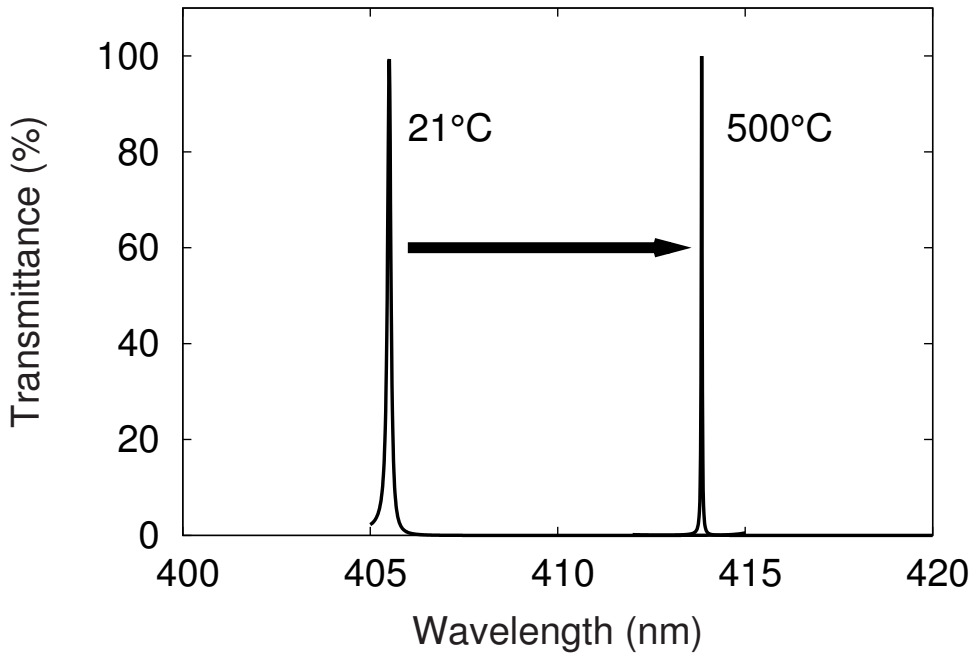

Figure 2.8: Simulation results of the transmittance of GaN tunable band-pass filter. The transparent wavelength of the filter is shifted to longer wavelength with about 9 nm, which is much larger than the width of pass band (~ 0.1 nm).

estimated value is larger than the simulation result. However, these results are in rough agreement, suggesting that the simulation have been carried out precisely.

It is noted that the curve shapes of the transmittance spectrums at RT and 500°C were slightly different in Fig. 2.8. It is probably caused by the difference of reflection characteristics of AlGaN/GaN DBRs at these temperatures. It suggests that the temperature dependence of constituent DBRs of a filter should be also considered for precise design of optical tunable filers.

2.7 Summary

I measured the temperature dependence of the refractive indices of 4H-SiC, GaN, and AlN from RT to 500°C over a wide spectral range from 1700 nm to near the bandgaps of each material. The thermo-optic coefficients for the ordinary refractive indices of 4H-SiC, GaN, and AlN were accurately determined over a wide temperature range. The results obtained thus far are useful for the design of GaN-based optoelectronic devices as well as SiC- and GaN-based wavelength-tunable band-pass filters and photonic crystals that actively utilize the thermo-optic effect operating from IR to UV regions.

A GaN-based optical band-pass filter simulation was also conducted at different temperatures by utilizing the determined thermo-optic coefficients of GaN and AlN. The simulation has demonstrated that the modulation of the transparent wavelength of a filter can be suitable for tunable filter application.

In the future, extraordinary index measurements will be needed for complete characterization of thermo-optic coefficients. The determination for AlGaN will also be needed for the design of GaN-based devices. Eventually, wide-bandgap-semiconductor tunable filters should be realized.

References

[1] G. Hatakoshi, M. Onomura, M. Yamamoto, S. Nunoue, K. Itaya, and M. Ishikawa, Jpn. J. Appl. Phys. **38**, 2764 (1999).

[2] S. Nakamura, T. Mukai, and M. Senoh, Jpn. J. Appl. Phys. **30**, L1998 (1991).

[3] S. Nakamura, M. Senoh, S. Nagahama, N. Iwase, T. Yamada, T. Matsushita, H. Kiyoku, and Y. Sugimoto, Jpn. J. Appl. Phys. **35**, L74 (1996).

[4] S. Sota, H. Sakai, T. Tanaka, M. Koike, and H. Amano, Electron. Lett. **32**, 1105 (1996).

[5] Y. Taniyasu, M. Kasu, and T. Makimoto, Nature **441**, 325 (2006).

[6] J. Edmond, H. Kong, A. Suvorov, D. Waltz, and C. Carter, *Jr.*, Phys. Stat. Sol. A **162**, 481 (1997).

[7] M. De Vittorio, B. Potì, M. T. Todaro, M. C. Frassanito, A. Pomarico, A. Passaseo, M. Lomascolo, and R. Cingolani, Sens. Actuators A **113**, 329 (2004).

[8] D. Hohlfeld and H. Zappe, J. Opt. A **6**, 504 (2004).

[9] F. G. Della Corte, G. Cocorullo, M. Iodice, and I. Rendina, Appl. Phys. Lett. **77**, 1614 (2000).

[10] N. A. Riza, M. Arain, and F. Perez, J. Appl. Phys. **98**, 103512 (2005).

[11] U. Tisch, B. Meyler, O. Katz, E. Finkman, and J. Salzman, J. Appl. Phys. **89**, 2676 (2001).

[12] S. Yamada, B. S. Song, T. Asano, and S. Noda, Appl. Phys. Lett. **99**, 201102 (2011).

[13] S. H. Wemple and M. DiDomenico, *Jr.*, Phys. Rev. B **3**, 1338 (1971).

[14] D. T. F. Marple, J. Appl. Phys. **35**, 539 (1964).

[15] B. Tatian, Appl. Opt. **23**, 4477 (1984).

[16] M. E. Levinshtein, S. L. Rumyantsev, and M. S. Shur (*eds.*), *Properties of Advanced Semiconductor Materials: GaN, AlN, InN, BN, SiC, SiGe*, (John Wiley & Sons, Toronto, 2001).

[17] K. Hiramatsu, T. Detchprohm, and I. Akasaki, Jpn. J. Appl. Phys. **32**, 1528 (1993).

[18] C. Kisielowski, J. Krüger, S. Ruvimov, T. Suski, J. W. Ager, Ⅲ, E. Jones, Z. Liliental-Weber, M. Rubin, and E. R. Weber, Phys. Rev. B **54**, 17745 (1996).

[19] Z. Li and R. C. Bradt, J. Appl. Phys. **60**, 612 (1986).

[20] R. S. Okojie, A. A. Ned, and A. D. Kurtz, Sens. Actuators A **66**, 200 (1998).

[21] J. S. Shor, A. D. Kurtz, I. Grimberg, B. Z. Weiss, and R. M. Osgood, J. Appl. Phys. **81**, 1546 (1997).

[22] P. T. B. Shaffer, Appl. Opt. **10**, 1034 (1971).

[23] G. Yu, G. Wang, H. Ishikawa, M. Umeno, T. Soga, T. Egawa, J. Watanabe, and T. Jimbo, Appl. Phys. Lett. **70**, 3209 (1997).

[24] N. A. Sanford, L. H. Robins, A. V. Davydov, A. Shapiro, D. V. Tsvetkov, A. V. Dmitriev, S. Keller, U. K. Mishra, and S. P. DenBaars, J. Appl. Phys. **94**, 2980 (2003).

[25] Y. Huttel, H. Gomez, A. Cebollada, G. Armelles, and M. I. Alonso, J. Cryst. Growth **242**, 116 (2002).

[26] N. Nepal, J. Li, M. L. Nakermi, J. Y. Lin, and H. X. Jiang, Appl. Phys. Lett. **87**, 242104 (2005).

[27] D. Brunner, H. Angerer, E. Bustarret, F. Freudenberg, R. Höpler, R. Dimitrov, O. Ambacher, and M. Stutzmann, J. Appl. Phys. **82**, 5090 (1997).

Chapter 3

Determination of Absorption Coefficients of SiC for High-Temperature Photodetector Design

3.1 Introduction

Ultraviolet sensors which can operate in a wide temperature range, e.g., from room temperature (RT) to 500°C, are required for harsh-environment sensing applications. A silicon carbide (SiC) pn photodiode is one of promising candidates for such sensors. There are some reports on SiC photodiodes operating at elevated temperature [1–4]. However, the photodiodes showed strong temperature dependence of photoresponse. In many applications, operating temperature varies. In the case, the knowledge of the temperature dependence of photoresponse is strongly required to assure precise sensing.

The temperature dependence of the photoresponse is mainly determined by the change of the optical absorption coefficient of the constituent material. Knowledge of the temperature dependence of the absorption coefficient is therefore necessary to design high-performance photodiodes properly. However, investigations of the absorption coefficients of SiC are very limited. Groth and Kauer have investigated the absorption coefficient of 6H-SiC between RT and 1500°C up to about 100 cm^{-1} [5], and Pikhtin and Yas'kov have reported the data of 6H-SiC between -178 and 300°C up to about 60 cm^{-1} [6]. Although these studies are very useful because they have investigated the fundamental absorption edge of 6H-SiC, the data in shorter wavelength range are required to design photodetectors made of SiC. The absorption coefficient of 4H-SiC, which is mainly investigated as the material for SiC semiconductor devices, is also important while these report did not target. Another group reported the absorption coefficient of 3C-, 4H-, and 6H-SiC from about 300 to 390 nm [7]. Their work revealed the data in the wide range of wavelengths. However, they reported the data at only

RT. To design high-temperature SiC pn photodiodes, it is necessary to reveal the absorption coefficient of SiC at high temperature in the wide wavelength range, especially shorter wavelength regions. In this chapter, I have determined the optical absorption coefficients of 4H- and 6H-SiC from RT up to 300°C by transmission measurement.

3.2 Theoretical Model

Optical absorption can be described as the optical transition at the fundamental absorption edge. Optical absorption coefficient α is

$$\alpha = -\frac{dI}{dx} \cdot \frac{1}{I} \tag{3.1}$$

where x is the position from the surface of incidence and I is the light intensity at x. $-dI/dx$ means the decay rate of the intensity per unit time, and it can be described as the product of transition probability W and photon energy $h\nu$. I is given by the Poynting vector, hence it is proportional to the square of the frequency of the light ν. α is therefore expressed as the following equation:

$$\alpha \propto W/h\nu. \tag{3.2}$$

In SiC, a photon can excite an electron from the valence band to the conduction band with the assistance of a phonon because of the indirect bandgap. The transition probability can be given by this equation [8]:

$$W = \frac{4\pi^2}{h} \sum_{\boldsymbol{k}_\mathrm{c},\boldsymbol{k}_\mathrm{v}} \left| \sum_i \frac{\langle f|\mathscr{H}_\mathrm{ep}|i\rangle\langle i|\mathscr{H}_\mathrm{eR}|0\rangle}{E_{\mathrm{i}0} - h\nu} \right|^2 \delta(E_\mathrm{c}(\boldsymbol{k}_\mathrm{c}) - E_\mathrm{v}(\boldsymbol{k}_\mathrm{v}) - h\nu \pm E_\mathrm{p}). \tag{3.3}$$

$|0\rangle$ represents the initial state of the transition, $|f\rangle$ is the final state, and $|i\rangle$ is the intermediate state. This transition step involves the electron–photon interaction $\mathscr{H}_\mathrm{eR}$ and the electron–phonon interaction $\mathscr{H}_\mathrm{ep}$.

The photon energy dependence of W can be obtained by summing over the delta function in Eq. (3.3). By converting the summations over $\boldsymbol{k}_\mathrm{c}$ and $\boldsymbol{k}_\mathrm{v}$ to integrations over the conduction and valence band energies E_c and E_v, respectively, and assuming that the bands are parabolic and three-dimensional, this equation can be expressed as

$$W \propto (h\nu \pm E_\mathrm{p} - E_\mathrm{g})^2 \tag{3.4}$$

where E_p is the phonon energy and E_g is the bandgap. Every indirect energy gap gives rise to two absorption edges for each phonon, at $E_\mathrm{g} - E_\mathrm{p}$ corresponds to phonon absorption and $E_\mathrm{g} + E_\mathrm{p}$ to phonon emission.

From Eqs. (3.2) and (3.4), the change of the absorption coefficient by changing the temperature is caused by the change of the bandgap. In other words, the bandgap of the

material is changed by changing the temperature, following which the dispersion of the absorption coefficient is shifted by the change of the band edge.

However, there is another temperature effect on the absorption coefficient of SiC. The electron–phonon matrix element $\langle f|\mathscr{H}_{\rm ep}|i\rangle$ in Eq. (3.3) is proportional to $N_{\rm p}$ and $N_{\rm p}+1$ for phonon absorption and emission, respectively, where $N_{\rm p}$ phonon occupation number expressed as

$$N_{\rm p} \propto 1/[\exp(E_{\rm p}/kT) - 1] \tag{3.5}$$

where k is the Boltzmann constant and T is the temperature. Obviously, $N_{\rm p}$ will change by changing the temperature.

Combining Eqs. (3.2), (3.4), and (3.5), the absorption coefficient can be described as following equation with a fitting parameter A:

$$\alpha = \frac{A}{h\nu}\left[\frac{(h\nu - E_{\rm g} + E_{\rm p})^2}{\exp(E_{\rm p}/kT) - 1} + \frac{(h\nu - E_{\rm g} - E_{\rm p})^2}{1 - \exp(-E_{\rm p}/kT)}\right]. \tag{3.6}$$

In addition, free exciton formation with absorption and emission of the corresponding phonons should be considered at the fundamental absorption edge [6]. Optical absorption of excitons by indirect transition can be expressed as [9]

$$\alpha_{\rm exciton} = \frac{B}{h\nu}\left[\frac{(h\nu - E_{\rm gx} + E_{\rm p})^{\frac{1}{2}}}{\exp(E_{\rm p}/kT) - 1} + \frac{(h\nu - E_{\rm gx} - E_{\rm p})^{\frac{1}{2}}}{1 - \exp(-E_{\rm p}/kT)}\right] \tag{3.7}$$

where $E_{\rm gx}$ is the exciton gap ($E_{\rm gx} = E_{\rm g} - E_{\rm ex}$: $E_{\rm ex}$ is the exciton binding energy) and B is the fitting parameter. Therefore, the absorption coefficient of SiC can be determined by summing Eqs. (3.6) and (3.7) for each phonon which assists the transition.

3.3 Experimental Procedure

The absorption coefficients of SiC were determined by making measurements with the transmitted light propagating parallel to the c-axis. The transmission measurement was carried out using a spectrophotometer (Shimadzu UV-3100). Fig. 3.1 shows a schematic diagram of the measurement instrument [10]. As shown in Fig. 3.1, two beam branches, the reference branch and the sample branch, were used for the measurement. By taking the ratio of the two beams at each wavelength, the effect of the fluctuations in the deuterium and halogen light sources can be eliminated.

The measurement was carried out at RT and elevated temperature up to 300°C utilizing a self-made sample holder with a small ceramic heater. Fig. 3.2 shows a schematic drawing of the setup to make the absorption measurement at elevated temperatures. To perform high-temperature measurement with high uniformity and accuracy, the sample was set into a small copper chamber with 0.5-mm-thick sapphire windows. The temperature of the copper

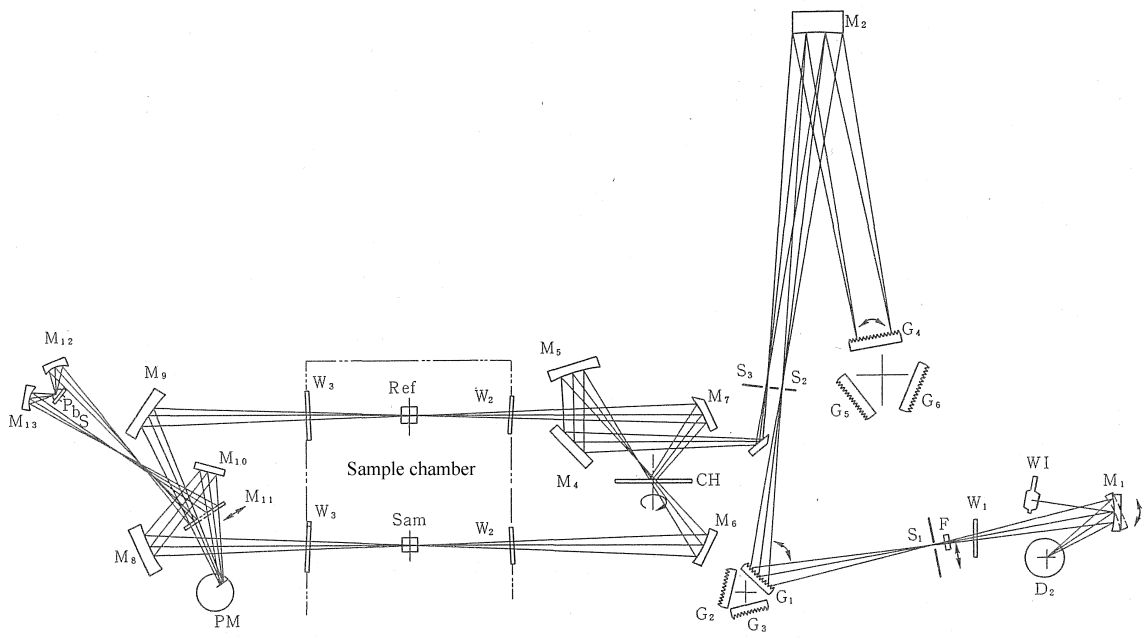

D_2	:	Deuterium Lamp
WI	:	Halogen Lamp
F	:	Filter
G_1 - G_6	:	Gratings
S_1 - S_3	:	Slits
W_1 - W_3	:	Windows
CH	:	Chopper
M_1 - M_{13}	:	Mirrors
Ref	:	Reference branch
Sam	:	Sample branch
PM	:	Photomultiplier
PbS	:	PbS Cell

Figure 3.1: Schematic diagram of a spectrophotometer (Shimadzu UV-3100) used to make the transmission measurement [10].

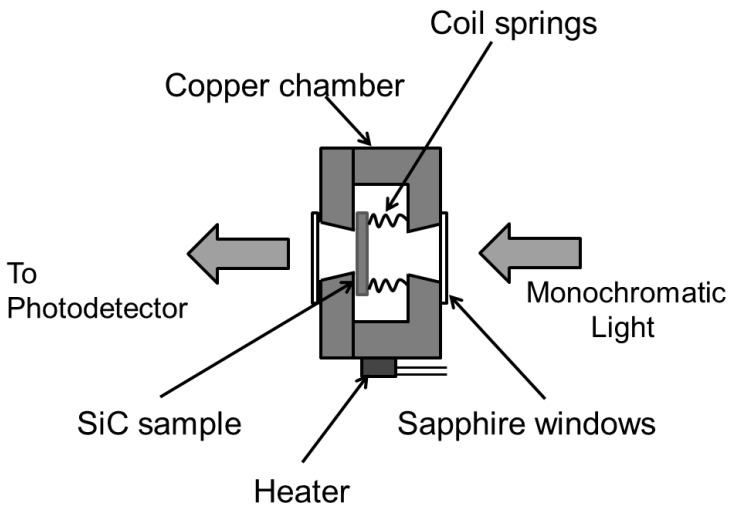

Figure 3.2: Schematic drawing of the setup to make the absorption measurement at elevated temperatures. A small copper chamber enables to carry out the high-temperature measurement with high uniformity and accuracy.

chamber and that of the inside (atmosphere) of the chamber were measured using type-K thermocouples (pairs of chromel and alumel). The temperature of the sample should be between these two temperatures. The difference between these temperatures was confirmed to be less than 3°C even at 300°C, ensuring a good temperature uniformity within the measured sample. The error of type-K thermocouples used in this study (T. M. Electronics KA02) was ±0.25 %, and the error of the thermometer (Yokogawa Meters and Instruments TX1003) was ±(0.2 % + 1°C). Consequently, total error at 300°C was ±2.35°C, which was small enough for this study.

The transmittance spectrum was measured in air. To avoid the effect of the incident reflection and scattering at the surface and reflection at the sapphire windows of a copper chamber, transmittance of two samples with different thickness were measured. The absorption coefficient can be calculated using the following equation as described in Appendix B:

$$\alpha = \frac{1}{d_2 - d_1} \ln\left(\frac{T_1}{T_2}\right) \tag{3.8}$$

where α is the absorption coefficient, d_1 and d_2 are the thickness of each sample, and T_1 and T_2 are measured transmittance values.

In the calculation, change of the layer thickness caused by the thermal expansion was taken into account. The thermal expansion coefficients of 4H- and 6H-SiC paralleled to the c-axis are 4.06×10^{-6} K^{-1} [11] and 4.7×10^{-6} K^{-1} [12], respectively.

3.4 Sample Preparation

The samples used in this study were commercially available single crystalline semi-insulating 4H- and 6H-SiC (0001) on-axis substrates. To obtain samples with various thicknesses, mechanical polishing from the backside [$(000\bar{1})$ face] was carried out. The thickness of the samples was determined by a digimatic indicator (Mitutoyo ID-C112X). In this study, 4H-SiC samples with thickness of 109 and 181 μm and 6H-SiC samples with thickness of 154 and 202 μm were prepared. The samples are summarized in Table 3.1.

3.5 Temperature Dependence of Absorption Coefficients of SiC

3.5.1 4H-SiC

Fig. 3.3 shows the measured dispersion curve of the absorption coefficient of 4H-SiC at 26, 100, 200, and 300°C. The reported data at RT [7] fairly agreed with measured data. The dispersion curve shifted to longer wavelength with increasing temperature. As a result, at a fixed wavelength, the absorption coefficient increased. As described in Section 3.2, this shift is mainly caused by the change of the bandgap by changing the temperature. However, the

Table 3.1: Samples used in this study.

	4H-SiC	6H-SiC
Thickness No. 1	109 μm	154 μm
Thickness No. 2	181 μm	202 μm
Thermal expansion, c-axis	4.06×10^{-6} K^{-1} a)	4.7×10^{-6} K^{-1} b)

a) Ref. 11, b) Ref. 12

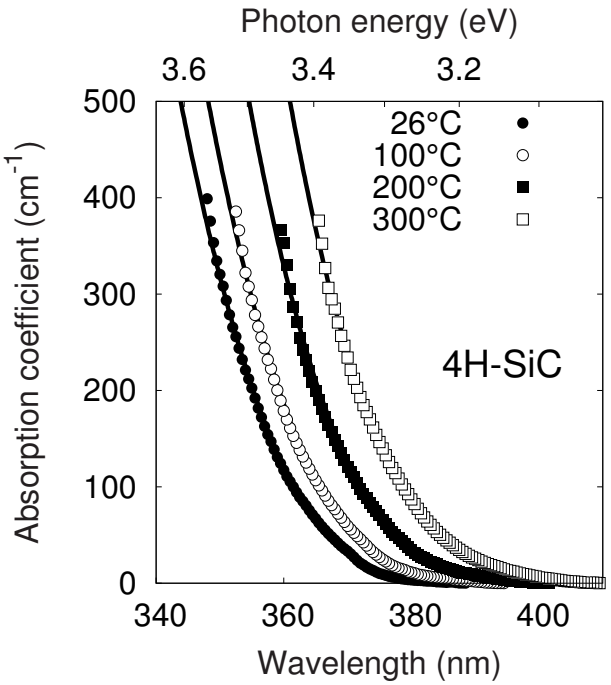

Figure 3.3: Absorption spectra of 4H-SiC at room temperature and elevated temperatures. Solid curves show deduced dispersions from Eqs. (3.6) and (3.7) with the best-fit parameters listed in Table 3.2.

dispersion shift at 300 cm^{-1} was -5.8×10^{-4} eV/K while the change of the bandgap was -2.8×10^{-4} eV/K between 26 and 300°C [12]. The comparison of the absorption spectra of 4H-SiC at RT, at 300°C, and at RT with −77 meV shift, i.e., the bandgap decrease of 4H-SiC from RT to 300°C, is shown in Fig. 3.4. As shown in Fig. 3.4, the absorption spectrum of 4H-SiC at 300°C is larger than the estimated data from the data at RT with the bandgap decrease. This disagreement suggests that the change of the phonon occupation by changing the temperature significantly affects the temperature dependence of the absorption coefficient of 4H-SiC.

3.5.2 6H-SiC

Fig. 3.5 shows the measured dispersion curve of the absorption coefficient of 6H-SiC at 26, 100, 200, and 300°C. The dispersion curves agreed with reported data of the fundamental absorption edge [5–7]. Similar to 4H-SiC, the dispersion curve shifted to longer wavelength with increasing temperature, and the dispersion shift (-5.9×10^{-4} eV/K at 300 cm^{-1}) did not agree with the change of the bandgap (-3.0×10^{-4} eV/K between 26 and 300°C [12]). The comparison of the absorption spectra of 6H-SiC at RT, at 300°C, and at RT with −82 meV shift, which is the bandgap decrease of 6H-SiC from RT to 300°C, is shown in Fig. 3.6. Similar to the result of 4H-SiC shown in Fig. 3.4, the absorption spectrum of 6H-SiC at 300°C is larger than the estimated data from the data at RT with the bandgap decrease. This result suggests that the temperature dependence of the absorption coefficient of 6H-SiC is also effectively affected by the change of the phonon occupation.

3.5.3 Discussion

As shown in Figs. 3.4 and 3.6, the absorption coefficients of both 4H- and 6H-SiC at elevated temperatures are larger than those estimated by the data at RT and the bandgap decrease. These results suggest that the temperature dependence of the absorption coefficient of both 4H- and 6H-SiC is affected by the change of the phonon occupation. As described in Eq. (3.5), the phonon occupation number N_{p} increases with increasing temperature. The increase of N_{p} enhances the absorption coefficient of SiC, resulting in the larger absorption coefficient at elevated temperatures.

The report shows that fundamental absorption edge of 6H-SiC at RT and elevated temperatures shows phonon interaction of TA-, LA-, and TO-mode as shown in Fig. 3.7 [6]. Hence curve fitting to the measured data was carried out using Eqs. (3.6) and (3.7) with TA-, LA-, and TO-mode phonons. The energy of TA-, LA-, and TO-mode phonons are 46.7, 76.9, and 95.0 meV for 4H-SiC [13], and those of 6H-SiC are 46.3, 77.0, and 94.7 meV [14]. The results of the fitting are shown in Figs. 3.3 and 3.5 as solid curves. The best-fit parameters of the fitting are listed in Tables 3.2 and 3.3 for 4H- and 6H-SiC, respectively. The bandgap E_{g} and the exciton gap E_{gx} of 4H- and 6H-SiC used for the fitting at each

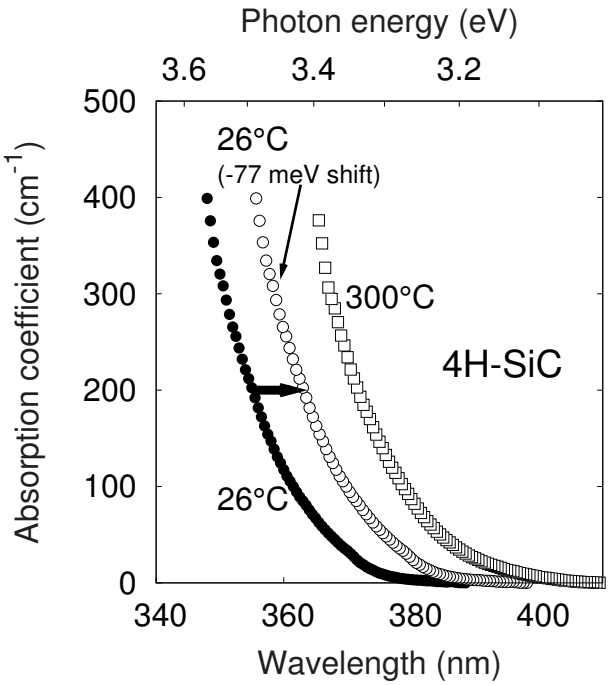

Figure 3.4: Absorption spectra of 4H-SiC. Filled circles show the absorption spectrum at room temperature (RT), open circles show that at RT with -77 meV shift, which is the decrease of the bandgap of 4H-SiC from RT to 300°C, and open squares show the absorption spectrum at 300°C. The absorption spectrum at 300°C is larger than the estimated data from the data at RT with the bandgap decrease.

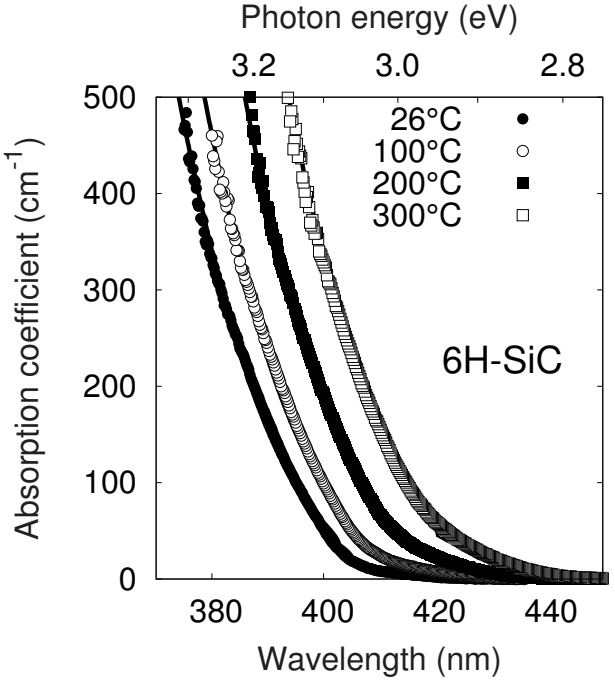

Figure 3.5: Absorption spectra of 6H-SiC at room temperature and elevated temperatures. Solid curves show deduced dispersions from Eqs. (3.6) and (3.7) with the best-fit parameters listed in Table 3.3.

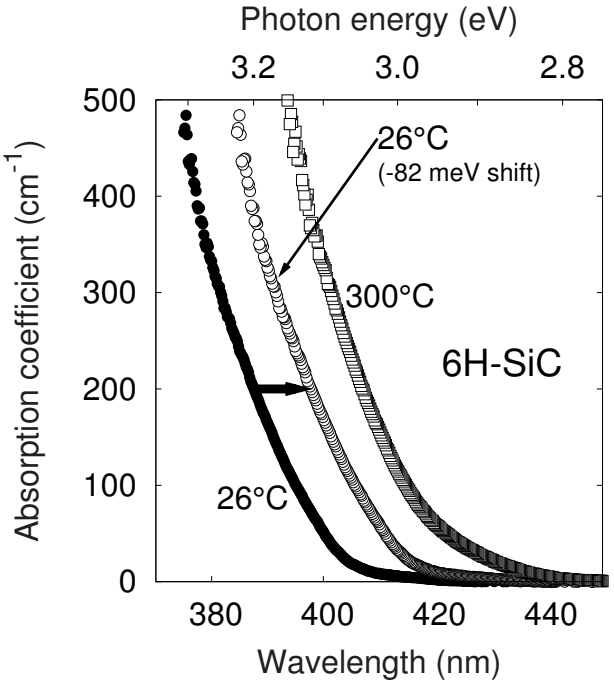

Figure 3.6: Absorption spectra of 6H-SiC. Filled circles show the absorption spectrum at room temperature (RT), open circles show that at RT with −82 meV shift, which is the decrease of the bandgap of 6H-SiC from RT to 300°C, and open squares show the absorption spectrum at 300°C. The absorption spectrum at 300°C is larger than the estimated data from the data at RT with the bandgap decrease.

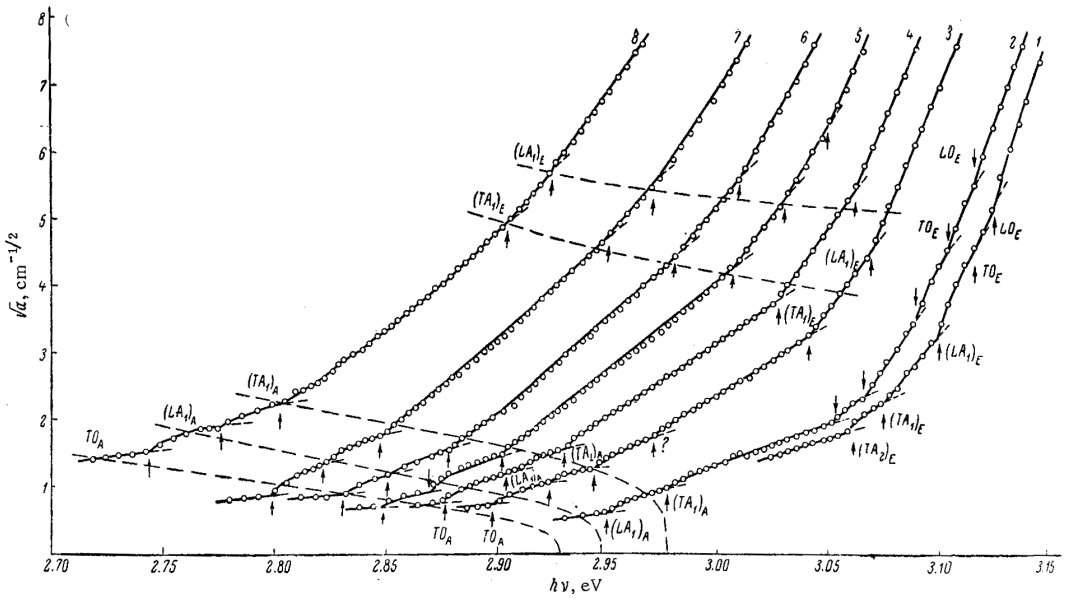

Figure 3.7: Fundamental absorption edge of 6H-SiC at various temperature. 1) −178°C, 2) −63°C, 3) 22°C, 4) 67°C, 5) 120°C, 6) 167°C, 7) 217°C, and 8) 300°C [6].

Table 3.2: Best-fit parameters of Eqs. (3.6) and (3.7) for the absorption coefficient of 4H-SiC with TA-, LA-, and TO-mode phonons (E_p = 46.7, 76.9, and 95.0 meV, respectively). The fitting is carried out with the equation which is determined by summing Eqs. (3.6) and (3.7) for each phonon. Note that parameter A of each phonon is in $\mathrm{eV}^{-1} \cdot \mathrm{cm}^{-1}$, while B is in $\mathrm{eV}^{0.5} \cdot \mathrm{cm}^{-1}$. E_g and E_gx are the bandgap and the exciton gap of 4H-SiC, respectively [12], both of which are fixed in the fitting.

T (°C)	E_p = 46.7 meV		E_p = 76.9 meV		E_p = 95.0 meV		E_g (eV)	E_gx (eV)
	A	B	A	B	A	B		
26	2500	50	3000	80	14000	150	(3.256)	(3.229)
100	2500	50	3000	80	15000	190	(3.238)	(3.211)
200	2500	60	3000	90	16000	250	(3.210)	(3.183)
300	2500	60	3000	90	16500	300	(3.178)	(3.151)

Table 3.3: Best-fit parameters of Eqs. (3.6) and (3.7) for the absorption coefficient of 6H-SiC with TA-, LA-, and TO-mode phonons (E_p = 46.3, 77.0, and 94.7 meV, respectively). The fitting is carried out with the equation which is determined by summing Eqs. (3.6) and (3.7) for each phonon. Note that parameter A of each phonon is in $\mathrm{eV}^{-1} \cdot \mathrm{cm}^{-1}$, while B is in $\mathrm{eV}^{0.5} \cdot \mathrm{cm}^{-1}$. E_g and E_gx are the bandgap and the exciton gap of 6H-SiC, respectively [12], both of which are fixed in the fitting.

T (°C)	E_p = 46.3 meV		E_p = 77.0 meV		E_p = 94.7 meV		E_g (eV)	E_gx (eV)
	A	B	A	B	A	B		
26	2000	150	9000	200	11000	250	(3.011)	(2.984)
100	2000	160	9000	210	11000	260	(2.993)	(2.966)
200	2000	180	9000	230	11000	280	(2.963)	(2.936)
300	2000	200	9000	250	11000	300	(2.930)	(2.903)

temperature are also listed in Tables 3.2 and 3.3 [12]. Measured data were fairly fitted at elevated temperatures as well as at RT, suggesting that the absorption coefficients of both 4H- and 6H-SiC can be deduced with TA-, LA-, and TO-mode-phonon interactions in this temperature range and wavelength range. It is noted that a good fitting of the absorption coefficients of both 4H- and 6H-SiC could not be obtained by considering only interband transition, i.e., employing only Eq. (3.6), especially at the fundamental absorption edge. It suggests that the absorption spectrum of SiC at fundamental absorption edge is determined by exciton transitions, which suggestion agrees with the report [6].

As listed in Tables 3.2 and 3.3, the fitting parameters of Eqs. (3.6) and (3.7) were weakly temperature-dependent, indicating that the electron–phonon interaction for each phonon slightly changes by changing the temperature.

The measured data in this study, however, does not satisfy to utilize for SiC photodetector design. 4H-SiC photodetectors, for example, are used at shorter wavelength, around 300 nm because of the higher quantum efficiency [15]. At shorter wavelength region, optical absorption caused by direct transition will be occurred. Therefore the absorption coefficient of SiC at that region cannot be predicted precisely from the current data. To determine the temperature dependence of the absorption coefficient of SiC at shorter wavelength region, thinner samples should be used for the transmission measurement because of the larger absorption coefficient.

3.6 Summary

In this chapter, I determined the temperature dependence of the absorption coefficient of 4H- and 6H-SiC between RT and 300°C up to about 400 cm^{-1} (4H-SiC) and 500 cm^{-1} (6H-SiC). Redshift of the absorption edge at elevated temperature was observed. This redshift is mainly caused by the bandgap decrease with increasing temperature. Temperature dependence of the phonon occupation number is also significant to explain the temperature dependence of the absorption coefficient of SiC. Employing TA-, LA-, and TO-mode phonons, the measured data were fairly fitted with the theoretical equation.

Although the measured data is not enough to design SiC photodetectors, this study demonstrated that the temperature dependence of the absorption coefficient of SiC can be determined precisely in a wide range of wavelengths with the transmission measurement. In the future, the data at the shorter-wavelength region should be determined by measuring thinner samples, and the design of SiC photodetector can be realized.

References

[1] R. B. Campbell and H. C. Chang, Solid State Electron. **10**, 949 (1967).

[2] P. Glasow, G. Ziegler, W. Suttrop, G. Pensl, and R. Helbig, Proc. SPIE **868**, 40 (1987).

[3] D. M. Brown, E. T. Downey, M. Ghezzo, J. W. Kretchmer, R. J. Saia, Y. S. Liu, J. A. Edmond, G. Gati, J. M. Pimbley, and W. E. Schneider, IEEE Trans. Electron Devices **40**, 325 (1993).

[4] J. Edmond, H. Kong, A. Suvorov, D. Waltz, and C. Carter, *Jr.*, Phys. Stat. Sol. A **162**, 481 (1997).

[5] R. Groth and E. Kauer, Phys. Stat. Sol. **1**, 445 (1961).

[6] A. N. Pikhtin and D. A. Yas'kov, Phys. Tverd. Tela **12**, 1597 (1970).

[7] S. G. Sridhara, T. J. Eperjesi, R. P. Devaty, and W. J. Choyke, Mater. Sci. Eng. B **61-62**, 229 (1999).

[8] P. Y. Yu and M. Cardona, *Fundamentals of Semiconductors, 3rd ed.*, (Springer, Berlin, 2005).

[9] R. J. Elliott, Phys. Rev. **108**, 1384 (1957).

[10] UV-3100 Instruction Manual, Shimadzu

[11] Z. Li and R. C. Bradt, J. Appl. Phys. **60**, 612 (1986).

[12] M. E. Levinshtein, S. L. Rumyantsev, and M. S. Shur (*eds.*), *Properties of Advanced Semiconductor Materials: GaN, AlN, InN, BN, SiC, SiGe*, (John Wiley & Sons, Toronto, 2001).

[13] L. Patrick, W. J. Choyke, and D. R. Hamilton, Phys. Rev. **137**, A1515 (1965).

[14] W. J. Choyke, D. R. Hamilton, and L. Patrick, Phys. Rev. **133**, A1163 (1964).

[15] H. -Y. Cha, S. Soloviev, S. Zelakiewicz, P. Waldrab, and P. M. Sandvik, IEEE Sens. J. **8**, 233 (2008).

Chapter 4

Fabrication of Single-Crystalline SiC MEMS Structures for Harsh-Environment Operation

4.1 Introduction

Microelectromechanical systems (MEMS) have attracted much attention as integrated components of miniaturized mechanical structures with microelectronics, mainly for sensing and actuating applications. A large number of sensors and actuators are utilized in many environments, and a demand has emerged, demand which is the usage in harsh environments characterized as locations of high temperature, high pressure, strong radiation, and corrosive environments. MEMS devices operating in harsh environments are required in many applications such as automobile, aerospace, nuclear, and chemical industries. However, silicon (Si), the most conventional material employed in MEMS devices [1], cannot be used as a structural material of MEMS devices operated in harsh environments because of its characteristic limitations. Therefore, materials which can stand up with harsh environments are required for such MEMS applications.

Silicon carbide (SiC) is one of the most promising structural materials of MEMS devices in harsh environment because of its superior characteristics. SiC has large bandgap which enables the MEMS devices to be used in high temperature, high power, and strongly radiative environments. SiC is also mechanically strong, having large Young's modulus and large yield strength even in a high temperature environment. Furthermore, SiC has great inertness to most corrosive chemicals. Consequently, there have been various studies on SiC-based MEMS devices for operating in harsh environments [2–4].

In the most of the studies about SiC MEMS, SiC films which are amorphous [5], polycrystalline [6, 7], or relatively high-defect-density heteroepitaxial layers (3C-SiC) grown on Si substrates [8] were utilized. These SiC films convey many advantages compared with Si. However, single-crystalline SiC free of structural defects is expected to convey far su-

perior device performance. MEMS devices with high-quality single-crystalline SiC should extend the range of applicability of harsh-environment MEMS. Furthermore, the other constituent components of thin-film SiC MEMS devices, e.g., substrates and spacer layers, are commonly fabricated with conventional structural materials. Even if SiC films can resist harsh environmental conditions, the actual range of operating conditions is restricted by the limitations of the conventional materials. To operate under more extreme environments that only SiC can withstand, the MEMS devices should be composed entirely of single-crystalline SiC, i.e., homoepitaxial SiC layers on SiC substrates.

Although all-single-crystalline SiC MEMS have great potentials as described above, it is difficult to fabricate devices composed entirely of SiC because of its chemical inertness and mechanical hardness. Okojie and coworkers reported piezoresistive pressure sensors entirely composed of bulk single-crystalline 6H-SiC [9]. The device was free from the mismatch of thermal expansion coefficient between a substrate and a membrane, and could be operated up to 500°C. However, there have been no reports of all-single-crystalline SiC MEMS devices with electrostatic actuation which requires the devices to have suspended plates or beams with sub-micron-scale separation from the substrate. In addition, mechanical characteristics, e.g., resonance characteristics, of all-single-crystalline SiC MEMS devices have not been investigated in detail.

In this chapter, I have fabricated all-single-crystalline SiC suspended structures by utilizing photoelectrochemical (PEC) and electrochemical (EC) etching, these which have doping-sensitive selectivity. Electrostatic actuation of fabricated double-clamped bridge structures has been demonstrated in this study. I have also evaluated resonance characteristics of fabricated single-clamped cantilever structures to demonstrate the advantage of all-single-crystalline SiC MEMS devices.

4.2 Single-Crystalline SiC Bridge/Cantilever Structure

4.2.1 Design of Structure

In this study, I have fabricated bridge (double-clamped beam) and cantilever (single-clamped beam) structures using single-crystalline 4H-SiC. To design 4H-SiC bridge structure for demonstrating electrostatic actuation properly, structural analysis of the structures was carried out with the finite element method (FEM) using CoventorWare 2010 software. The structure used in this simulation is shown in Fig. 4.1. Only the bridge structure was allowed to move and the bridge was fixed at the anchors. The length of the bridge was 50 μm, the width was 2 and 5 μm, the thickness was 100, 300, and 500 nm, and the gap between the bridge and the bottom was 600 nm. Applying the voltage between the bridge and the bottom, the bridge was deformed by the Coulomb force.

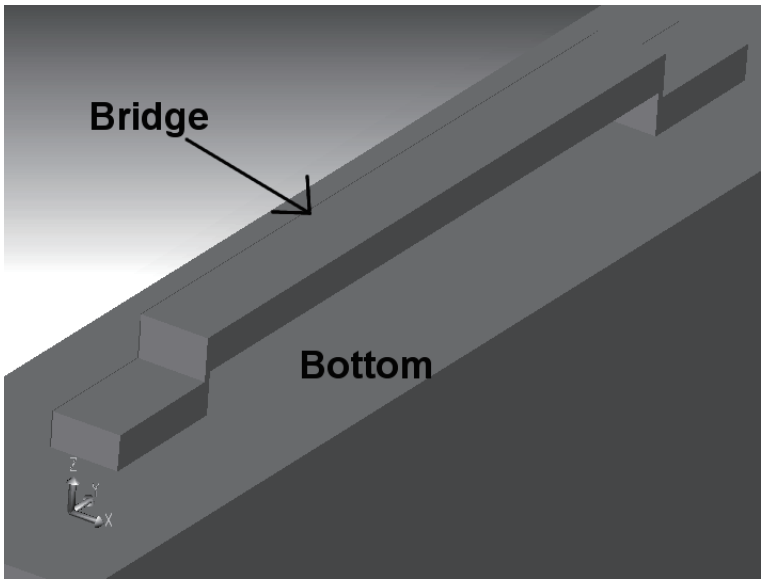

Figure 4.1: Structure model of the SiC bridge structure used for the structural analysis of electrostatic actuation. The dimensions of the bridge are defined as the length (parallel to y-axis), the width (parallel to x-axis), and the thickness (parallel to z-axis). Only the bridge structure is allowed to move and the bridge is fixed at the anchors.

The relationship between maximum displacement and the applied voltage was calculated with FEM simulation. In this simulation, the material properties of SiC were employed as follows: the density of SiC was 3.22 g/cm^3 and the Young's modulus was 448 GPa [10]. The result is shown in Fig. 4.2. As shown in Fig. 4.2, the displacement of the bridge increased with increasing applied voltage. From the simple parallel-plate model as described in Appendix C, the stability limit of the displacement can be expressed as

$$\delta = h/3 \tag{4.1}$$

where δ is the displacement and h is the distance between two plates. Employing this stability limit for the electrostatic actuation of this bridge structure, the bridge is pulled in to the bottom when the displacement becomes over 200 nm. The sharp increase of the displacement of the bridge over 200 μm shown in Fig. 4.2 indicates this stability limit. When the displacement reaches the stability limit, the applied voltage is given by this equation:

$$V_{\mathrm{p}} = \left(\frac{256 d^3 h^3 E}{27 \epsilon_0 l^4} \right)^{\frac{1}{2}} \tag{4.2}$$

where d is the thickness of the bridge, l is the length, E is the Young's modulus of the material, and ϵ_0 is the vacuum permittivity. As shown in Fig. 4.2, the applied voltage at the displacement of the stability limit (200 nm) increases with increasing the thickness of the bridge. The applied voltage is roughly proportional to $d^{1.4}$, which is in good agreement with $d^{1.5}$ derived from Eq. (4.2). On the other hand, from Eq. (4.2), the applied voltage at the displacement of the stability limit does not depend on the width of the bridge while the displacement is slightly changed by changing the width from the simulation, especially in high-voltage region. This is probably caused by the difference between the simple parallel plate structure and the double-clamped bridge structure. However, the width dependence is small and negligible in the low-voltage region as shown in Fig. 4.2. This simulation result properly depicts the electrostatic actuation of SiC bridge structure.

From the simulation result, SiC bridge structure with the length of 50 μm, the width of 5 μm, the thickness of 100 nm, and the distance of 600 nm from the bottom can be electrostatically actuated properly by applying the voltage under 10 V. To operate with moderate operating voltage, the electrostatic-actuating SiC bridge structure should be designed with such dimensions.

As for the resonant frequency, the following equation gives the n-th resonant frequency of flexural vibration of suspended beam structure as described in Appendix C:

$$f_n = X_n \frac{d}{2\pi l^2} \sqrt{\frac{E}{\rho}} \tag{4.3}$$

where X_n is the coefficient determined by the structure and the order of the resonance, and ρ is the density of the material. For the double-clamped bridge and single-clamped cantilever structures, X_1 is 6.459 and 1.015, respectively. Employing the dimensions of $l = 100$ μm

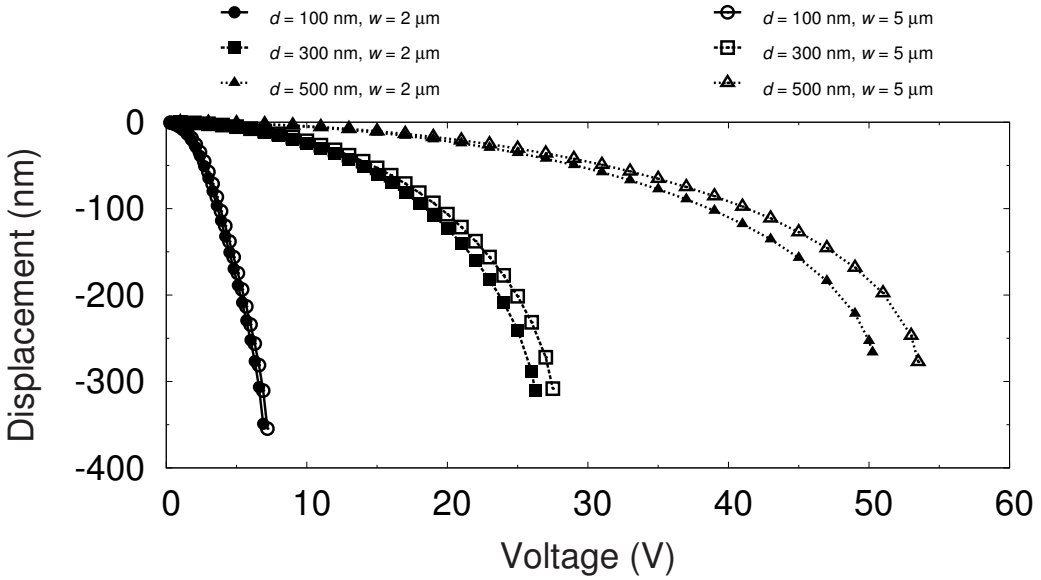

Figure 4.2: FEM simulation result of the displacement of the SiC bridge structure as a function of applied voltage. The length of the bridge is 50 μm, the width is 2 μm (filled symbols) and 5 μm (open), and the thickness is 100 nm (circle symbols), 300 nm (square), and 500 nm (triangle). The gap between the bridge and the bottom is 600 nm.

and $d = 900$ nm, first-mode resonant frequencies of SiC MEMS structures are derived to be 1.09 MHz for the double-clamped bridge and 171 kHz for the single-clamped cantilever.

4.2.2 Fabrication Process

To fabricate suspended beam structure of the length of 50-100 μm and sub-micron-thickness as described above, device patterning and sacrificial-layer etching are necessary. Device pattern formation with transferring photolithographically formed pattern can be realized utilizing dry etching process. In SiC, reactive ion etching (RIE) has been employed for fabricating SiC electronic devices and thus SiC MEMS pattern also can be formed by this process.

On the other hand, sacrificial-layer etching in all-single-crystalline SiC MEMS fabrication is difficult. Typical sacrificial-layer process, for example, deposition of poly-SiC on a substrate with an insulating sacrificial layer such as silicon dioxide (SiO_2) followed by sacrificial etching, cannot be employed for all-single-crystalline SiC MEMS fabrication. Only a targeted layer should be etched in stacked structure entirely composed of SiC. There are fundamental studies on PEC etching, a doping-sensitive selective wet etching under illumination with above-band-gap light [11–13]. Etching selectivity in doping type of SiC can lead to sacrificial-layer etching of all-single-crystalline SiC structure since SiC pn-stacking structure can be easily formed by homoepitaxial growth or ion implantation. And there is another possible SiC etching process which can realize sacrificial-layer etching. EC etching of p-type SiC has been reported recently [14, 15]. This EC etching of SiC is also expected to have doping-type selectivity as well as PEC etching.

4.3 Etching Processes for SiC MEMS Fabrication

4.3.1 Reactive Ion Etching

RIE is a key process in the semiconductor industry. As well as electronic devices, microstructures are commonly formed by this technology. RIE involves the generation of chemically reactive ions which are accelerated by an electric field toward a target substrate. The reactive ions are generated by the collision of molecules in a plasma-state reactant gas. The cloud of energetic electrons is excited by an RF electric field. In RIE, ion motion toward the substrate is almost vertical thus RIE has vertical anisotropy. This vertical anisotropy contributes to transferring photolithographically formed pattern to the target substrate.

RIE process for SiC has been investigated since 1980's [16]. Reactant gases commonly used for RIE of SiC are fluorine-based [e.g., tetrafluoromethane (CF_4) and sulfur hexafluoride (SF_6)] and chlorine-based [e.g., chlorine (Cl_2) and silicon tetrachloride ($SiCl_4$)] gases. The improvement in the etching rate of SiC by mixing oxygen gas (O_2) with a reactant gas was reported [17]. High-rate etching of SiC up to 2.7 μm/min was demonstrated using

SF_6 + O_2 mixture gas [18]. Device patterns of thin-film SiC MEMS devices have been formed by RIE [6, 7], as well as SiC semiconductor devices such as mesa-type pn diodes [19].

4.3.2 Photoelectrochemical Etching

PEC etching is an electrochemical etching of SiC. This includes two reactions, oxidation and dissolution. The oxidation reaction of PEC etching of SiC can be described as following chemical equations:

$$\mathrm{SiC} + 4\mathrm{H_2O} + 8\mathrm{h^+} \rightarrow \mathrm{SiO_2} + \mathrm{CO_2} + 8\mathrm{H^+}, \tag{4.4}$$

$$\text{or,} \quad \mathrm{SiC} + 2\mathrm{H_2O} + 4\mathrm{h^+} \rightarrow \mathrm{SiO} + \mathrm{CO} + 4\mathrm{H^+}. \tag{4.5}$$

As shown in these equations, hole carriers (h^+) are required for the reaction. In PEC etching, these holes are supplied by generating hole-electron pairs with light absorption. Illuminating ultraviolet (UV) light above bandgap energy (3.23 eV for 4H-SiC), the light is absorbed into SiC and carriers are generated. The dissolution reaction is caused by the etchant of PEC etching. Hydrogen fluoride (HF) or potassium hydroxide (KOH) solutions are typically used for the etchant.

PEC etching of SiC has selectivity between doping types, i.e., p-type and n-type. N-type SiC is selectively removed by PEC etching. This selectivity is caused by the difference of band bending at p-type and n-type SiC/electrolyte interface. The mechanism of the selectivity is shown in Fig. 4.3. These figures show the band structures of p-type and n-type SiC. Illuminating above bandgap light, carriers are generated in the space-charge regions of both p-type and n-type SiC. Generated holes in p-type SiC are drifted into the SiC while those in n-type SiC are drifted into the electrolyte. PEC etching is occurred only in n-type SiC because the PEC etching reaction requires hole carriers as indicated in Eqs. (4.4) and (4.5).

The etching rate of PEC etching can be deduced from the current density of the electrochemical reaction by utilizing Faraday's laws of electrolysis. For the reaction represented by Eq. (4.4), the required number of hole carriers to oxidize SiC is given by

$$N_{\mathrm{h^+}} = \frac{3.21V}{40} \times 8 \tag{4.6}$$

where $N_{\mathrm{h^+}}$ is in mole units, V is the volume of SiC, 3.21 g/cm^3 represents the SiC density, 40 is the molecular mass of SiC. The current flowed in the reaction can be expressed as

$$I = \frac{N_{\mathrm{h^+}} e N_{\mathrm{A}}}{t} \tag{4.7}$$

where e is the elementary charge, N_{A} is the Avogadro constant, and t is the etching time. The etching rate v can be expressed with the etching depth d and the etching time, i.e.,

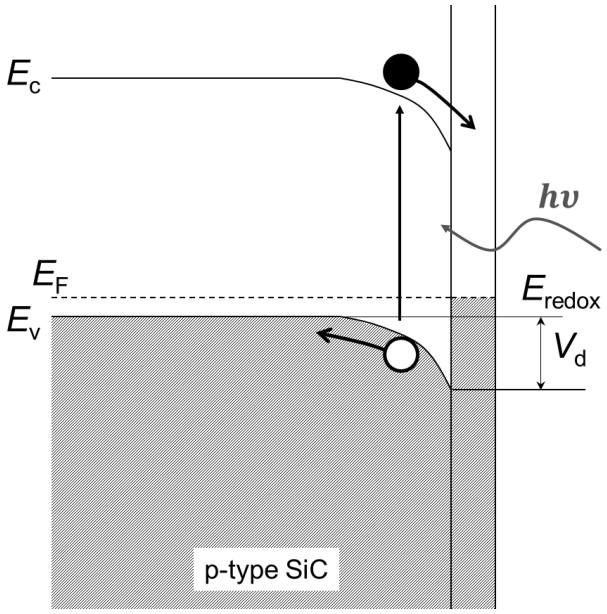

(a) p-type SiC

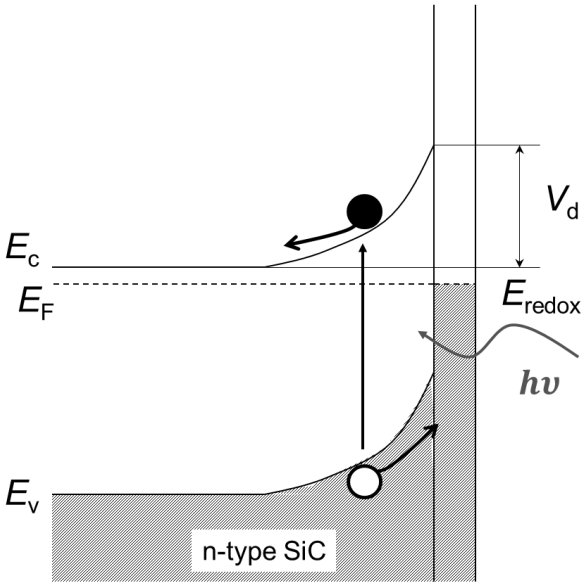

(b) n-type SiC

Figure 4.3: Band structures of (a) p-type and (b) n-type SiC at the interface of electrolyte. Illuminating above bandgap light, carriers are generated. Generated holes in p-type SiC are drifted into the SiC while those in n-type SiC are drifted into the electrolyte. Photo-electrochemical (PEC) etching is occurred only in n-type SiC because the PEC etching reaction requires hole carriers.

$$v = \frac{d}{t} = \frac{V}{St} \tag{4.8}$$

where S is the etching area. Since the current density J is given by I/S, the etching rate can be obtained as follow:

$$v = 9.7J \tag{4.9}$$

where v is in nm/min and J is in mA/cm^2. The etching rate of SiC represented by Eq. (4.5) can be obtained in the same manner, i.e.,

$$v = 19.4J. \tag{4.10}$$

PEC etching of SiC in this study was carried out with the setup shown in Fig. 4.4. A sample was fixed in the setup with silicone resin. The sample and platinum (Pt) counter electrode were soaked in etchant and connected to a sourcemeter (Keithley Instruments 2400). For the PEC etching, no bias was applied between the sample and the counter electrode, hence the sourcemeter was used as an ammeter. A xenon (Xe) lamp (Asahi Spectra MAX-301) was used for illuminating UV light to generate hole-electron pairs in the sample. The PEC etching was performed at elevated temperature around 70°C to enhance the chemical reaction of the dissolution of silicon oxide.

Fig. 4.5 shows the etching rate of the SiC with PEC etching as a function of the current density. Sample a is n-type 4H-SiC with doping concentration of 3×10^{16} cm^{-3} and sample b is n-type 6H-SiC with doping concentration of 2×10^{18} cm^{-3}. Solid lines are deduced etching rate of chemical reactions of Eqs. (4.4) and (4.5) from Faraday's laws of electrolysis. The etching rate of PEC etching of SiC agreed with deduced value from Eq. (4.4), suggesting that the oxidation reaction which occurred in the PEC etching of SiC can be represented by Eq. (4.4). As depicted in Fig. 4.5, the etching rate of sample a is larger than that of sample b. It is caused by the difference in the width of the space-charge region formed at the SiC/electrolyte interface. Sample a has a space-charge region of larger width because of the lower doping concentration, resulting in the larger amount of generated carriers with the same illumination. PEC etching of p-type SiC was also carried out, resulting in that p-type SiC was not etched.

4.3.3 Electrochemical Etching

EC etching of SiC without UV illumination is also able to decompose SiC. Applying bias voltage between the semiconductor and the counter electrode soaked in an electrolyte, carriers existed within the semiconductor are drifted to the electrolyte. As shown in Eqs. (4.4) and (4.5), hole carriers are required to electrochemically oxidize SiC. In p-type SiC, a lot of holes are existed as majority carriers while n-type SiC has much small amount

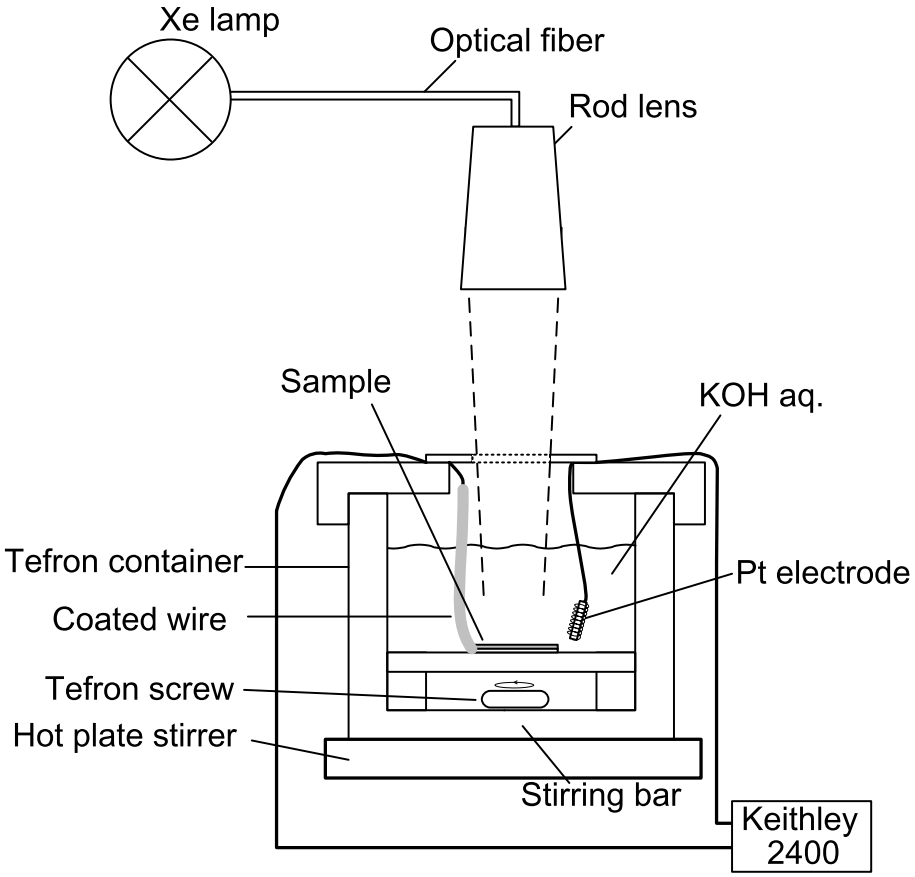

Figure 4.4: Schematic layout of experimental setup used for photoelectrochemical (PEC) and electrochemical (EC) etching. For EC etching, the xenon (Xe) lamp is not used.

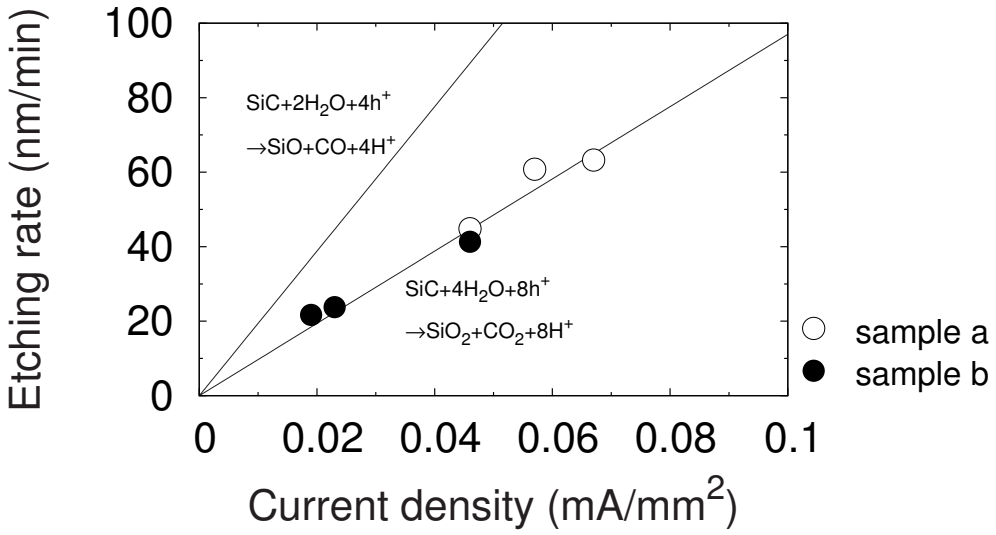

Figure 4.5: Etching rate of photoelectrochemical (PEC) etching as a function of current density. Sample a is n-type 4H-SiC with doping concentration of 3×10^{16} cm^{-3} and sample b is n-type 6H-SiC with doping concentration of 2×10^{18} cm^{-3}. Solid lines depict deduced etching rate from Faraday's laws of electrolysis with chemical reactions of Eqs. (4.4) and (4.5). The etching rate of PEC etching of SiC agreed with deduced value from Eq. (4.4).

of holes. As a result, EC etching of SiC has doping-type selectivity. In other words, this etching removes only p-type SiC.

EC etching of SiC in this study was carried out with the setup shown in Fig. 4.4 without UV illumination. For the EC etching, applying bias between the sample and the counter electrode was performed by the sourcemeter under constant-current conditions. Current direction was determined to utilize SiC as an anode. EC etching was performed at elevated temperature around 70°C to enhance the chemical reaction of the dissolution of silicon oxide.

The etching rate of EC etching of SiC is shown in Fig. 4.6 as a function of the current density. Sample A is p-type 4H-SiC with doping concentration of 2.0×10^{17} cm^{-3}, sample B is that with doping concentration of 6.8×10^{15} cm^{-3}, and sample C corresponds to p-type 4H-SiC substrates etched from the backside $(000\bar{1})$. Solid lines represent the deduced etching rate from Faraday's laws of electrolysis. As shown in Fig. 4.6, the etching rate of EC etching of SiC agreed with deduced value from Eq. (4.4). It suggests that the oxidation reaction which occurs in the EC etching of SiC can be represented by Eq. (4.4). EC etching of n-type SiC was also carried out, resulting in that n-type SiC was not etched.

The etching rate of EC etching can be enhanced easily by increasing the current density while enhancing that of PEC etching requires larger illumination intensity. On the other hand, EC etching of SiC only removes p-type SiC contrary to PEC etching, which removes only n-type SiC. It suggests that combining PEC and EC etching can improve the flexibility of the design of all-single-crystalline SiC MEMS because both n-type and p-type SiC can be used as a sacrificial layer.

4.4 Fabrication of Electrostatic-Actuated SiC Bridges Structures Using Photoelectrochemical Etching

In this section, I have fabricated all-single-crystalline SiC suspended bridge structures by using PEC etching. Electrostatic actuation of the bridges has been also demonstrated.

4.4.1 Device Structure

Fig. 4.7 shows a schematic illustration of the suspended SiC bridge structure. A thin SiC bridge is suspended on a SiC substrate. The bridge is actuated by applying a voltage between the bridge and the substrate. To actuate with a moderate voltage, the gap size between the bridge and the substrate should be submicron as described in Section 4.2.1. A 700-nm gap was employed for the bridge fabrication. The thickness of the bridge was determined to be 100 nm as derived from Section 4.2.1. The width and the length of a bridge are commonly 1-10 μm and 100-1000 μm, respectively. In this study, the width of 4 or 10 μm and the length of 50-200 μm were employed for the dimensions of the fabricated

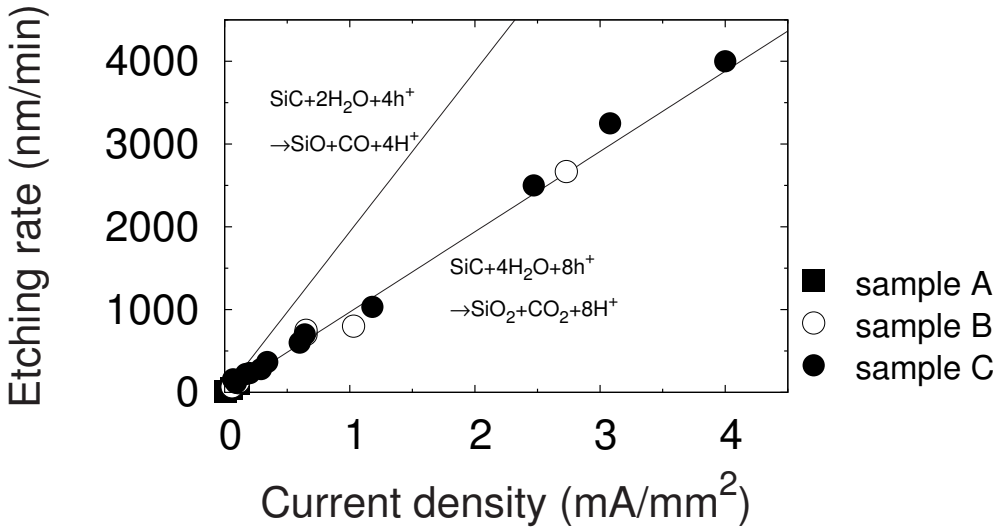

Figure 4.6: Etching rate of electrochemical (EC) etching as a function of current density. Sample A is p-type 4H-SiC with doping concentration of 2.0×10^{17} cm^{-3}, sample B is that with doping concentration of 6.8×10^{15} cm^{-3}, and sample C is p-type 4H-SiC etched from the backside $(000\bar{1})$. Solid lines depict deduced etching rate from Faraday's laws of electrolysis with chemical reactions of Eqs. (4.4) and (4.5). The etching rate of EC etching of SiC agreed with deduced value from Eq. (4.4).

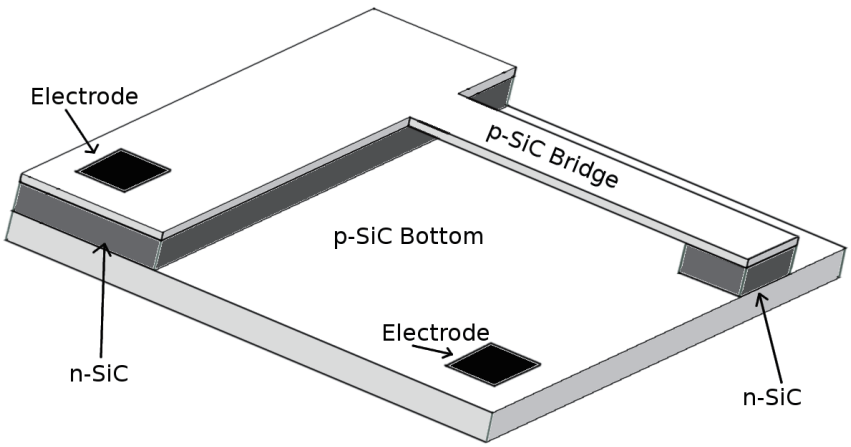

Figure 4.7: Schematic drawing of a single-crystalline SiC bridge (double-clamped beam) structure. Electrostatic actuation can be realized by applying bias voltage between the bridge and the bottom.

bridge structure.

Instead of conventional sacrificial-layer etching, doping-type selective PEC etching was employed. An n-type SiC was utilized as a sacrificial layer of surface micromachining in PEC etching. It is noted that a reverse connected pn junction in a p–n–p structure provides the electrical isolation. A p–n–p structure can block both positive and negative voltages. SiC pn junctions can easily block over 30 V because of the large breakdown field (around 3 MV/cm) of a high-quality homoepitaxial 4H-SiC layer [20].

4.4.2 Device Fabrication

Fig. 4.8 shows the fabrication process of the SiC bridge structures. Commercially available p-type 4H-SiC (0001) 8° off-axis substrates with a 12-μm-thick aluminum (Al)-doped p-type homoepitaxial layer were prepared. This epilayer was grown by chemical vapor deposition (CVD) with a doping concentration of 6×10^{15} cm^{-3}. Then multiple nitrogen ion (N^+) implantation (100-650 keV) was carried out to form a buried n-type layer with a depth of 100 to 800 nm. Subsequently, multiple aluminum ion (Al^+) implantation (20 and 50 keV) was carried out to assure p-type conductivity for a 100-nm-thick surface layer. The box profile of the ion implantation is shown in Fig. 4.9. After ion implantations, thermal annealing was conducted to activate implanted dopants at 1700°C for 30 min in argon (Ar) atmosphere. Finally, p–n–p structure was successfully formed as shown in Fig. 4.8(a).

After forming the p–n–p structure, RIE with CF_4 and O_2 gases was carried out to form a line and space pattern with a depth of about 500 nm [Fig. 4.8(b)]. This pattern was also used as a window to access the buried n-type layer. Next, contacts were formed by nickel (Ni) metal deposition and then thermal treatment was performed to obtain ohmic contacts at 950°C for 10 min in Ar atmosphere [Fig. 4.8(c)].

Then PEC etching was carried out to obtain suspended bridges at 70°C in a 0.1 wt. % KOH solution [Fig. 4.8(d)]. A 300 W xenon lamp was used for PEC etching and the irradiation power density was 440 mW/cm^2. The PEC etching caused lateral (undercut) etching to remove an n-type layer under a surface p-type layer. As a result, a surface p-type layer became to a suspended layer as schematically illustrated in Fig. 4.8(e).

A bird's-eye-view scanning electron microscope (SEM) image of the sidewall of the bridge after PEC etching is shown in Fig. 4.10. The top and bottom p-type layers were not etched and remained as structural layers. The buried n-type layer was etched; however, it remained as a porous layer. As a result, the top p-type layer was not released and not suspended.

A porous layer formed by PEC etching can be removed by thermal oxidation. The surface area of the porous layer is much larger than that of a bulk layer, suggesting that the oxidization rate of a porous layer was much faster and a porous layer can be entirely oxidized with keeping a top layer. 1150°C 1 h thermal oxidization was therefore carried out after PEC etching, following which generated SiO_2 was removed by an HF solution. Fig. 4.11 shows a bird's-eye-view SEM image of the sidewall of the bridge after thermal oxidization

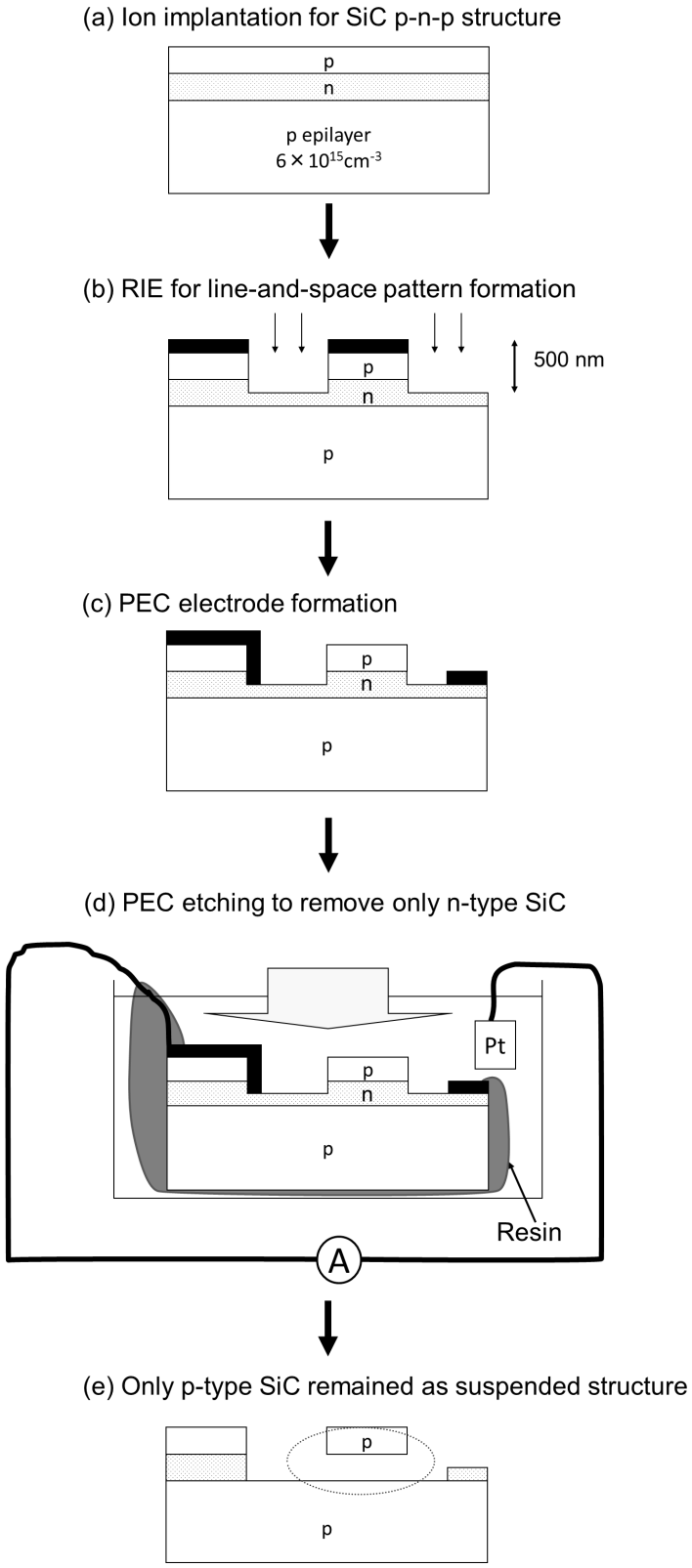

Figure 4.8: Fabrication process of electrostatic-actuating all-single-crystalline SiC bridge structures.

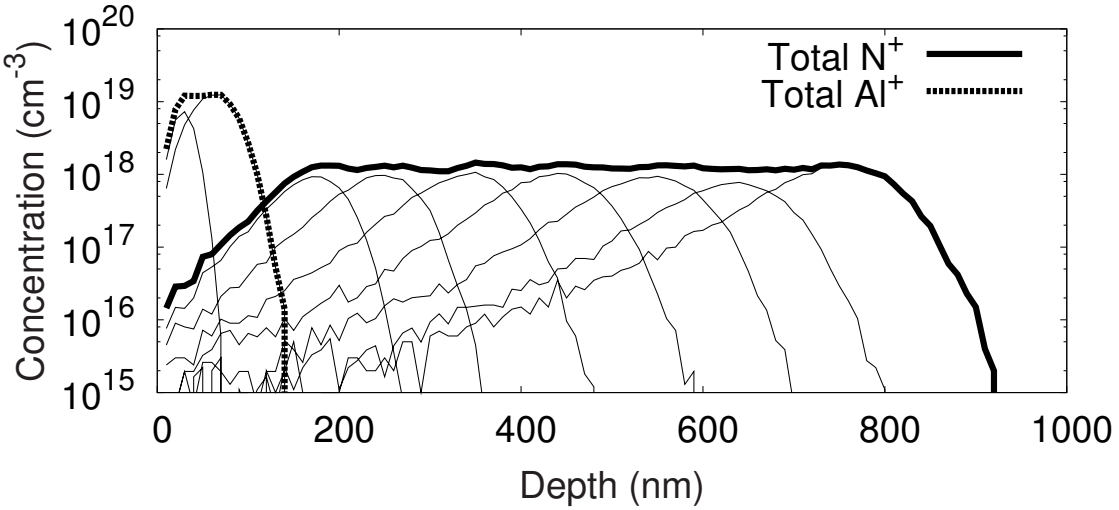

Figure 4.9: Box profile of ion implantation utilized for the fabrication of all-single-crystalline SiC bridge structures. Nitrogen ions (N^+) are used to form n-type SiC from the depth of 100 nm to 800 nm and aluminum ions (Al^+) are used to form p-type SiC between the surface and the depth of 100 nm.

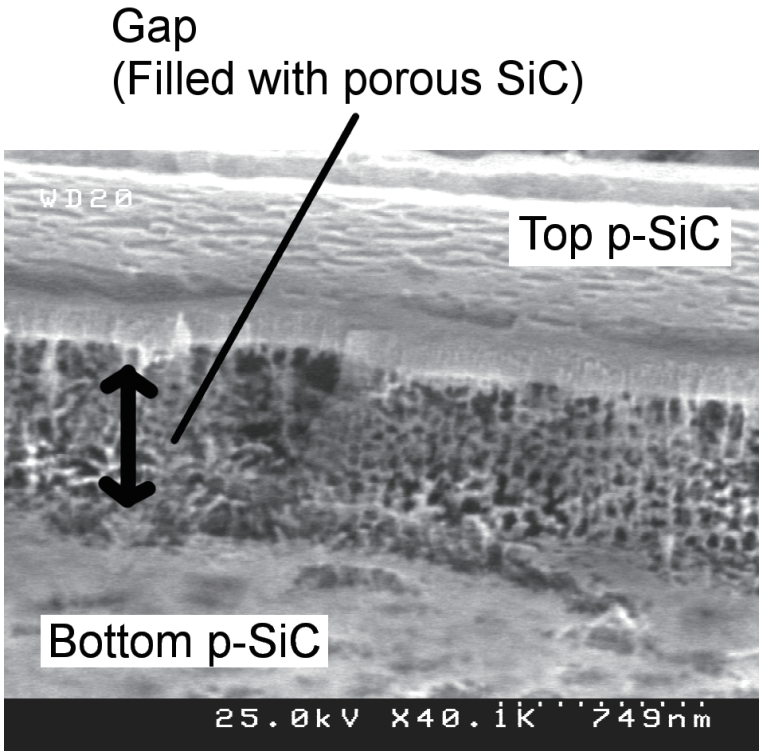

Figure 4.10: Bird's-eye-view scanning electron microscope (SEM) image of the sidewall of the bridge after photoelectrochemical etching. Top and bottom p-type layers were not etched and remained as structural layers. A buried n-type layer remained as a porous layer while it was expected to be removed as a sacrificial layer.

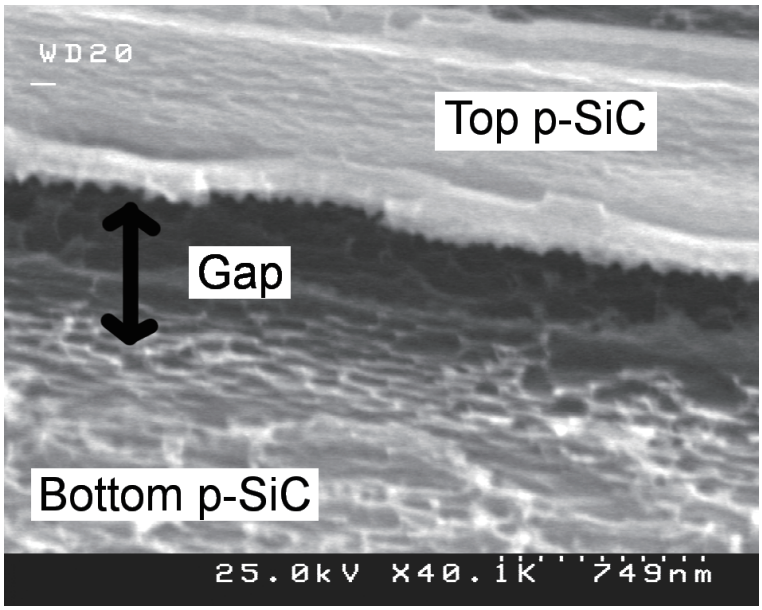

Figure 4.11: Bird's-eye-view scanning electron microscope (SEM) image of the sidewall of the bridge after photoelectrochemical etching followed by oxidization (1150°C, 1 h) and subsequent HF release. The porous n-type layer was successfully removed.

followed by SiO_2 removal. The porous n-type layer was removed and the top p-type layer was released from the bottom p-type layer. Fig. 4.12 shows a SEM image of a fabricated 4-μm-wide bridge array. Suspended p-type SiC bridges were successfully fabricated.

4.4.3 Electrostatic Actuation of Fabricated Devices

To applying bias voltage between the bridge and the bottom, ohmic contact electrodes were formed. Titanium (Ti), aluminum (Al), and Ni were deposited in this sequence on both bridge and bottom layers. Increasing the applied voltage between the fabricated bridges and the bottom, electrostatic actuations of the bridges were observed at 10-20 V under an optical microscope. Fig. 4.13 shows the current-voltage characteristics of the fabricated SiC bridge structure with electrostatic actuation. The leakage current with applying voltage at 20 V was 251 μA, which was slightly leaked, as shown in Fig. 4.13. This small leakage was probably caused by leaky spots under top electrodes. On the other hand, applying negative voltage, the leakage current sharply increased below -13 V and was 3.5 mA at -20 V. This large leakage was caused by the breakdown of the top p-type SiC and buried n-type SiC junction. The high doping concentrations of both layers caused the low breakdown voltage of this pn junction.

4.4.4 Discussion

Porous layer formation was occurred just under the top p-type layer, suggesting that the formation was caused by the reduction of the current density of PEC etching in the n-type SiC. Light absorption of the top p-type layer resulted in this reduction. In case of Si, Smith and Collins reported porous Si formation mechanisms by anodic oxidation [21] and this report describes that low current density of anodic oxidation causes the formation of porous Si.

FEM structural analysis of electrostatic bridge actuation was carried out on the same design of the fabricated bridges (width: 4 μm, length: 100 μm, thickness: 100 nm, gap between the bridge and the bottom: 700 nm) by using CoventorWare 2008 software. In this simulation, the material properties of SiC were employed as follows: the density of SiC was 3.22 g/cm^3 and the Young's modulus was 448 GPa [10]. The result of the simulation is that bridges can be sufficiently deformed at 2 V, which is much smaller than the actuating voltage of the fabricated bridges. The difference is probably caused by the residuals of the n-type SiC layer. As illustrated in Fig. 4.14, if there is residual of n-type SiC under a bridge, the length of the deformable bridge is shortened. Shorter bridge length causes the bridge to be less deformable, in other words, it causes the increase of the applied voltage for electrostatic actuation. The wide variety of actuating voltage also suggests that residual n-type SiC exists randomly underneath the p-type SiC bridges.

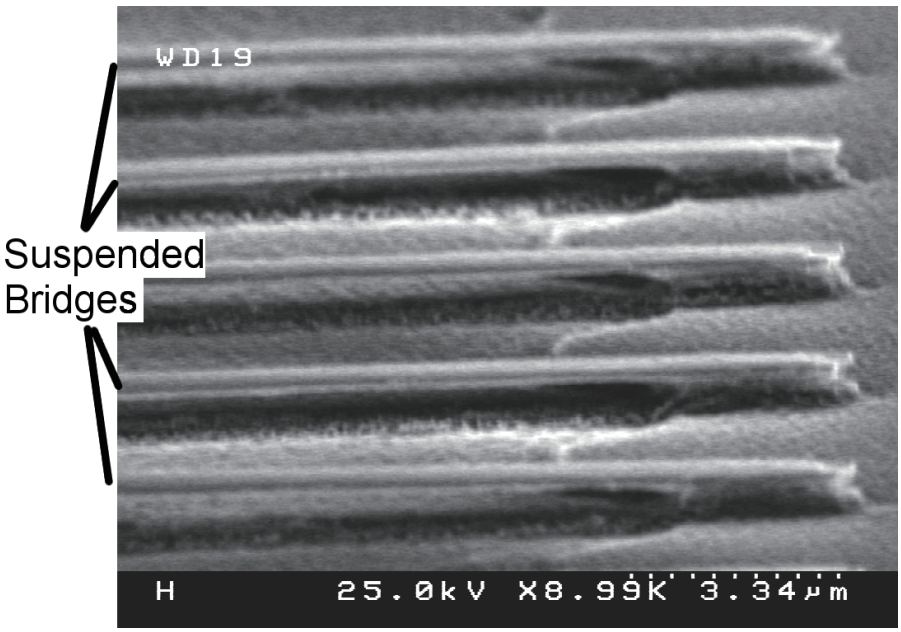

Figure 4.12: Bird's-eye-view scanning electron microscope (SEM) image of the fabricated single-crystalline SiC bridge structure.

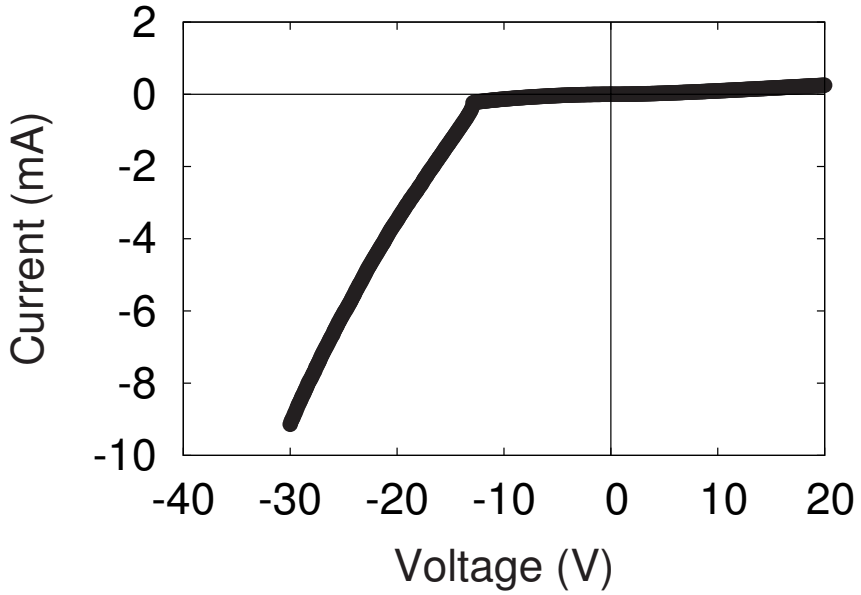

Figure 4.13: Current-voltage characteristics of the fabricated SiC bridge structure applying the voltage with electrostatic actuation. The leakage current under positive-bias condition is very small while it sharply increases below -13 V.

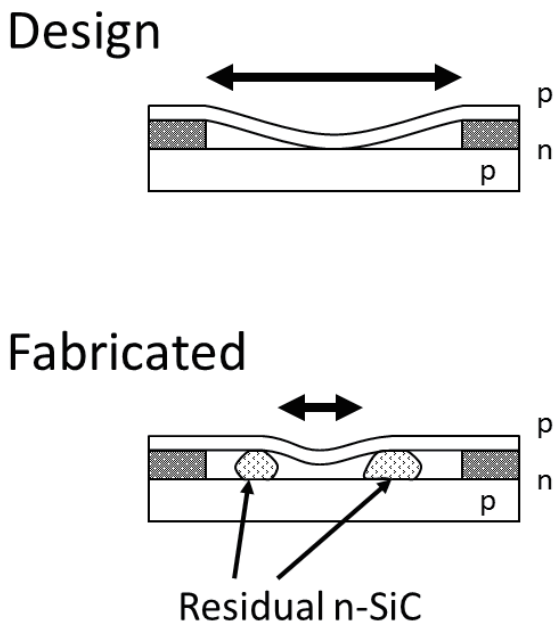

Figure 4.14: Schematic drawing of the deformable length of the bridge as designed and fabricated. The length of the deformable bridge becomes shorter than that as designed because of residual n-type SiC.

4.5 Fabrication of High-Quality-Factor SiC Cantilever Structures Using Electrochemical Etching

Although all-single-crystalline SiC bridge structure was successfully fabricated as described in the previous section, sacrificial n-type SiC layer was not fully removed because the illumination of PEC was weakened by the photoabsorption at the top p-type layer. To avoid this effect and to fabricate suspended structure properly, I employed EC etching of SiC without illumination and fabricated suspended cantilever structure entirely composed of single-crystalline SiC.

4.5.1 Device Structure

Fig. 4.15 shows a schematic illustration of single-crystalline SiC cantilever structure. A thin SiC cantilever is suspended on a SiC substrate. The width and the length of the cantilever are 15 μm and 80-140 μm, respectively. The thickness of the cantilever is 900 nm. The gap between the cantilever and the substrate is larger than 10 μm to evaluate resonance characteristics with optical method. A p-type SiC is utilized as a sacrificial layer in EC etching of SiC. By applying a positive voltage to the SiC in an electrolyte, holes are supplied only at the interface between the p-type SiC and the solution, so that only p-type SiC is oxidized and etched.

4.5.2 Device Fabrication

Fig. 4.16 shows the fabrication process of single-crystalline 4H-SiC cantilevers. As shown in Fig. 4.16(a), a 1-μm-thick n-type layer was grown on a p-type 4H-SiC (0001) 8° off-axis substrate by CVD. The doping concentration of the n-type SiC layer was 4.5×10^{18} cm^{-3}. Following n–p stack formation, the n-type SiC was etched by RIE using CF_4 and O_2 gases. RIE was performed until the p-type SiC was exposed to the surface [Fig. 4.8(b)]. After the cantilever patterning, metal deposition (Ti/Al/Ni) to the backside of the substrate was carried out, following which thermal treatment was performed to obtain ohmic contacts at 1000°C for 2 min in Ar atmosphere [Fig. 4.16(c)].

Then EC etching was carried out to obtain suspended cantilevers at 80°C in a 5.4 wt. % KOH solution by applying a constant current to the p-type SiC for 12 min [Fig. 4.16(d)]. The current density at the interface between the SiC and the KOH solution was 3.3 mA/mm^2. Under these conditions, the side-etching width of the substrate was about 35 μm and the etched depth was about 18 μm. As a result, the surface n-type SiC layer became a suspended layer as shown in Fig. 4.16(e).

The p-type sacrificial layer was selectively etched by EC etching. However, the p-type SiC just under the n-type SiC cantilevers was not completely etched and was formed to

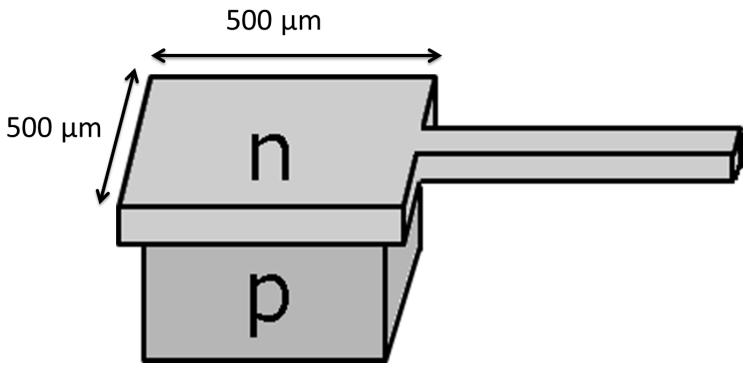

Figure 4.15: Schematic drawing of a single-crystalline SiC cantilever (single-clamped beam) structure. The width and the length of a bridge are 15 μm and 80-140 μm, respectively.

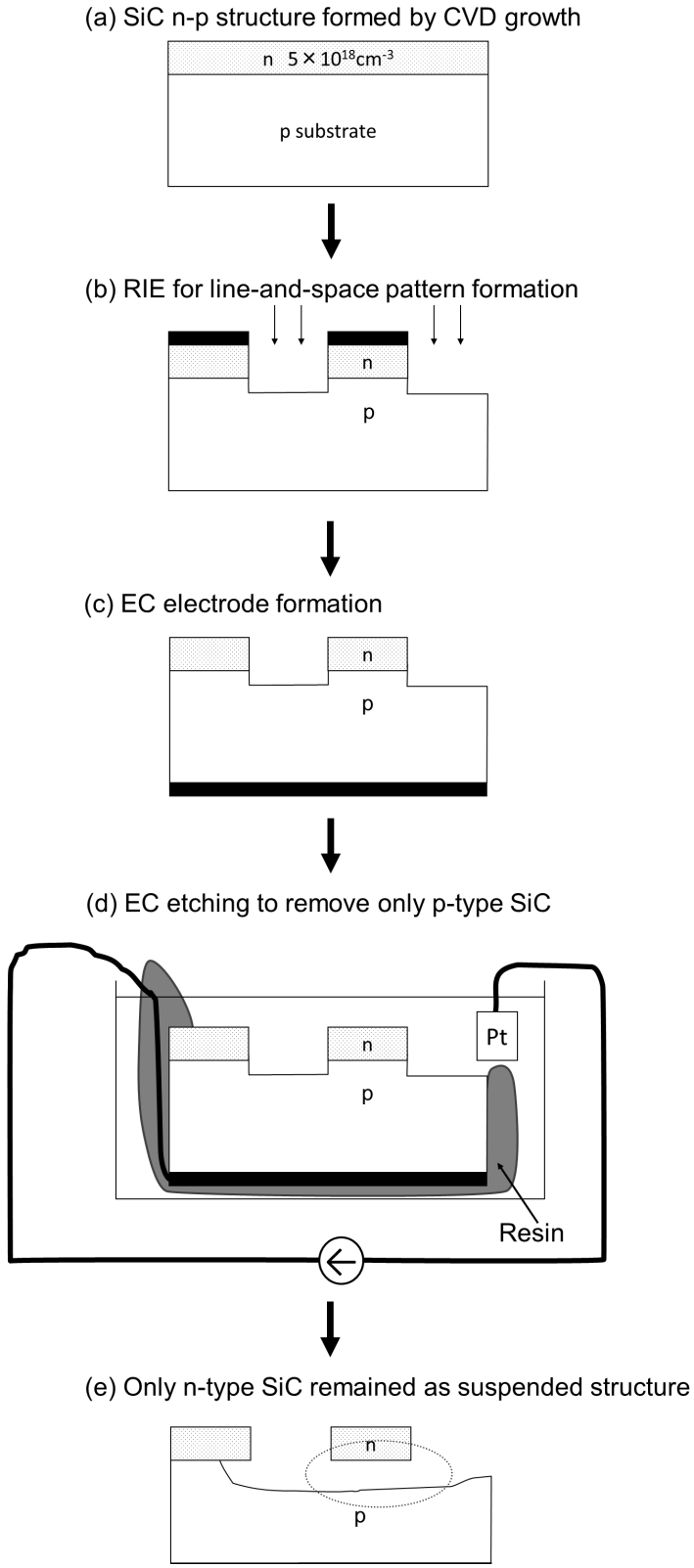

Figure 4.16: Fabrication process of all-single-crystalline SiC cantilever structures.

porous SiC. To remove the porous SiC layer, thermal oxidation was performed for 2.5 h at 1150°C followed by SiO_2 removal using an HF solution. As a result, the porous SiC was completely removed. It is noted that the thickness of the SiC cantilevers was decreased from 1 μm to about 900 nm after the thermal oxidation and SiO_2 removal, suggesting that the cantilever layer was also slightly oxidized. A bird's-eye-view SEM image of the fabricated all-single-crystalline SiC cantilever is shown in Fig. 4.17.

4.5.3 Resonance Characteristics

The resonance characteristics of the fabricated cantilevers were measured by illuminating a laser light onto the center of the free-standing part of the cantilevers and detecting the reflected light with a laser Doppler vibrometer (DENSHIGIKEN Vibroducer V1002). To excite a vibration in fabricated cantilevers, the samples were mounted on a piezoceramic (lead zirconium titanate, PZT) actuator. Applying a sinusoidal voltage to the PZT actuator, the cantilevers were vibrated. The frequency range is below 1.5 MHz, which is limited by the actuation of PZT. The cantilevers were placed in a vacuum chamber with a small window, which allowed optical access to the sample. The pressure in the chamber was 1.5 mTorr.

The resonant frequency and the quality factor of the cantilevers were not varied by changing the amplitude of the sinusoidal voltage between 0.2 and 20 mV_{RMS}. It suggests that the resonance characteristics responded linearly to the amplitude of the applied voltage in this region. For the following measurement, the amplitude of the sinusoidal voltage was employed as 1 mV_{RMS}.

Fig. 4.18 shows the first-mode resonant spectrum of the 100-μm-length 4H-SiC cantilever. The full-width at half-maximum (FWHM) of this 4H-SiC cantilever was 0.64 Hz. The quality (Q) factor was calculated as $Q = f/\Delta f$, where f is the resonant frequency and Δf is the FWHM. Q-factor of the fabricated SiC cantilever was 230,000. Resonance characteristics of fabricated SiC cantilevers with different dimensions were also measured, and Q-factors of around 200,000 were obtained in all SiC cantilevers. Enderling and colleagues reported the resonance characteristics of 3C-SiC cantilevers fabricated on a Si substrate and Q-factor of the 3C-SiC cantilevers with the similar dimensions in vacuum condition was determined to be 14,755 [22]. Q-factor of the fabricated all-single-crystalline 4H-SiC cantilevers was more than 10 times larger than that of reported 3C-SiC cantilevers fabricated on a Si substrate. It is noted that the Q-factors of fabricated all-single-crystalline SiC cantilevers are much larger than the reported value of single crystalline Si cantilever with similar dimensions ($\sim$5,000) [23].

Fig. 4.19 shows the resonant frequencies of 4H-SiC cantilevers of various lengths. The first- and second-mode resonant frequencies are shown with filled circle and square symbols, respectively. Numerical simulations of the resonance characteristics of these cantilevers were also carried out using the FEM. In this simulation, the material properties of SiC were employed as follows: the density of SiC was 3.22 g/cm^3 and the Young's modulus was

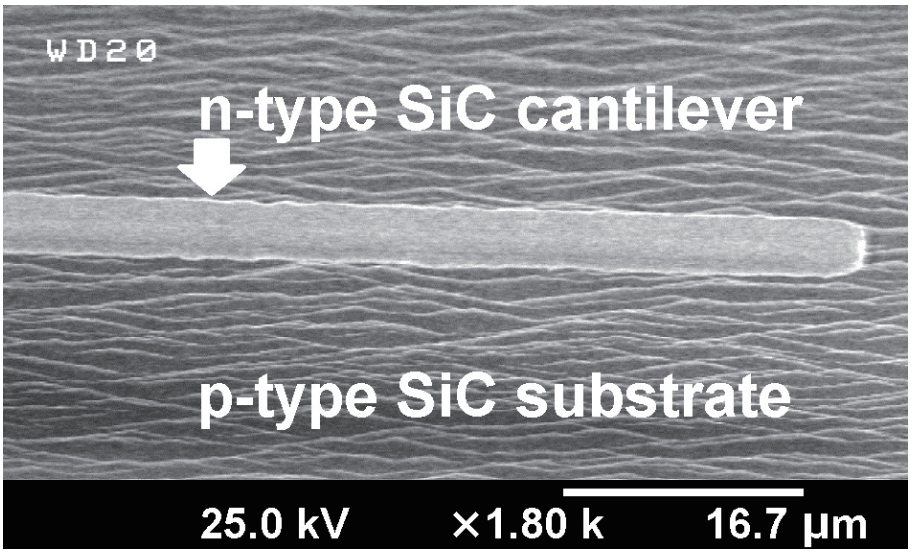

Figure 4.17: Bird's-eye-view scanning electron microscope (SEM) image of the fabricated single-crystalline SiC cantilever structure.

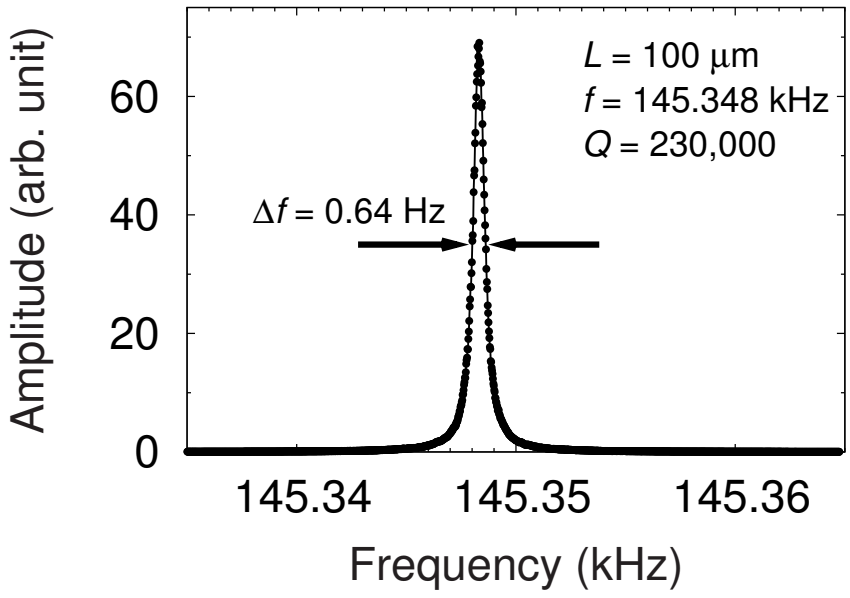

Figure 4.18: Resonance characteristics of the fabricated SiC cantilever. L and f are the length and resonant frequency of the cantilever, respectively. High quality factor $Q = 230,000$ was obtained with the all-single-crystalline SiC cantilever.

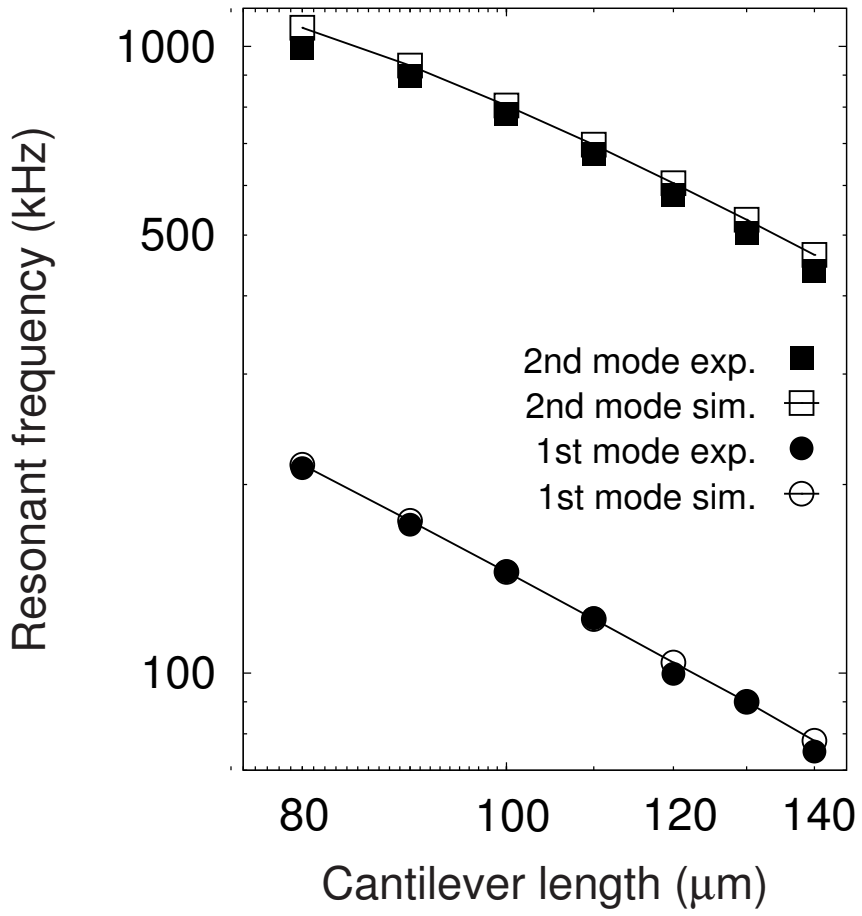

Figure 4.19: Resonant frequencies of fabricated SiC cantilevers with various lengths. First- and second-mode resonances are measured and plotted with filled symbols. Resonant frequencies of fabricated SiC cantilever structures derived from FEM analysis are also plotted with open symbols.

448 GPa [10]. The simulation results are shown in Fig. 4.19 with open symbols. Both first- and second-mode experimental resonant frequencies fairly agreed with the simulation results. The differences between experimental resonant frequencies and the simulation results are only 2.76 % in average.

4.5.4 Discussion

Significantly large Q-factor was obtained from the fabricated cantilevers constituted entirely 4H-SiC. This shows that the energy dissipation of 4H-SiC cantilevers is much smaller than that of conventional 3C-SiC cantilevers. The energy dissipation characteristics in vibrational microactuators are categorized as internal friction, support loss, and air damping as discussed by Hosaka [24]. In case of the internal friction, defects in crystals of constituent materials are one of the sources of internal friction and the defects can lead to energy dissipation. In 3C-SiC cantilevers, 3C-SiC films have a large number of defects such as stacking faults and dislocations because they are heteroepitaxially grown on a Si substrate with a large lattice mismatch (20 %). On the other hand, 4H-SiC cantilevers are fabricated on a 4H-SiC substrate. Homoepitaxially-grown 4H-SiC films have significantly lower amount of defects than 3C-SiC films, resulting in the much lower internal friction in 4H-SiC cantilevers.

As for the support loss, this loss is generated from the friction between connected surfaces. Since 3C-SiC cantilevers are fabricated on a Si substrate, which is a different material from the cantilevers, the support loss cannot be neglected in 3C-SiC cantilevers. In case of 4H-SiC cantilevers, the devices entirely consist of 4H-SiC, leading to the significantly small support loss in the cantilevers. Furthermore, Q-factor of the fabricated 4H-SiC cantilevers is independent of cantilever length, suggesting that 4H-SiC cantilevers are not influenced by the support loss.

It has been reported that air damping under 1 mTorr vacuum condition is negligible in resonators with a Q-factor of less than 10,000 [23]. It suggests that air damping may not be negligible for the fabricated SiC cantilevers because of the high Q-factor of 200,000. To completely eliminate the air damping effect, measuring the resonance characteristics under much higher vacuum conditions should be necessary.

4.6 Summary

In this chapter, suspended bridge and cantilever structure of all-single-crystalline 4H-SiC were fabricated. From the numerical simulation of the FEM analysis, SiC bridge structure with sub-micron air gap between the bridges and the bottom is required to electrostatically actuate the bridges with a moderate operating voltage. To fabricate such suspended structure, it can be useful to employ the combination of patterning of devices with RIE and sacrificing an n-type or p-type SiC layer with PEC or EC etching. PEC and EC etching of SiC showed selectivity in doping type, where n-type SiC is removed by PEC and p-type

SiC by EC.

A suspended bridge structure of all-single-crystalline SiC was fabricated utilizing PEC etching. Although a sacrificial n-type SiC layer was not removed by PEC etching and remained as porous SiC, the porous SiC layer was removed by utilizing thermal oxidation followed by SiO_2 removal by an HF solution, resulting in the successful fabrication of the bridge structure entirely composed of 4H-SiC. Electrostatic actuation of the fabricated bridges was also demonstrated.

I also fabricated single-crystalline 4H-SiC cantilevers on a 4H-SiC substrate by EC etching without UV illumination. The cantilever structure was successfully fabricated. The maximum Q-factor of the 4H-SiC cantilevers was 230,000, which was more than 10 times higher than that of conventional 3C-SiC cantilevers fabricated on a Si substrate.

Although the fabrication process of 4H-SiC MEMS is more difficult than that of 3C-SiC/Si MEMS, their very high Q-factor makes 4H-SiC MEMS very attractive for high-sensitivity sensors. Furthermore, all-single-crystalline SiC MEMS devices can be combined with SiC high temperature electronic devices. This combination can realize integrated sensor systems operating in harsh environments. In the future, the improvement of etching condition and the device design for the PEC and EC etching should lead to the realization of complex micromechanical structures entirely composed of single-crystalline SiC and of the integration of SiC MEMS and semiconductor devices.

References

[1] W. Lang, Mater. Sci. Eng. R **17**, 1 (1996).

[2] M. Mehregany and C. A. Zorman, Thin Solid Films **355**, 518 (1999).

[3] R. M. Sarro, Sens. Actuators A **82**, 210 (2000).

[4] M. Mehregany, C. A. Zorman, S. Roy, A. J. Fleischman, C. H. Wu, and N. Rajan, Int. Mater. Rev. **45**, 85 (2000).

[5] A. Klumpp, U. Schaber, H. L. Offereins, K. Kühl, and H. Sandmaier, Sens. Actuators A **41**, 310 (1994).

[6] S. Roy, R. G. DeAnna, C. A. Zorman, and M. Mehregany, IEEE Trans. Electron Devices **49**, 2323 (2002).

[7] D. Gao, M. B. J. Wijesundara, C. Carraro, R. T. Howe, and R. Maboudian, IEEE Sens. J. **4**, 441 (2004).

[8] C. Förster, V. Cimalla, K. Brückner, M. Hein, J. Pezoldt, and O. Ambacher, Mater. Sci. Eng. C **25**, 804 (2005).

[9] R. S. Okojie, A. A. Ned, and A. D. Kurtz, Sens. Actuators A **66**, 200 (1998).

[10] M. Mehregany, C. A. Zorman, N. Rajan, and C. H. Wu, Proc. IEEE **86**, 1594 (1998).

[11] J. S. Shor, R. M. Osgood, and A. D. Kurtz, Appl. Phys. Lett. **60**, 1001 (1992).

[12] J. S. Shor, A. D. Kurtz, I. Grimberg, B. Z. Weiss, and R. M. Osgood, J. Appl. Phys. **81**, 1546 (1997).

[13] M. Kato, M. Ichimura, E. Arai, and P. Ramasamy, Jpn. J. Appl. Phys. **42**, 4233 (2003).

[14] W. -H. Chang, Sens. Actuators A **112**, 36 (2004).

[15] Y. Ke, F. Yan, R. P. Devaty, and W. J. Choyke, J. Appl. Phys. **106**, 064901 (2009).

[16] J. W. Palmour, B. E. Williams, P. Astell-Burt, and R. F. Davis, J. Electrochem. Soc. **136**, 491 (1989).

[17] J. W. Palmour, R. F. Davis, T. M. Wallett, and K. B. Bhasin, J. Vac. Sci. Technol. A **4**, 590 (1985).

[18] K. M. Robb, J. Hopkins, G. Nicholls, and L. Lea, Solid State Technol. **48**, 61 (2005).

[19] T. Kimoto, N. Miyamoto, and H. Matsunami, IEEE Trans. Electron Devices **46**, 471 (1999).

[20] A. O. Konstantinov, Q. Wahab, N. Nordell, and U. Lindefelt, Appl. Phys. Lett. **71**, 90 (1997).

[21] R. L. Smith and S. D. Collins, J. Appl. Phys. **71**, R1 (1992).

[22] S. Enderling, J. Hedley, L. Jiang, R. Cheung, C. Zorman, M. Mehregany, and A. J. Walton, J. Micromech. Microeng. **17**, 213 (2007).

[23] K. Y. Yasumura, T. D. Stowe, E. M. Chow, T. Pfafman, T. W. Kenny, B. C. Stipe, and D. Rugar, J. Microelectromech. S. **9**, 117 (2000).

[24] H. Hosaka, K. Itao, and S. Kuroda, Proc. IEEE Workshop on MEMS 1994, pp. 193 (1994).

Chapter 5

High-Temperature Operation of SiC pn Photodiodes

5.1 Introduction

High-temperature smart sensors are needed in various fields such as automotive engines, power instrumentation, and space exploration. One of the most promising materials for integrated sensor systems of microelectromechanical systems (MEMS) and electronic devices for high-temperature applications is silicon carbide (SiC). SiC is an attractive structural material for applications of MEMS which operates at high temperature because of its superior material properties [1–5]. To realize integrated MEMS systems, electronic devices such as transistors, diodes, and discrete sensors, which can operate at high temperature, are required. The large bandgap of SiC should lead to high-temperature operation in SiC electronic devices at more than 500°C [6, 7].

SiC electronic devices operated in high-temperature environments have been investigated, such as field-effect transistors [8–10], diodes [11], and gas sensors [12]. In this study, I focused on a SiC pn photodiode, which can be used for an ultraviolet (UV) photodetector operating in a wide range of temperature [room temperature (RT) to 500°C]. High-temperature UV photodetectors can be used as flame detectors for combustion control within automotive engines. So far, several groups have reported 6H-SiC pn photodiodes [13–16], and Edmond and coworkers reported high quantum efficiency (around 70-85 % at 270 nm illumination) of 6H-SiC pn photodiodes up to 350°C [15, 16].

However, there have been no detailed studies on the temperature dependence of the photoresponse of SiC pn photodiodes. One of the requirements for high-temperature sensors operating in such a wide range of temperature is small temperature dependence of the photoresponse. For example, sensors with temperature-independent response are desirable in environments where the temperature changes sharply. To reduce the temperature dependence of the photoresponse, it is necessary to understand the origin of the dependence in pn photodiodes. Another issue is that the reports did not utilize the full potential of SiC.

As mentioned above, SiC photodiodes should work at more than 500°C. Although Cambell and Chang reported photovoltaic operation of a 6H-SiC photodiode at 800 K (527°C) [13], the output voltage of the photodiode at 800 K was significantly low and the report involves no detailed study about high-temperature operation. To operate SiC pn photodiodes properly at high temperature, it is necessary to understand the high-temperature electronics of SiC pn junction. In other words, electrical characteristics of SiC pn junction at high temperature should be revealed.

In this chapter, I have fabricated 4H-SiC pn photodiodes and investigated the electrical characteristics of the devices from RT to elevated temperature in detail. The temperature dependence of the photoresponse was measured between RT and 300°C for various wavelengths (280-365 nm) as a function of reverse-bias voltage. I have demonstrated that the device shows small temperature dependence at certain wavelength illumination, and I have proposed that the targeted wavelength can be adjusted on the same device by controlling the reverse-bias voltage. Furthermore, the electrical characteristics of fabricated pn photodiodes up to 600°C have been investigated to operate the devices properly at such high temperature. Employing new device passivation technique, the reverse leakage current has been significantly reduced at elevated temperatures and I have measured the photoresponse of the fabricated device for various wavelengths up to 500°C.

5.2 Temperature-Independent Photoresponse in SiC pn Photodiodes

5.2.1 Device Fabrication Process

Fig. 5.1 shows a schematic structure of a fabricated SiC pn photodiode. Single-crystalline n-type 4H-SiC (0001) 8° off-axis substrates were used in this study. A nitrogen (N)-doped n-type epitaxial layer of 10 μm thickness was grown on the substrate. A heavily aluminum (Al)-doped p-type epitaxial layer of 470 nm thickness was subsequently grown to form p^+–n junction. The doping concentrations of n-type and p-type epitaxial layers were 5×10^{15} and 1×10^{18} cm^{-3}, respectively. Mesa structure was fabricated by using reactive ion etching (RIE) with tetrafluoromethane (CF_4) and oxygen (O_2) gases [17]. The depth of fabricated mesa structure was 1 μm. The etching mask of this RIE process was silicon dioxide (SiO_2) formed by plasma-enhanced chemical vapor deposition. Diodes with different mesa dimensions from 0.3×0.3 to 2×2 mm^2 were fabricated. The surface was passivated with a 30-nm-thick oxide formed by dry thermal oxidation at 1150°C for 3 h. The contact to the top p-type epitaxial layer was formed by depositing titanium (Ti), Al, and nickel (Ni) in this sequence, following which the contact to the n-type SiC substrate was formed with Ni. The top contact consisted of a simple frame along the edge of the mesa. Thermal treatment was performed at 1000°C for 2 min in argon (Ar) atmosphere to obtain ohmic

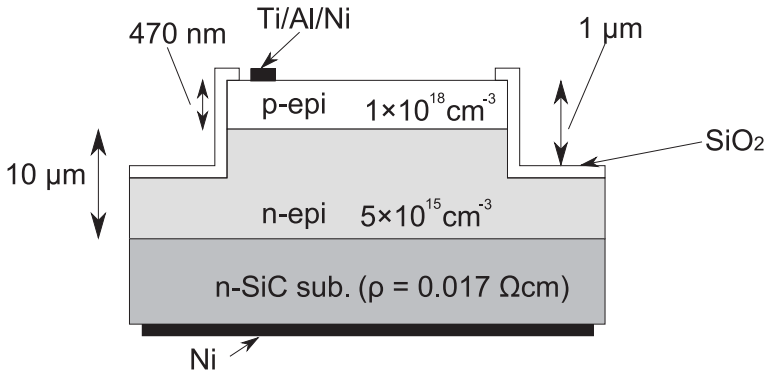

Figure 5.1: Schematic structure of a fabricated 4H-SiC pn photodiode. The doping concentration of the n-type epitaxial layer was 5×10^{15} cm^{-3} and that of the p-type epitaxial layer was 1×10^{18} cm^{-3}.

contacts.

5.2.2 Measurement Setup

The electrical characteristics of the fabricated devices were measured as a function of temperature. The temperature was changed from 24 to 300°C. The measurements were performed under dark and UV illuminated conditions. Optical responsivity measurements were carried out using a 300 W xenon lamp (Asahi Spectra MAX-301) with band pass filters (Asahi Spectra LX series) to illuminate UV light of specific wavelength. The wavelength was changed from 280 to 365 nm. The full width at half maximum of band pass filters was 10 nm.

5.2.3 Temperature Dependence of Photoresponse

Under the dark condition, the current-voltage (I–V) characteristics of 0.5×0.5 mm^2 SiC pn photodiode is shown in Fig. 5.2. The I–V characteristics of the SiC pn photodiode yield ideality factors of 1.85-1.95 from 24 to 300°C. The leakage current under the −150-V-bias condition was 65 pA at 24°C and 5.3 nA at 300°C. The leakage current was much smaller than the generated photocurrent (0.3-5.3 μA) in this study. Fig. 5.3 depicts the I–V characteristics of 0.5×0.5 mm^2 SiC pn photodiode at 300°C under dark and 300 nm UV illumination.

The photoresponse and external quantum efficiency (EQE) of a fabricated device as determined by measuring the short-circuit current are shown in Fig. 5.4. The photoresponse was obtained in amperes per watt from the measured photocurrent of the device and the intensity of the illumination. The external quantum efficiency is determined by the following simple equation:

$$\mathrm{EQE} = 1240 \times \frac{R}{\lambda} \tag{5.1}$$

where R is the responsivity (in A/W) and λ is the wavelength of the incident light (in nm). The external quantum efficiency over 40 % was obtained for wavelengths of 280-310 nm. The photoresponse increased with increasing temperature. On the other hand, the temperature dependence became smaller for shorter wavelength, and the photoresponse was nearly temperature independent at 280 nm.

5.2.4 Temperature-Independent Photoresponse by Applying Reverse-Bias Voltage

Fig. 5.5 shows the photoresponse of a fabricated device under (a) 50- and (b) 150-V-reverse-biased conditions. With increasing reverse-bias voltage, the wavelength of the temperature-independent photoresponse was significantly changed. The tunable wavelength range was

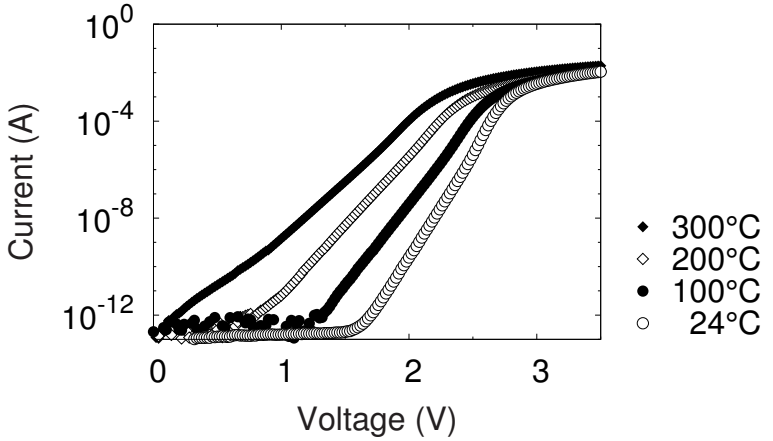

(a) Forward bias

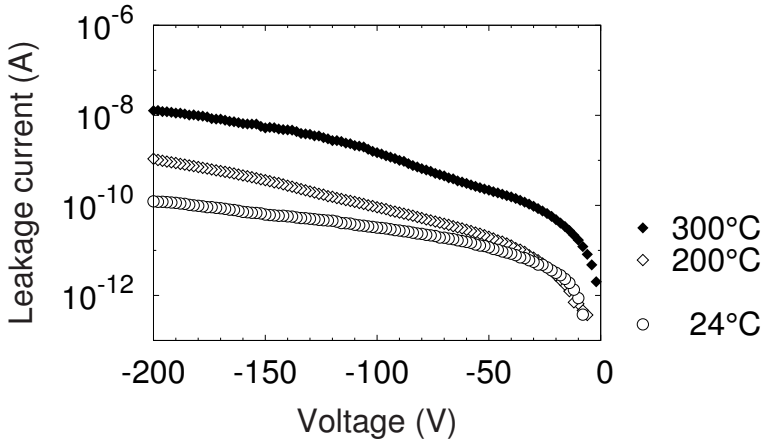

(b) Reverse bias

Figure 5.2: I–V characteristics of the fabricated SiC pn photodiode under a dark condition from room temperature to 300°C. The shape of the device is 0.5×0.5 mm^2 square. The reverse-bias characteristics at 100°C are failed to be measured.

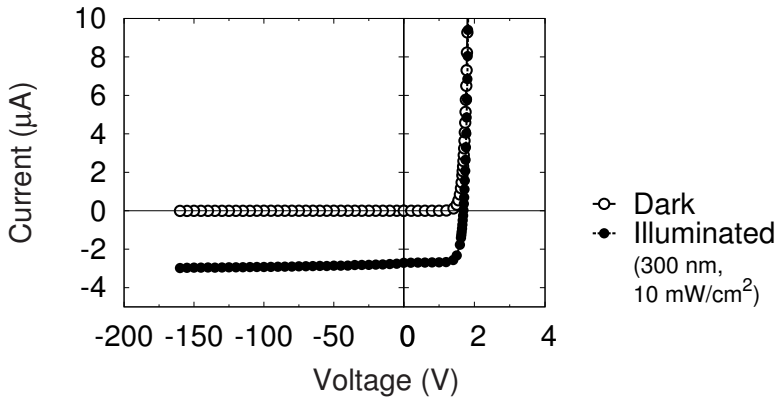

Figure 5.3: *I–V* characteristics of the fabricated device (0.5×0.5 mm^2-square mesa) at 300°C under dark and illuminated (300 nm) conditions. The dark leakage current is less than 5.5 nA even at -150 V.

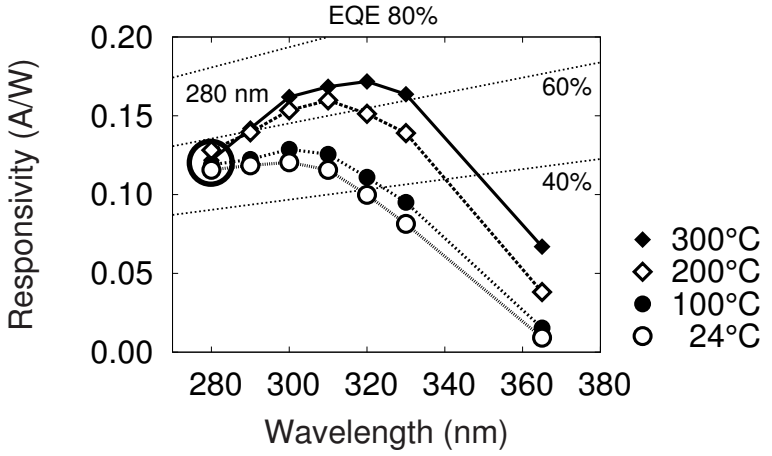

Figure 5.4: Photoresponse and quantum efficiency of the fabricated device as determined by measuring the short-circuit current from 24 to 300°C. The photoresponse increases with increasing temperature, while the temperature dependence of the photoresponse is very small under illumination of 280 nm.

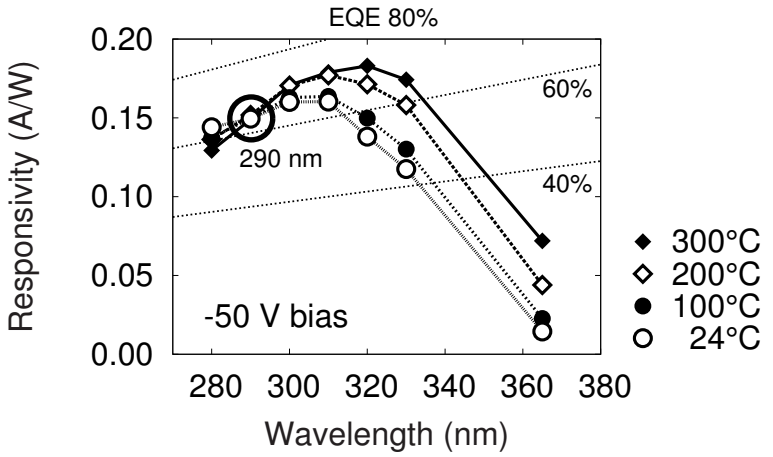

(a) −50 V bias

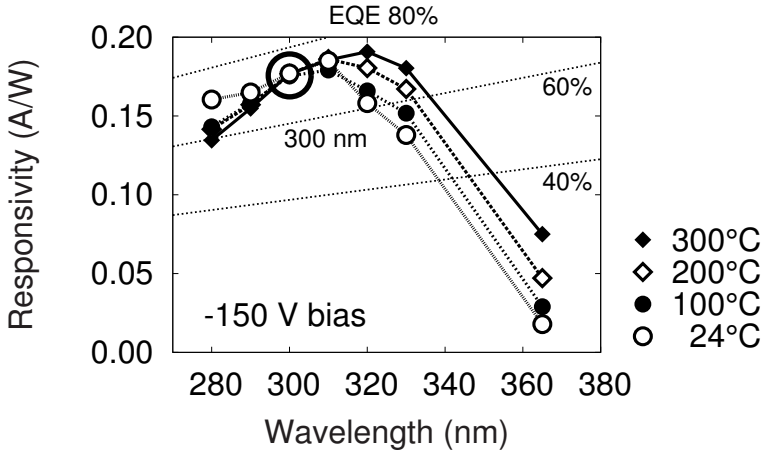

(b) −150 V bias

Figure 5.5: Photoresponse of the fabricated device under reverse-biased conditions [(a) −50 V, (b) −150 V bias] from 24 to 300°C. The wavelength of temperature-independent photoresponse becomes longer with increasing applied reverse-bias voltage.

280-300 nm in this device when the reverse-bias voltage from 0 to 150 V was applied. A higher voltage was required for the temperature-independent photoresponse at longer wavelength illumination.

5.2.5 Photoresponse Simulation

Numerical simulation of the photoresponse of 4H-SiC pn photodiodes under reverse-biased conditions at various temperatures was performed. In this simulation, the photocurrent of a device was calculated as a one-dimensional model shown in Fig. 5.6. When light get into this pn junction, electron–hole pairs are generated within the semiconductor because of light absorption. Generated carriers within the space-charge region are drifted by the electric field and become photocurrent, and generated carriers outside the space-charge region are diffused randomly. Some of these reached the space-charge region and become photocurrent. It is noted that there are recombination centers at surface and epilayer/substrate interface. Some carriers are trapped and recombine at the centers. The total photocurrent consists of the drift current generated in the space-charge region and the diffusion currents generated in the p- and n-type epitaxial layers. The drift current is given by the number of photons absorbed within the space-charge region, and the diffusion current can be deduced from the continuity equation [18].

Absorption coefficients of 4H-SiC at elevated temperatures were estimated from the result obtained in Chapter 3. Summing Eqs. (3.6) and (3.7) for each phonon, i.e., TA-, LA-, and TO-mode phonons, with the fitting parameters listed in Table 3.2, the absorption coefficients of 4H-SiC at each temperature were calculated. Although the wavelength range of the absorption coefficient measurement performed in Chapter 3 is not enough for this simulation, the absorption coefficient of 4H-SiC can be moderately estimated because the dominant optical transition of 4H-SiC is the same in the wavelength range of this simulation, i.e., M–Γ transition [19].

The parameters used for the simulation were as follows: the diffusion lengths of holes and electrons were 4 and 0.3 μm, the diffusion constants of holes and electrons at RT were 3 and 23 cm^2/s, respectively, and the surface recombination velocity was 10^4 cm/s. The temperature dependence of these parameters was ignored in the simulation.

The device structure used for the simulation is the same p^+–n–n^+ structure as shown in Fig. 5.1. The simulation results are shown in Fig. 5.7. The simulation showed that the photoresponse under zero bias condition was almost temperature independent at 280 nm and the wavelength of the temperature-independent photoresponse increased with increasing reverse-bias voltage. The wavelengths of the temperature-independent photoresponse at -50 and -150 V were 292 and 301 nm, which fairly reproduced the experimental results.

The simulation with a different device structure was also carried out. Fig. 5.8 shows the calculated photoresponse of a 4H-SiC pn photodiode where the doping concentration of the n-type epilayer is reduced from 5×10^{15} to 1×10^{15} cm^{-3}. The photoresponse under zero

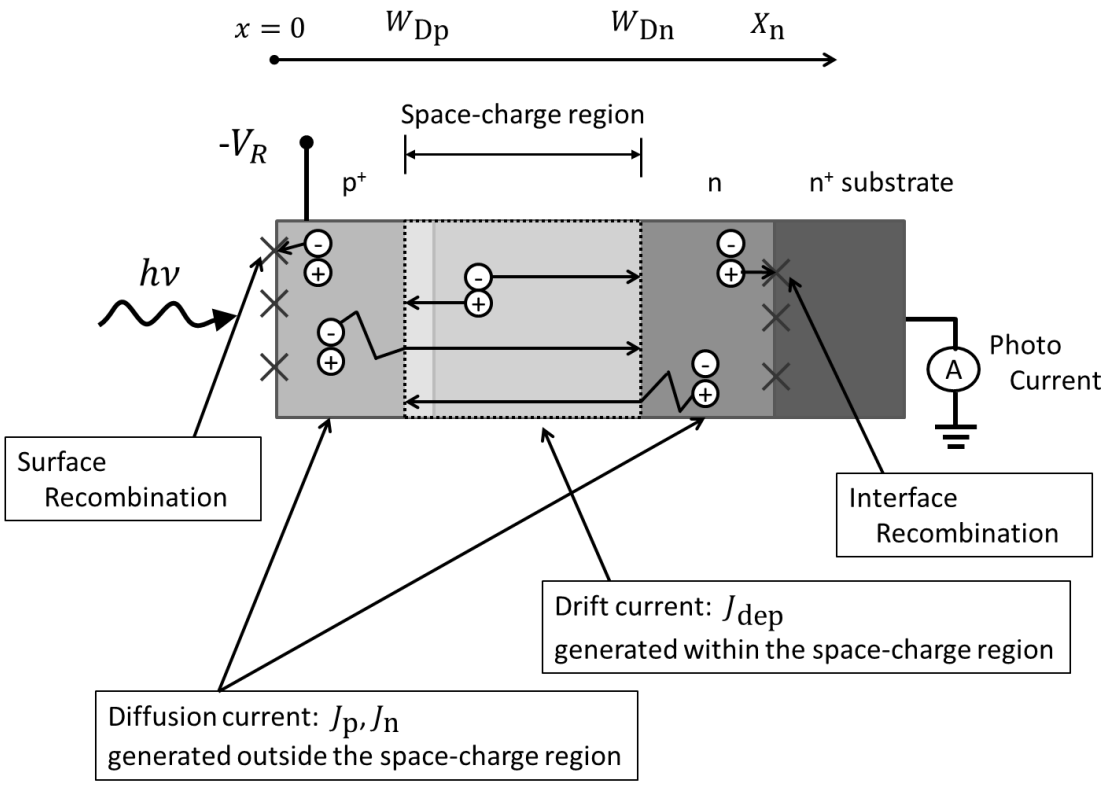

Figure 5.6: Cross-sectional schematics of a pn photodiode. When light get in, carriers are generated and carriers within the space-charge region are drifted by the electric field and become photocurrent. Generated carriers outside the space-charge region are diffused randomly and some of these reached the space-charge region and become photocurrent. There are recombination centers at surface and epilayer/substrate interface. Some carriers are trapped and recombine at the center. The total photocurrent consists of the drift current and the diffusion currents.

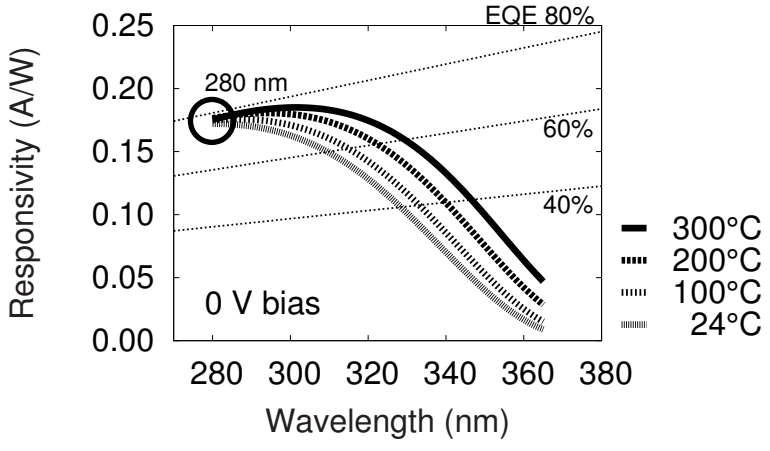

(a)

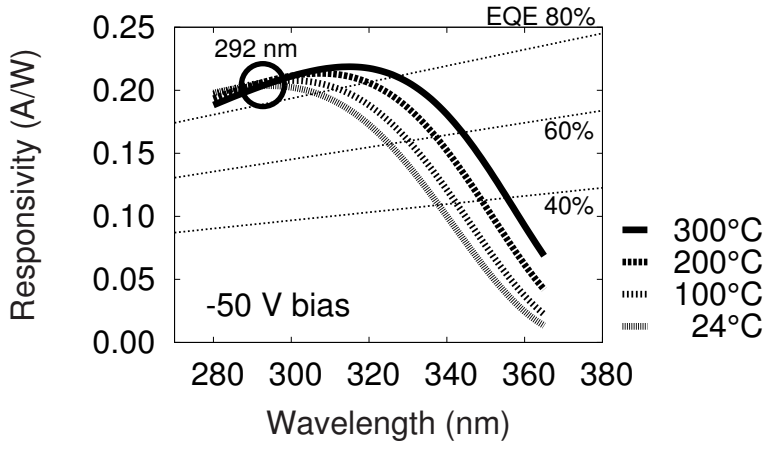

(b)

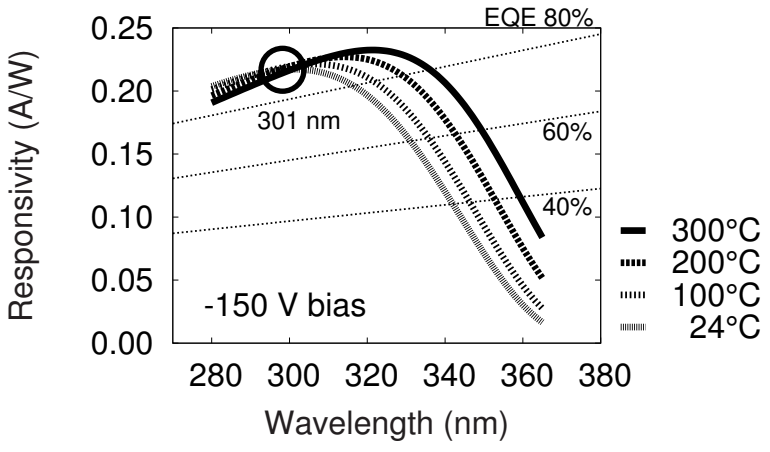

(c)

Figure 5.7: Simulation results of the photoresponse of the fabricated device under various reverse-bias conditions [(a) 0 V, (b) −50 V, (c) −150 V bias] from 24 to 300°C. The wavelength of temperature-independent photoresponse became longer with increasing applied reverse-bias voltage. The simulation fairly reproduces the experimental results.

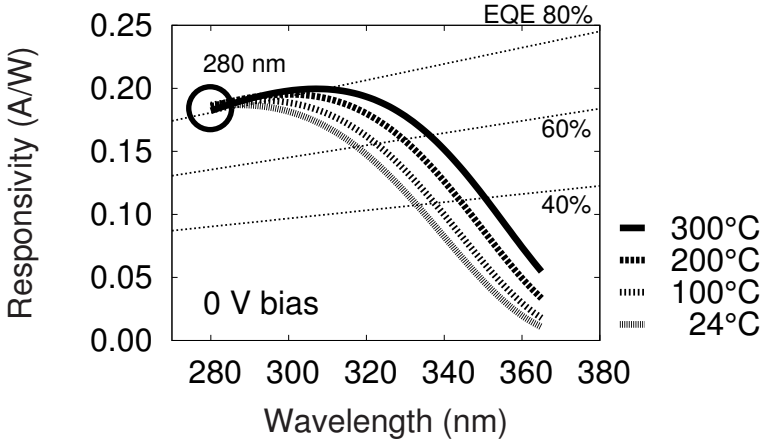

(a)

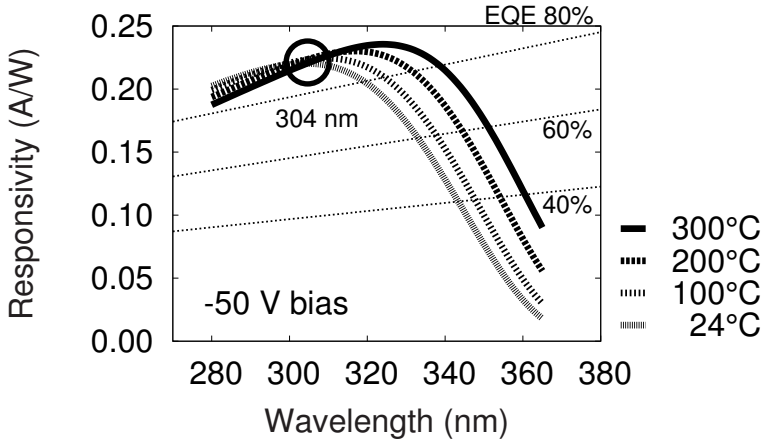

(b)

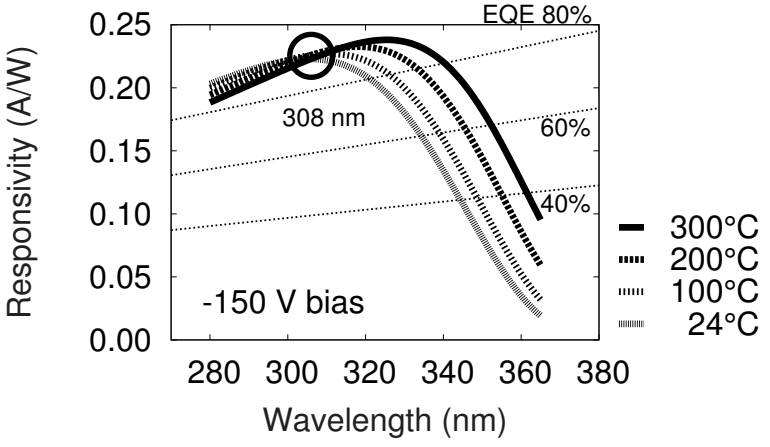

(c)

Figure 5.8: Simulation results of the photoresponse of the device with a different structure (the doping concentration of n-type epitaxial layer was reduced to be 1×10^{15} cm^{-3}). The simulation was carried out under various reverse-bias conditions [(a) 0 V, (b) -50 V, (c) -150 V bias] from 24 to 300°C. The tunable wavelength range was expanded from that of the fabricated device because the width of the space-charge region became larger at same reverse-bias voltage.

bias condition was almost temperature independent at 280 nm and the wavelength of the temperature-independent photoresponse increased with increasing reverse-bias voltage as well as the results of the original device. The wavelengths of the temperature-independent photoresponse under -50 and -150 V were 304 and 308 nm, which were longer than those of the original device.

5.2.6 Discussion

The temperature dependence of the photocurrent is mainly determined by the change in the optical absorption coefficients with temperature. The absorption coefficient at a fixed wavelength increases with increasing temperature due to the decrease of the bandgap. The increase of the absorption coefficient results in two phenomena. The first factor is the change in the distribution of the photon absorption inside pn photodiodes. With increasing absorption coefficient, the number of carriers generated near the surface increases and the number of carriers generated in the deep region decreases. Since the total photocurrent of pn photodiodes consists of the drift current due to carriers generated within the space-charge region and the diffusion currents due to carriers generated outside the space-charge region, impacts of change in the distribution of generated carriers on the photoresponse are strongly influenced by the location of the space-charge region. The second factor is the increase of the surface recombination due to the increase of photogenerated carriers at the surface with increasing absorption coefficient, which has a negative impact on the photoresponse. The temperature dependence of the photoresponse determined by these two phenomena can be cancelled out at a certain wavelength (280 nm at zero bias in this case), because the impact on the photoresponse from the first factor can be positive for a certain wavelength. The wavelength at which a temperature-independent photoresponse is obtained can be modified by changing the device structure, i.e., thicknesses and doping concentrations of epitaxial layers.

Without changing the device structure, the width of the space-charge region can be modulated by applying a reverse-bias voltage. Thus, the wavelength at which the photoresponse is almost temperature independent can be tuned by controlling the reverse-bias voltage. As shown in Fig. 5.5, the wavelength of the temperature-independent photoresponse was successfully changed with increasing reverse-bias voltage. The space-charge region of this device is located from 0.47 to 1.3 μm depth at zero bias, and from 0.44 to 6.3 μm at 150 V bias. Under 280 nm illumination (the penetration depth for this light is 1.5 μm at RT), the temperature dependence of the photoresponse was cancelled at zero bias. And under 300 nm illumination, at which the penetration depth is 3.2 μm at RT, the width of the space-charge region was modulated enough to cancel the temperature dependence of the photoresponse by applying the reverse-bias voltage of 150 V.

The wavelengths of the temperature-independent photocurrent from the simulation fairly agreed with those from the measured data, supporting the proposed mechanism

of temperature-independent photoresponse of SiC pn photodiode described above. However, the photoresponse value of experimental data did not precisely agree with that of the deduced data because 1) roughly-estimated temperature dependence of the absorption coefficient was used and 2) the temperature dependences of the diffusion lengths of minority carriers and surface recombination velocity were ignored in this simulation. Measurements of those physical parameters are very important to design a device with high accuracy. From the simulation results of the different device structure, results which are shown in Fig. 5.8, the tunable wavelength range can be expanded by using an n-type epitaxial layer with lower concentration because the width of the space-charge region becomes larger at the same reverse-bias voltage.

5.3 Electrical Characteristics of SiC pn Photodiodes up to 600°C

5.3.1 Device Fabrication Process

Device structure fabricated for this investigation is almost the same as the schematic shown in Fig. 5.1. Dimensionwise, there are two differences from Fig. 5.1. The thickness of the top p-type epitaxial layer is 440 nm, and the mesa height is 1.5 μm. These changes have been caused by employing slightly different wafers and RIE condition.

In terms of passivation process, I have employed two different processes for surface passivation. The first one is ordinary dry thermal oxidation process at 1300°C for 40 min. This process formed 40-nm-thickness oxide at the surface. The second one is dry thermal oxidation with the same condition followed by nitric oxide (NO) annealing at 1250°C for 1 h. This passivation process has been carried out to try reducing the reverse leakage current of fabricated devices.

5.3.2 Measurement Setup

The electrical characteristics of the fabricated devices were measured from RT up to 600°C. The measurements were performed in a vacuum chamber with a small window, which allows to illuminate UV light to the sample. I–V characteristics of SiC pn junction were measured under dark condition. Optical responsivity measurements were carried out using a 300 W xenon lamp with band pass filters. The wavelength range was between 260 and 390 nm.

5.3.3 Current–Voltage Characteristics of SiC pn Junction

Fig. 5.9 shows the I–V characteristics of a fabricated SiC pn diode (passivated with dry thermal oxidation) under a dark condition from RT to 600°C. The shape of the device is 847-μm-diameter circle. As shown in the forward-bias characteristics [Fig. 5.9(a)], the

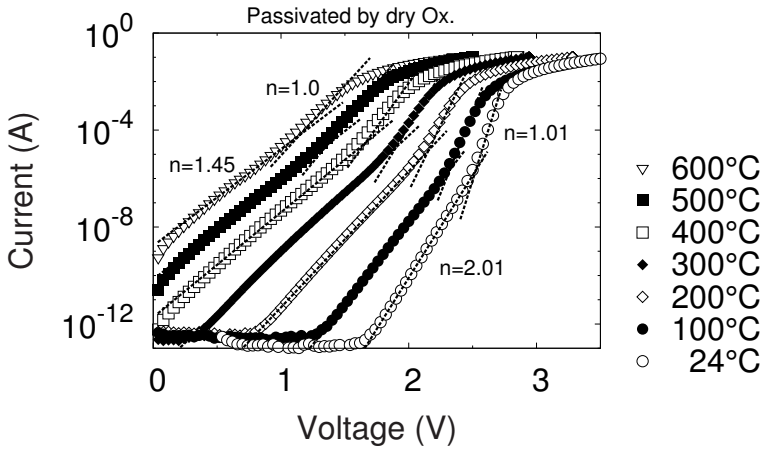

(a) Forward bias

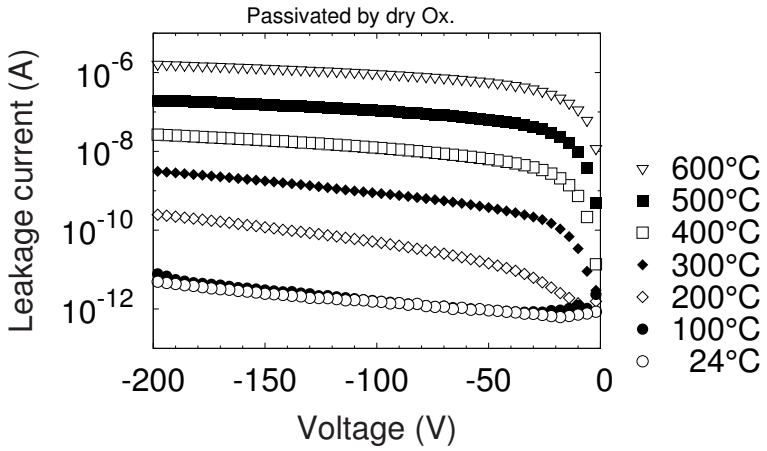

(b) Reverse bias

Figure 5.9: *I–V* characteristics of the fabricated SiC pn diode (passivated with dry thermal oxidation) under a dark condition from room temperature to 600°C. The shape of the device is 847-μm-diameter circle. The leakage currents at 24 and 100°C were below the measurement limit of the setup.

device worked as a diode up to 600°C. The forward I–V characteristics shifted to lower voltage with increasing temperature. It is caused by the decrease of the diffusion potential of the pn junction. From Fig. 5.9(a), the slope of the forward current consisted of two components. The ideality factor n of the recombination current component which is two ($n = 2$) at RT was determined to be 2.01. By subtracting this recombination current component from the experimental data, forward current with an n of 1.01 could be obtained. This forward current was the diffusion current component. From the current intercept of the line with $n = 1$, the ideal leakage current of the device can be deduced. At RT, the ideal leakage current was determined to be 8.5×10^{-49} A for this device. In the same manner, the ideality factor of the recombination and diffusion current component at 600°C were 1.45 and 1.0, respectively. The ideal leakage current at 600°C was determined to be 1.5×10^{-11} A. The obtained ideality factors and ideal leakage currents at each temperature are listed in Table 5.1. The ideality factor of recombination current component decreased with increasing temperature. It is caused by the increase of the diffusion current component at lower voltage region, resulting in that recombination current component could not be separated from diffusion current component.

The reverse-bias characteristics at 24 and 100°C were almost the same because the leakage currents at these temperature were below the measurement limit of the setup[1]. It is noted that the I–V characteristics of this device up to 300°C are different from Fig. 5.2 because the surface passivation was carried out with cleaner oxidation equipment for the device. With increasing temperature, the leakage current increased exponentially. Arrhenius plot of the reverse leakage current at −100 V bias is shown in Fig. 5.10. The activation energy of the leakage current was 1.1 eV. Fig. 5.11 shows the leakage current of fabricated SiC pn diodes (passivated with dry thermal oxidation) at 400, 500, and 600°C as a function of perimeter at −100 V. As shown in Fig. 5.11, the leakage current is proportional to the perimeter.

Employing the passivation with dry thermal oxidation followed by NO annealing, the I–V characteristics of the fabricated SiC pn diode resulted in Fig. 5.12. The device geometry was same as a device of Fig. 5.9. From the forward characteristics shown in Fig. 5.12(a), the I–V curve shifted to lower voltage with increasing temperature as well as those of the device with the conventional dry-thermal-oxidation passivation. The "ledges" were appeared in the I–V curves, hence the ideality factors could not be obtained.

Similar to the device passivated with only dry thermal oxidation, the leakage current was under the measurement limit at low temperature and increased significantly with increasing temperature. As shown in Figs. 5.9 and 5.12, the leakage current was reduced by a factor of 20, compared with only dry thermal oxidation, suggesting that the leakage current caused at the perimeter significantly reduced by the passivation of dry thermal oxidation followed by NO annealing. Arrhenius plot of the reverse leakage current at −100 V bias is shown

[1]The leakage current caused by the measurement setup at 200 V was around 10 pA at RT

Table 5.1: Ideality factors and ideal leakage current of the fabricated SiC pn diode (847-μm-diameter circle-shape mesa, passivated with dry thermal oxidation) under a dark condition up to 600°C. The ideality factor of the recombination current component (Rec.) of which is two ($n = 2$) and that of the diffusion current component (Diff.) of which is one ($n = 1$) are shown. The ideal leakage currents were determined from the current intercept of the line with $n = 1$. The measured leakage currents under a −100-V-bias condition are also listed at each temperature. Note that the measured leakage currents below 200°C are not precise since these values are affected by the measurement limit of the setup.

T (°C)	Idealty factor		Ideal leakage current (A)	Measured leakage current (A)
	Rec.	Diff.		(−100 V bias)
24	2.01	1.01	8.5×10^{-49}	(1.5×10^{-12})
100	2.01	1.01	2.1×10^{-37}	(6.1×10^{-12})
200	1.9	0.98	5.5×10^{-29}	(4.9×10^{-11})
300	1.8	1.02	8.2×10^{-22}	8.7×10^{-10}
400	1.73	1.03	2.5×10^{-17}	1.2×10^{-8}
500	1.6	1.01	4.0×10^{-14}	1.1×10^{-7}
600	1.45	1.0	1.5×10^{-11}	9.5×10^{-7}

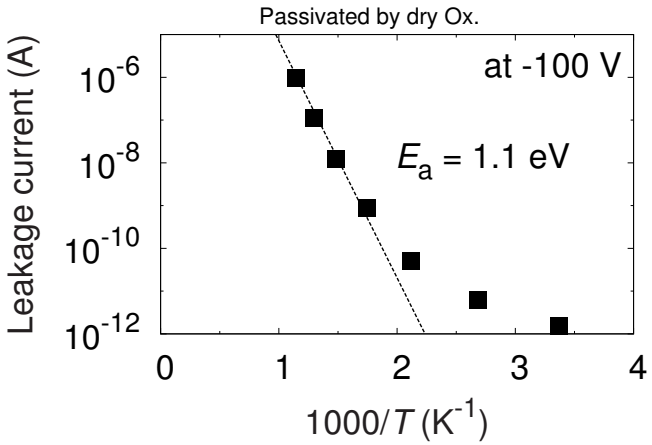

Figure 5.10: Arrhenius plot of the leakage current at -100 V of the SiC pn diode (847-μm-diameter circle-shape mesa, passivated with dry thermal oxidation). Excepting the data below 200°C, which are below the measurement limit of the setup, the activation energy is 1.1 eV.

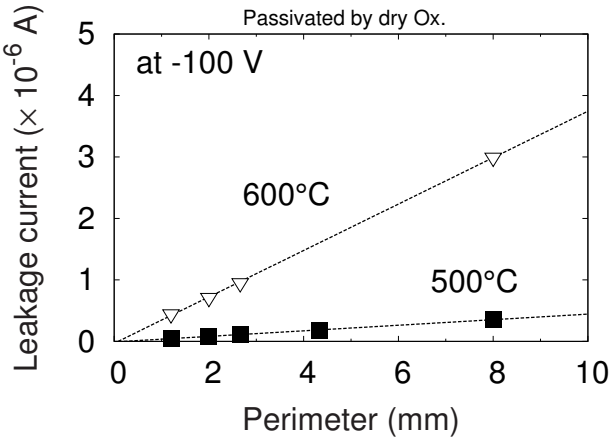

(a) 500 and 600°C

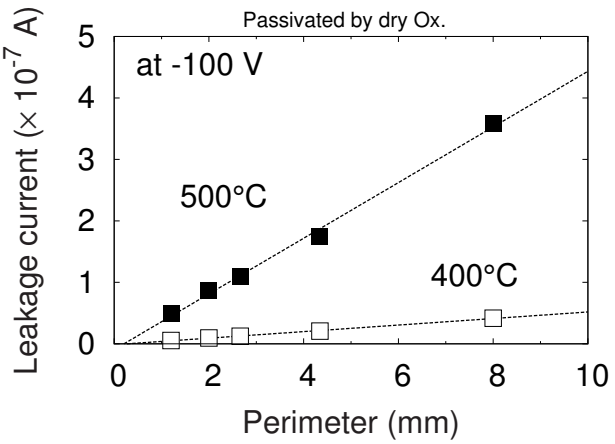

(b) 400 and 500°C

Figure 5.11: Perimeter dependence of the leakage current at -100 V of the SiC pn diodes (passivated with dry thermal oxidation) at (a) 500 and 600°C and (b) 400 and 500°C. The leakage current is proportional to the perimeter up to 600°C, suggesting that the origin of the leakage current is related to the leakage at the perimeter.

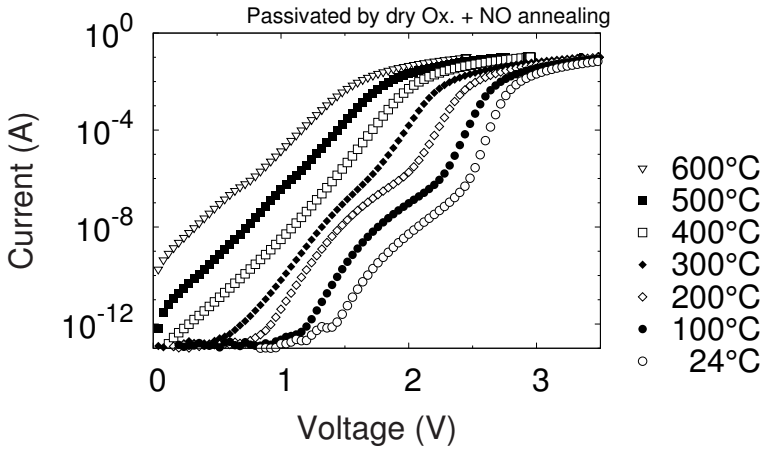

(a) Forward bias

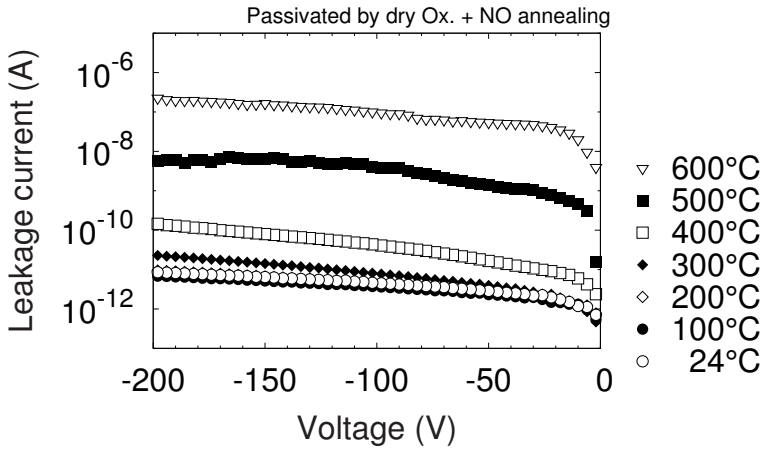

(b) Reverse bias

Figure 5.12: *I–V* characteristics of the fabricated SiC pn diode (passivated with dry thermal oxidation followed by NO annealing) under a dark condition from room temperature to 600°C. The shape of the device is 847-μm-diameter circle. The leakage currents at 24, 100, and 200°C were below the measurement limit of the setup.

in Fig. 5.13. The activation energy of the leakage current was 2.0 eV. Fig. 5.14 shows the leakage current of fabricated SiC pn diodes (passivated with dry thermal oxidation and NO annealing) at 400 and 500°C as a function of perimeter at −100 V bias, indicating that the leakage current is proportional to the perimeter.

5.3.4 Photoresponse

The photoresponse of the SiC pn photodiode passivated with dry thermal oxidation followed by NO annealing as a function of incident wavelength is shown in Fig. 5.15. The photoresponse was determined by measuring the short-circuit current from 24 to 500°C. The external quantum efficiency over 40 % was obtained for wavelengths of 280-365 nm at 500°C. The device successfully worked as a photodetector up to 500°C. As shown in Fig. 5.15, the photoresponse for longer wavelength illuminations increased with increasing temperature, while that for shorter wavelength decreased. Temperature-independent photoresponse was not obtained for any wavelength in the whole range of temperature between 24 and 500°C. On the other hand, the temperature dependence of the photoresponse was small at 270 and 280 nm illuminations between 24 and 300°C, and at 320 nm illumination between 300 and 500°C. Note that the photoresponse at 600°C could not be obtained because the device was broken at this temperature.

5.3.5 Discussion

Reverse leakage current of a mesa-type pn diode consists of some components. The first component is the diffusion current in the neutral region, i.e., the ideal leakage current. However, the diffusion current of SiC pn diodes under reverse-bias condition is very small as listed in Table 5.1 because of the large bandgap. Comparing to the obtained reverse leakage current of fabricated diodes, the contribution from this component is negligible. The second component is the generation current in the space-charge region. The generation current could be divided into bulk and perimeter generation component. As shown in Fig. 5.11, the leakage current is proportional to the perimeter. It suggests that the origin of the leakage current is related to the leakage at the perimeter. The intercept of the plot in Fig. 5.11 is almost zero, suggesting that the bulk generation process is negligible. The activation energy of the leakage current shown in Fig. 5.10 was 1.1 eV. The leakage current caused by carrier generation has the activation energy of $E_g/2$ where E_g is the bandgap of the material, i.e., $E_g/2 = 1.6$ eV for 4H-SiC. Since the activation energy of the experimentally obtained leakage current roughly agreed with $E_g/2$, the origin of the leakage current should be the carrier generation at the perimeter.

In order to reduce the reverse leakage current of SiC pn diodes, the leakage at the perimeter should be eliminated. Although surface passivation process could reduce the leakage at the perimeter, the devices shown in Figs. 5.9 and 5.11, which were already

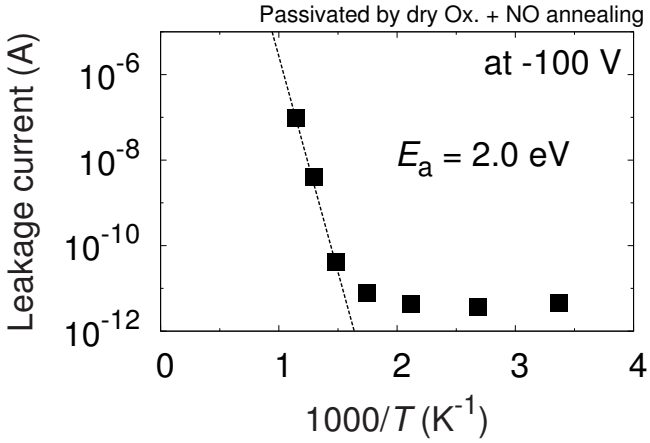

Figure 5.13: Arrhenius plot of the leakage current at -100 V of the SiC pn diode (847-μm-diameter circle-shape mesa, passivated with dry thermal oxidation followed by NO annealing). Excepting the data below 300°C, which are below the measurement limit of the setup, the activation energy is 2.0 eV.

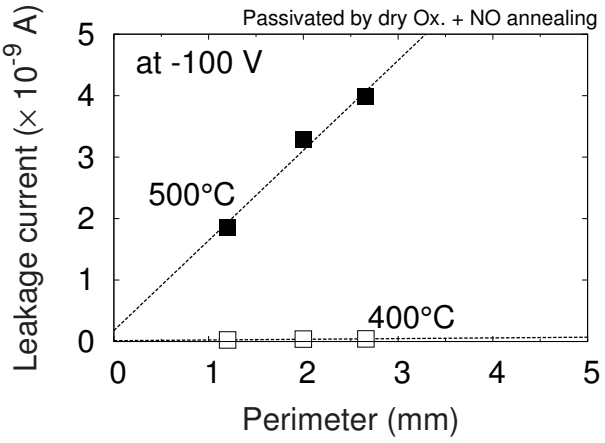

Figure 5.14: Perimeter dependence of the leakage current at -100 V of the SiC pn diodes (passivated with dry thermal oxidation followed by NO annealing) at 400 and 500°C. The leakage current is proportional to the perimeter, suggesting that the origin of the leakage current is related to the leakage at the perimeter.

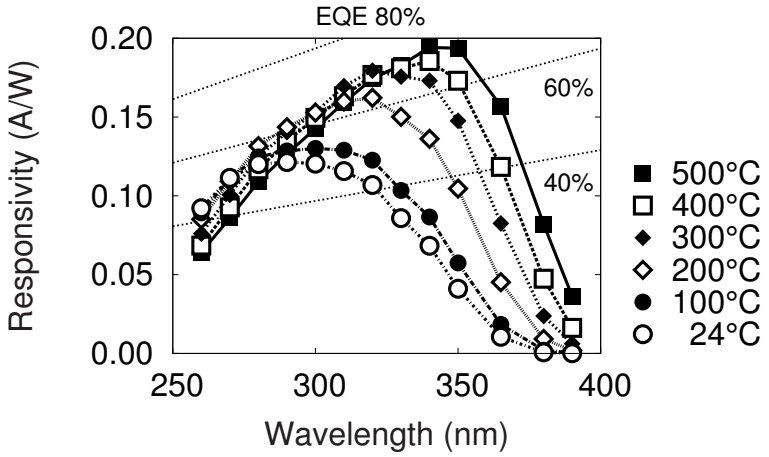

Figure 5.15: Photoresponse and quantum efficiency of the fabricated SiC pn photodiode (passivated with dry thermal oxidation followed by NO annealing) as determined by measuring the short-circuit current from 24 to 500°C. The device successfully work as a photodetector up to 500°C.

passivated with dry thermal oxidization, had considerable reverse-bias leakage. On the other hand, it has been reported that nitridation process after forming SiO_2 layer, i.e., annealing in nitrous oxide (N_2O) or NO, shows lower interface trap density, process which has attracted much attention to improve the performance of SiC MOSFETs [20]. In other words, this process also can be employed to reduce the leakage current at the surface (perimeter) of SiC pn diodes. As shown in Fig. 5.12, which depicts the I–V characteristics of a SiC pn diode with dry thermal oxidation followed by NO annealing passivation, the leakage current was significantly reduced even at high temperature up to 600°C from the result of the device with the conventional passivation. The activation energy of the leakage current shown in Fig. 5.10 was 2.0 eV, suggesting that the generation current component was significantly reduced. This result should lead to high-temperature operation of SiC pn photodiodes.

The ledges were appeared in forward I–V curves of the SiC pn diode with dry thermal oxidation and NO annealing passivation as shown in Fig. 5.12(a). It suggests that parasitic diodes are formed in the device. Since forward I–V curves of a SiC pn diode with conventional surface passivation shown in Fig. 5.9(a) didn't have ledges, the parasitic diodes are probably caused by the NO annealing. Although the device with dry thermal oxidation followed by NO annealing passivation causes the ledges in the forward characteristics, the passivation method is usable for enhancing the performance of SiC pn photodiodes because pn photodiodes are typically utilized under reverse-bias conditions.

As shown in Fig. 5.14, the leakage current of the fabricated devices passivated by dry thermal oxidation and NO annealing was proportional to the perimeter, suggesting that the leakage current still occurred at the perimeter. The leakage current may be reduced further by optimizing passivation condition.

As shown in Fig. 5.15, the fabricated SiC pn photodiode with dry thermal oxidation followed by NO annealing passivation successfully worked as a photodiode up to 500°C. With increasing temperature, the absorption coefficient of SiC increases, leading to the increase of the number of absorbed photon and generated carrier at longer wavelength region. As a result, the photoresponse increased with increasing temperature as described in Section 5.2.6. On the other hand, in shorter wavelength region, the photoresponse decreased with increasing temperature. The absorption coefficient increase causes the increase of the number of photon absorbed near the surface, resulting in the increase of the carrier which recombines at the surface. It induces the negative impact to the photoresponse, and causes the decrease of the photoresponse when the impact becomes large enough.

It is noted that the reliability of the device with dry thermal oxidation and subsequent NO annealing passivation more than 500°C is worse than that of the device with conventional passivation. A larger amount of the device were broken at 500 and 600°C comparing to that of the conventional device and the photoresponse at 600°C could not be obtained. Optimization of the passivation condition is necessary to enhance the reliability at such temperature.

5.4 Summary

In this chapter, 4H-SiC pn photodiodes were fabricated and the electrical characteristics of dark and UV-illuminated conditions were investigated between RT and high temperature. From RT to 300°C, the temperature-independent photoresponse was obtained for targeted-wavelength illumination at zero bias. By applying the reverse-bias voltage up to 150 V, the wavelength of the temperature-independent photoresponse was successfully tuned to longer wavelength on the same device. Simulation of the photoresponse under reverse-biased conditions at various temperatures was performed, and the simulation fairly represented the experimental results. I propose that controlling the reverse-bias voltage is an effective way of achieving a temperature-independent photoresponse at targeted wavelengths in addition to optimizing the device structure design.

I also investigated the electrical characteristics of SiC pn photodiodes up to 600°C. The reverse leakage current of fabricated mesa-type SiC pn diodes originated from the leakage at the perimeter of the devices. Utilizing the passivation process of dry thermal oxidation followed by NO annealing, which is utilized to reduce interface trap density for SiC MOSFETs, the leakage current of SiC pn diodes was significantly reduced. Finally, the photodetector operation of the fabricated device up to 500°C was successfully demonstrated. Surface passivation with thermal oxidation and subsequent nitridation can realize high-temperature operation of SiC pn photodiodes with low dark current.

References

[1] M. Mehregany and C. A. Zorman, Thin Solid Films **355**, 518 (1999).

[2] R. M. Sarro, Sens. Actuators A **82**, 210 (2000).

[3] M. Mehregany, C. A. Zorman, S. Roy, A. J. Fleischman, C. H. Wu, and N. Rajan, Int. Mater. Rev. **45**, 85 (2000).

[4] A. Klumpp, U. Schaber, H. L. Offereins, K. Kühl, and H. Sandmaier, Sens. Actuators A **41**, 310 (1994).

[5] D. Gao, M. B. J. Wijesundara, C. Carraro, R. T. Howe, and R. Maboudian, IEEE Sens. J. **4**, 441 (2004).

[6] J. B. Casady and R. W. Johnson, Solid State Electron. **39**, 1409 (1996).

[7] P. G. Neudeck, R. S. Okojie, and L. Y. Chen, Proc. IEEE **90**, 1065 (2002).

[8] G. Kelner, S. Binari, M. Shur, K. Sleger, J. Palmour, and H. Kong, Mater. Sci. Eng. B **11**, 121 (1992).

[9] J. W. Palmour, H. S. Kong, and R. F. Davis, J. Appl. Phys. **84**, 2168 (1988).

[10] T. Billon, T. Ouisse, P. Lassagne, C. Jassaud, J. L. Ponthenier, L. Baud, N. Bécourt, and P. Morfouli, Electron. Lett. **30**, 170 (1994).

[11] T. Kimoto, T. Urushidani, S. Kobayashi, and H. Matsunami, IEEE Electron Device Lett. **14**, 548 (1993).

[12] A. L. Spetz, A. Baranzahi, P. Tobais, and I. Lundström, Phys. Stat. Sol. A **162**, 493 (1997).

[13] R. B. Campbell and H. C. Chang, Solid State Electron. **10**, 949 (1967).

[14] P. Glasow, G. Ziegler, W. Suttrop, G. Pensl, and R. Helbig, Proc. SPIE **868**, 40 (1987).

[15] D. M. Brown, E. T. Downey, M. Ghezzo, J. W. Kretchmer, R. J. Saia, Y. S. Liu, J. A. Edmond, G. Gati, J. M. Pimbley, and W. E. Schneider, IEEE Trans. Electron Devices **40**, 325 (1993).

[16] J. Edmond, H. Kong, A. Suvorov, D. Waltz, and C. Carter, *Jr.*, Phys. Stat. Sol. A **162**, 481 (1997).

[17] T. Kimoto, N. Miyamoto, and H. Matsunami, IEEE Trans. Electron Devices **46**, 471 (1999).

[18] S. M. Sze and K. K. Ng, *Physics of Semiconductor Devices, 3rd ed.* (John Wiley & Sons, New York, 2006).

[19] H. -Y. Cha and P. M. Sandvik, Jpn. J. Appl. Phys. **47**, 5423 (2008).

[20] M. Noborio, J. Suda, S. Beljakowa, M. Krieger, and T. Kimoto, Phys. Stat. Sol. A **206**, 2374 (2009).

Chapter 6

Conclusions

6.1 Conclusions

Fundamental study on wide-bandgap-semiconductor microelectromechanical systems (MEMS) and photodetectors has been conducted in the present study to realize high functional and high performance integrated smart sensors. In this thesis, three main topics have been extensively investigated: 1) determination of the optical properties of silicon carbide (SiC), gallium nitride (GaN), and aluminum nitride (AlN) from room temperature (RT) to very high temperature (Chapters 2 and 3), 2) investigation of SiC micromachining process and fabrication of MEMS structures made of entirely single-crystalline SiC (Chapter 4), and 3) investigation of high-temperature operation of SiC pn photodiodes (Chapter 5). The main conclusions obtained in this study can be summarized as follows.

In Chapter 2, the temperature dependence of the refractive indices of 4H-SiC, GaN, and AlN from RT to 500°C were investigated to realize tunable filters which utilizes the thermo-optic effect. The refractive indices of 4H-SiC, GaN, and AlN were measured over a wide spectral range from infrared (1700 nm) to ultraviolet (UV) near the bandgaps of those materials (392 nm for SiC, 367 nm for GaN, and 217 nm for AlN). The thermo-optic coefficients for the ordinary refractive indices of these materials were accurately determined over a wide temperature range. These thermo-optic coefficients can be expressed as experimental polynomial fits in the wavelength range. At 450 nm, the thermo-optic coefficients of 4H-SiC, GaN, and AlN were determined to be 7.8×10^{-5}, 1.6×10^{-4}, and 3.6×10^{-5} K^{-1}, respectively. Since the devices based on the thermo-optic effect, e.g., tunable filters, require a large thermo-optic coefficient, GaN is the most suitable material for such devices.

Optical simulation of a band-pass filter based on GaN was also conducted at different temperatures by utilizing the determined thermo-optic coefficients in this study. The red-shift of the transparent wavelength from RT to 500°C was calculated to be approximately 9 nm, which is much larger than the width of the pass band ($\sim$ 0.1 nm). The simulation has demonstrated that the modulation of the transparent wavelength of a GaN-based optical filter can be attained to tunable filter application.

The results obtained thus far are useful for the design of GaN-based optoelectronic devices as well as SiC- and GaN-based wavelength-tunable band-pass filters and photonic crystals in the spectrum range from the infrared to UV regions that actively utilize the thermo-optic effect.

In Chapter 3, the temperature dependence of the absorption coefficients of 4H- and 6H-SiC between RT and 300°C were determined to design SiC photodetectors operating at high temperature. The absorption coefficient was determined at each temperature up to about 400 cm^{-1} (4H-SiC) and 500 cm^{-1} (6H-SiC). Redshift of the absorption edge at elevated temperature was observed, redshift which is caused by the decrease of the bandgap with increasing temperature. Temperature dependence of the phonon occupation number is also significant to explain the temperature dependence of the absorption coefficient of SiC. Employing TA-, LA-, and TO-mode phonons, the measured data were fairly fitted with the theoretical equation. Although the measured wavelength range was not enough to design SiC photodetectors, this study demonstrated that the temperature dependence of the absorption coefficient of SiC could be determined precisely in wide range of wavelength by the transmission measurement.

In Chapter 4, suspended bridge and cantilever structures of all-single-crystalline 4H-SiC were fabricated. From the numerical simulation using the finite element method (FEM), An SiC bridge structure with a sub-micron air gap between the bridges and the bottom is required to electrostatically actuate the bridges with a moderate operating voltage below 10 V. To fabricate such a suspended structure, I employed the combination use of patterning of devices with reactive ion etching (RIE) and sacrificing an n-type or p-type SiC layer with photoelectrochemical (PEC) or electrochemical (EC) etching, respectively. PEC and EC etching of SiC showed selectivity in doping-type, where n-type SiC is removed by PEC and p-type SiC by EC.

A suspended bridge structure of all-single-crystalline SiC was fabricated by utilizing PEC etching. Fabricated bridge structure has the widths of 4 and 10 μm, the lengths of 50-200 μm, and the thickness of 100 nm. The gap between the bridge and the bottom is 700 nm. Although a sacrificial n-type SiC layer was not completely removed by PEC etching and remained as porous SiC, the porous-SiC layer was removed by utilizing thermal oxidation and subsequent SiO_2 removal by HF solution, resulting in the successful fabrication of the bridge structure entirely composed of 4H-SiC. Electrostatic actuation of the fabricated bridges was also demonstrated by applying the voltage of 20 V.

I also fabricated single-crystalline 4H-SiC cantilevers on a 4H-SiC substrate by EC etching with no illumination. The cantilever structure was successfully fabricated. The width and the lengths of the cantilevers are 15 μm and 80-140 μm, respectively. The thickness of the cantilever is 900 nm. The maximum quality (Q) factor of the 4H-SiC cantilevers was 230,000, which was more than 10 times higher than that of conventional 3C-SiC cantilevers fabricated on an Si substrate. Resonance characteristics of fabricated SiC cantilevers with different dimensions were also measured, and Q-factor of about 200,000 was obtained in all

SiC cantilevers. It is noted that the Q-factors of fabricated all-single-crystalline SiC cantilevers are much larger than the reported value of single-crystalline silicon cantilever with similar dimensions (∼5,000). This very high Q-factor makes 4H-SiC MEMS very attractive for high-sensitivity sensors.

In Chapter 5, 4H-SiC pn photodiodes were fabricated and the electrical characteristics of dark and UV-illuminated conditions were investigated between RT and high temperature. From RT to 300°C, the photoresponse of fabricated SiC pn photodiodes was varied by the temperature, while the temperature-independent photoresponse was obtained under 280-nm-illuminated condition at zero bias. By applying the reverse-bias voltage up to 150 V, the wavelength of the temperature-independent photoresponse was tuned to a longer wavelength on the same device. Simulation of the photoresponse under reverse-biased conditions at various temperatures was performed, and the simulation fairly represented the experimental results. I have proposed that controlling the reverse-bias voltage is an effective way of achieving a temperature-independent photoresponse at targeted wavelengths in addition to optimizing the device structure design.

The electrical characteristics of SiC pn photodiodes up to 600°C were also investigated. To operate the devices at such high temperature, the reverse leakage current should be reduced. This study has clarified that the reverse leakage current of fabricated mesa-type SiC pn diodes mainly originate from the leakage at the perimeter of the devices up to 600°C. By utilizing the passivation process of dry thermal oxidation followed by nitric oxide (NO) annealing, which is utilized to reduce interface trap density for SiC metal-oxide-semiconductor field-effect transistors, the leakage current of SiC pn diodes was significantly reduced by a factor of 20, compared with conventional surface passivation. Finally, I successfully demonstrated the photodiode operation up to 500°C. Surface passivation with thermal oxidation and nitridation can realize high-temperature operation of SiC pn photodiodes with low dark current.

6.2 Future Outlook

Through this study, several bases for wide-bandgap-semiconductor integrated smart sensors have been established. Integrated smart sensors such as micro-scale spectrometer made of wide-bandgap-semiconductor thermo-optic tunable optical filters and high-temperature photodetectors can be realized. Monolithically integrated SiC sensor systems operating up to high temperature involving MEMS, electronic sensors, and circuits are as well. However, several issues still remain to be solved for realization of the integrated smart sensors.

- **Fabrication of wide-bandgap-semiconductor tunable filters:**

  The thermo-optic coefficients of wide bandgap semiconductors have been precisely determined, and the usefulness of a GaN-based tunable filter has been demonstrated by optical simulation using determined thermo-optic coefficients. However, tunable

filter devices based on wide bandgap semiconductors are not fabricated yet. From the optical simulation of a GaN-based tunable filter, this device can be used for the application which needs high resolution in wavelength. In other words, distributed Bragg reflectors (DBRs) should be formed at both side of the tunable filter to narrow the pass band of the filter. Such narrow pass band can be achieved by utilizing DBRs which have large difference in refractive index of the composed layer materials. A large number of stacked-layer pairs also contribute to narrowing the pass band.

For GaN-based filters, DBRs can be formed by epitaxial growth of aluminum gallium nitride (AlGaN) and GaN. Although high-aluminum-composition [1] and many-layer-pair [2] AlGaN/GaN DBRs were reported, it is difficult to obtain AlGaN/GaN DBRs which can realize such high resolution in GaN-based band-pass filters. One of the promising solutions is the employment of the growth method of molecular beam epitaxy (MBE), which can grow group-Ⅲ nitrides at relatively low temperature, expected to realize large number of stacked layer pairs. Low-temperature growth of group-Ⅲ nitrides conducted by MBE lead to reducing crack formation since an effect of the mismatch of the thermal expansion is relatively small.

Furthermore, such GaN-based tunable filters should be formed on a wide-bandgap-semiconductor photodetector to realize a micro-scale UV spectrometer proposed in this study. SiC is one of the most attractive candidates for the material of the photodetector because epitaxial growth of group-Ⅲ nitrides on SiC substrates with MBE has been extensively investigated [3, 4].

- **Determination of the temperature dependence of the optical absorption coefficient of SiC in short-wavelength region:**

  Although this study has precisely determined the temperature dependence of the optical absorption coefficient of SiC in a wide range of wavelengths, the data at shorter wavelength should be determined to design high-temperature operation of SiC photodiodes precisely. As shown in Chapter 5, SiC photodiodes will be typically used at such wavelengths to obtain higher quantum efficiency.

  The optical absorption coefficients in the short-wavelength region can be determined by the transmission measurement with thinner samples. To fabricate such thin samples, deep etching process with RIE can be utilized. Doping-type selective etching processes by PEC and EC etching, described in Chapter 4, are also attractive for such fabrication. A specific-doping-type epitaxial layer, i.e., p-type SiC for PEC etching and n-type SiC for EC, can remain as a high-uniform-thickness thin membrane structure by these etching processes.

- **High-temperature operation of all-single-crystalline SiC MEMS devices:**

  Suspended bridge and cantilever structures composed entirely of single-crystalline 4H-SiC have been successfully fabricated by employing doping-type selective etching of

PEC and EC etching processes, and electrostatic actuation of the bridge has been demonstrated. However, the operation of the devices in harsh environments has not been demonstrated yet. All-single-crystalline SiC MEMS devices are expected to operate in harsh environments such as high-temperature ambience, and furthermore, the devices can be combined with SiC high-temperature semiconductor devices. This combination leads to realize integrated systems operating in high-temperature environments. Therefore, high-temperature operation of all-single-crystalline SiC MEMS devices should be investigated.

One of the most important issues is the lack of the knowledge of the mechanical properties of 4H- and 6H-SiC, which are used for all-single-crystalline SiC MEMS devices, especially at high temperature. Mechanical properties such as the Young's modulus can be determined by evaluating electrostatically actuated MEMS structures [5, 6]. Since electrostatic actuation of the all-single-crystalline SiC MEMS device has been demonstrated, the mechanical properties of the SiC can be revealed. It should lead to the precise design all-single-crystalline SiC MEMS devices and realization of the high-temperature operation.

Achieving these challenges, high-functional and high-performance integrated smart sensors made of wide bandgap semiconductors should be realized in the future.

References

[1] F. Natali, D. Byrne, A. Dussaigne, N. Grandjean, J. Massies, and B. Damilano, Appl. Phys. Lett. **82**, 499 (2003).

[2] M. Diagne, Y. He, H. Zhou, E. Makarona, A. V. Nurmikko, J. Han, K. E. Waldrip, J. J. Figiel, T. Takeuchi, and M. Krames, Appl. Phys. Lett. **79**, 3720 (2001).

[3] M. Horita, Dr. Thesis, Faculty of Engineering, Kyoto University, Kyoto, 2009.

[4] H. Okumura, Dr. Thesis, Faculty of Engineering, Kyoto University, Kyoto, 2012.

[5] K. E. Petersen, IEEE Trans. Electron Devices **25**, 1241 (1978).

[6] P. M. Osterberg and S. D. Senturia, J. Microelectromech. S. **6**, 107 (1997).

Appendix A

Calculation of Refractive Index from Thin-Film Interference Measurement

The refractive index of thin-film materials can be determined by the interference measurement. A thin-film medium formed on a substrate can work as Fabry-Pérot etalon as shown in Fig. A.1. The optical path length difference ΔL of the reflected light can be described as

$$\begin{aligned} \Delta L &= n(\overline{\mathrm{AB}} + \overline{\mathrm{BC}}) - n_0\overline{\mathrm{AD}} \\ &= 2nd\cos\theta \end{aligned} \tag{A.1}$$

where n is the refractive index of the medium, n_0 is the refractive index of air, d is the thickness of the medium, and θ is the angle of refraction. The phase difference δ between each succeeding reflection is

$$\delta = \frac{2\pi\Delta L}{\lambda} = \frac{4\pi nd\cos\theta}{\lambda} \tag{A.2}$$

where λ is the wavelength of incident light.

The complex amplitude of each reflected light is given by X_i:

$$X_1 = r_1 A_\mathrm{i}, \quad X_2 = t_1 t_1' r_2' A_\mathrm{i} \mathrm{e}^{\mathrm{i}\delta}, \quad X_3 = t_1 t_1' r_1' r_2'^2 A_\mathrm{i} \mathrm{e}^{\mathrm{i}\delta}, \quad \cdots \tag{A.3}$$

The complex amplitude of incident light is given by A_i. r_1 and t_1 are the reflection and transmission coefficient of light propagating from air to the medium, respectively. r_1' and t_1' are the reflection and transmission coefficient of light propagating from the medium to air, respectively. The reflection coefficients of light propagating from the medium to substrate and the opposite are given by r_2 and r_2', respectively. Assuming $r_1 = -r_1'$, $r_2 = -r_2'$, and $r_1^2 + t_1 t_1' = 1$ (lossless mirror), the total complex amplitude of reflected light A_r can be described as

$$A_\mathrm{r} = \sum_i^\infty X_i = \frac{r_1 - r_2 \mathrm{e}^{\mathrm{i}\delta}}{1 - r_1 r_2 \mathrm{e}^{\mathrm{i}\delta}} A_\mathrm{i}. \tag{A.4}$$

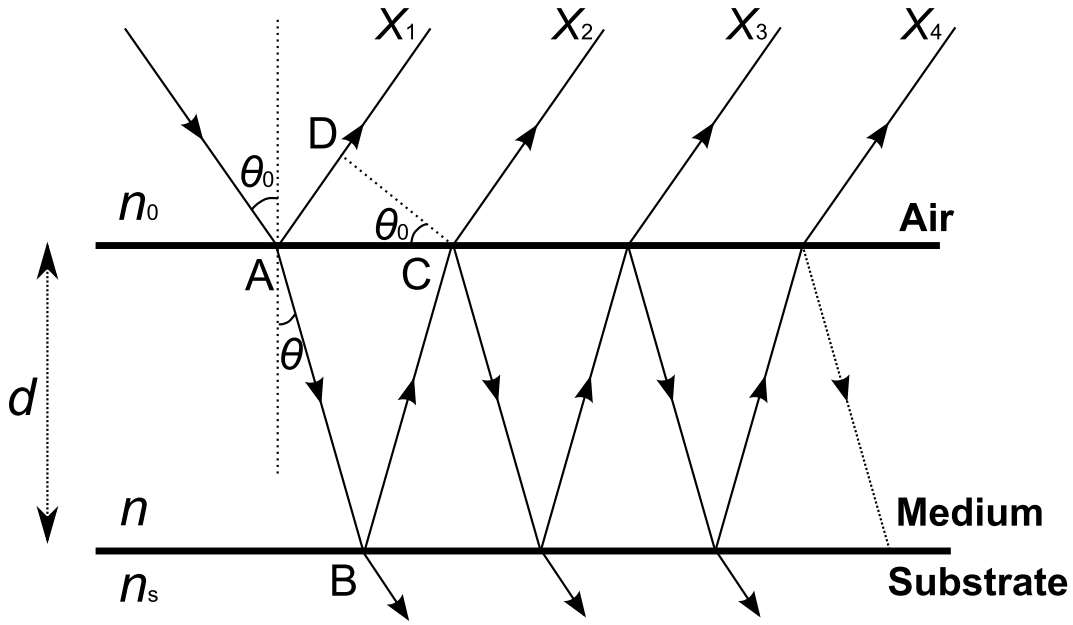

Figure A.1: Schematic drawing of thin-film interference. A thin-film medium is formed on a substrate. The light is transmitted or reflected at an interface. The air–medium and medium–substrate boundaries work as two parallel highly reflecting mirrors, and the medium become one-dimensional optical resonator, or Fabry-Pérot etalon.

The reflectance given by $I_\mathrm{r}/I_\mathrm{i}$, where I_r is the intensity of the reflected light and I_i is the intensity of the incident light, is expressed as the following equation:

$$\frac{I_\mathrm{r}}{I_\mathrm{i}} = \frac{A_\mathrm{r}A_\mathrm{r}^*}{A_\mathrm{i}A_\mathrm{i}^*} = \frac{r_1^2 + r_2^2 + 2r_1r_2\cos\delta}{1 + r_1^2r_2^2 + 2r_1r_2\cos\delta}. \tag{A.5}$$

A_r^* and A_i^* are the complex conjugate of A_r and A_i, respectively.

The reflectance will take maximal values at $\cos\delta = 1$ for $r_1r_2 > 0$ and at $\cos\delta = -1$ for $r_1r_2 < 0$. The reflection coefficient can be given by the Fresnel equations. Assuming a vertical-incidence configuration ($\theta_0 = \theta = 0$) and $n_0 = 1$, following equations can be derived [1]:

$$r_1 = \begin{cases} (1-n)/(1+n) & \text{(TE polarization)} \\ (n-1)/(n+1) & \text{(TM polarization)} \end{cases} \tag{A.6}$$

$$r_2 = \begin{cases} (n-n_\mathrm{s})/(n+n_\mathrm{s}) & \text{(TE polarization)} \\ (n_\mathrm{s}-n)/(n_\mathrm{s}+n) & \text{(TM polarization)} \end{cases} \tag{A.7}$$

where n_s is the refractive index of the substrate. For both TE and TM polarization, r_1r_2 will be positive when $n < n_\mathrm{s}$. Introducing $\cos\delta = 1$ or -1 into Eq. (A.2) with a vertical-incident configuration ($\theta = 0$), following equations can be obtained:

$$\lambda_{\mathrm{peak},m} = \begin{cases} 2nd/m & \text{for } n < n_\mathrm{s} \\ 4nd/(2m-1) & \text{for } n > n_\mathrm{s} \end{cases} \tag{A.8}$$

where m is the order of interference ($m = 1, 2, 3, \dots$) and $\lambda_{\mathrm{peak},m}$ is the peak wavelength of the interference. Similar to the maximum values, the reflectance given by Eq. (A.5) will take minimal values at $\cos\delta = -1$ for $r_1r_2 > 0$ and at $\cos\delta = 1$ for $r_1r_2 < 0$. Therefore the valley wavelength $\lambda_{\mathrm{valley},m}$ of the interference can be expressed as follow:

$$\lambda_{\mathrm{valley},m} = \begin{cases} 4nd/(2m-1) & \text{for } n < n_\mathrm{s} \\ 2nd/m & \text{for } n > n_\mathrm{s} \end{cases}. \tag{A.9}$$

Utilizing Eqs. (A.8) and (A.9), the refractive index of the medium can be calculated from the peak and valley wavelengths of the interference with the layer thickness.

References

[1] B. E. A. Saleh and M. C. Teich, *Fundamentals of Photonics (Japanese translation by Y. Ozaki and T. Asakura)* (Morikita Publishing, Tokyo, 2006).

Appendix B

Calculation of Optical Absorption from Transmission Measurement

Optical absorption spectra of materials can be determined by transmission measurement. When light is absorbed in passing through a medium which has parallel surface with a vertical-incidence configuration as shown in Fig. B.1, the optical absorption coefficient α of the medium is given by [1]

$$I_{\mathrm{t}} = I_{\mathrm{i}} \exp(-\alpha d) \tag{B.1}$$

where I_{t} is the intensity of transmitted light, I_{i} is the intensity of incident light, and d is the thickness of the medium. The transmittance T is given by

$$T = \frac{I_{\mathrm{t}}}{I_{\mathrm{i}}} = \exp(-\alpha d). \tag{B.2}$$

In the transmission measurement, the transmitted light is weakened by several factors, e.g., reflection and scattering at the surface. Especially, the reflection at the surface cannot be negligible when the surface is perfectly smooth. The reflectance R at the surface is given by [1]

$$R = \left(\frac{n - n_0}{n + n_0}\right)^2 \tag{B.3}$$

where n and n_0 are the refractive index of the medium and air, respectively. Considering a medium which is mirror polished on both sides, the reflection described in Eq. (B.3) will be occurred at both surfaces. Therefore, the transmittance of the medium can be expressed as

$$T = (1 - R)^2 \exp(-\alpha d). \tag{B.4}$$

To avoid the effect of the reflection and scattering at the surface on transmission measurement, measuring two or more samples with different thicknesses can be utilized. Since the optical loss of the reflection and scattering at the surface for each sample is same, the absorption coefficient of the medium can be determined by measuring the transmittance T_1

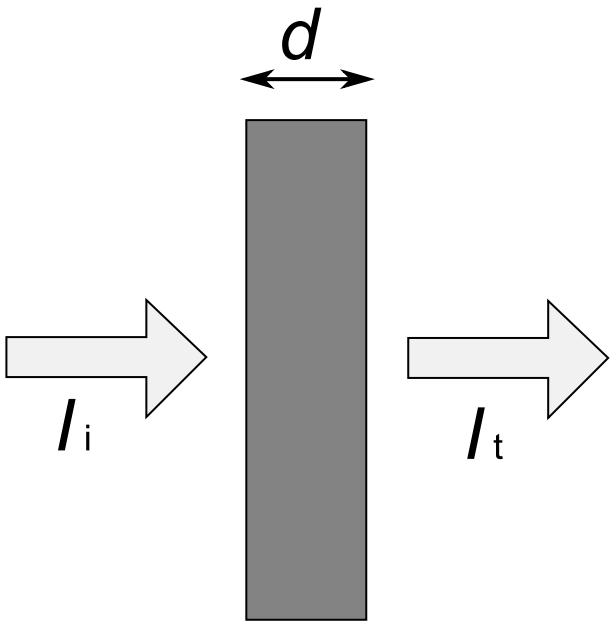

Figure B.1: Schematic drawing of optical transmission of a medium with parallel surface. The light is transmitted from a surface to the other. I_i is the intensity of incident light, I_t is the intensity of transmitted light, and d is the thickness of the medium.

of the sample with thickness d_1 and the transmittance T_2 of the sample with thickness d_2 as follows:

$$\begin{aligned}\frac{T_1}{T_2} &= \frac{(1-R)^2\exp(-\alpha d_1)}{(1-R)^2\exp(-\alpha d_2)} \\ &= \exp[-\alpha(d_1-d_2)].\end{aligned} \tag{B.5}$$

The absorption coefficient α is

$$\alpha = \frac{1}{d_2-d_1}\ln\left(\frac{T_1}{T_2}\right). \tag{B.6}$$

References

[1] B. E. A. Saleh and M. C. Teich, *Fundamentals of Photonics (Japanese translation by Y. Ozaki and T. Asakura)* (Morikita Publishing, Tokyo, 2006).

Appendix C

Mechanical Modeling of MEMS

C.1 Electrostatic Deformation of Suspended Bridge Structure

Electrostatic deformation of a double-clamped bridge structure can be approximated as a simple parallel-plate model in mass-spring system represented in Fig. C.1. The spring force F_{m} caused by the deformation of a bridge can be expressed as

$$F_{\mathrm{m}} = k\delta \tag{C.1}$$

where k is the spring constant and δ is the displacement. The Coulomb force F_{e} between two parallel plates is given by [1]

$$F_{\mathrm{e}} = \frac{\epsilon_0 V^2 S}{2(h-\delta)^2} \tag{C.2}$$

where ϵ_0 is the vacuum permittivity, V is the applied voltage, S is the area of a plate, and h is the distance between two plates. When F_{m} and F_{e} are equivalent, the parallel planes are steady-state with a certain displacement. Considering $F_{\mathrm{m}} = F_{\mathrm{e}}$, the following equation is obtained:

$$V^2 = \frac{2k}{\epsilon_0 S}\delta(h-\delta)^2. \tag{C.3}$$

From Eq. (C.3), V^2 can be plotted as a function of δ as shown in Fig. C.2. In Fig. C.2, the displacement is normalized by the distance between two plates h and the square of applied voltage is normalized by a constant $C = 2kh^3/\epsilon_0 S$. Since $\delta < h$, V^2 should be less than the value of the maximal at $\delta = h/3$. In other words, the parallel-plate model become unstable applying larger voltage than the voltage of $\delta = h/3$. This maximum safe-operating voltage can be expressed as

$$V_{\mathrm{p}} = \left(\frac{8}{27}\frac{kh^3}{\epsilon_0 S}\right)^{\frac{1}{2}}. \tag{C.4}$$

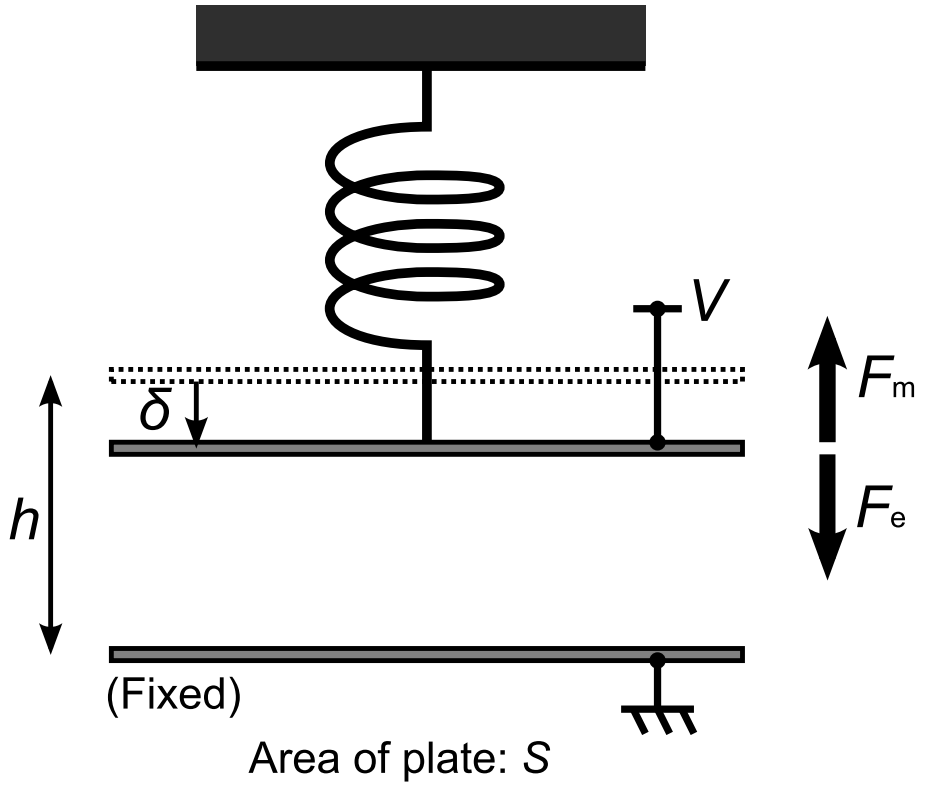

Figure C.1: Schematic drawing of electrostatic deformation in simple parallel-plate model considered as mass-spring system. The displacement δ of a movable plate (upper plate in this figure) at steady state is determined by the equilibrium between the spring force F_{m} and the Coulomb force F_{e}.

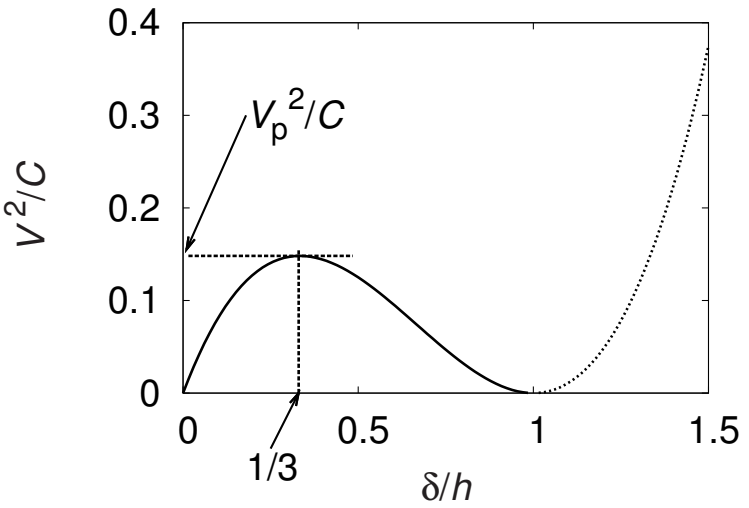

Figure C.2: Relation between the square of applied voltage V and the displacement δ of simple parallel-plate model. The displacement is normalized by the distance between two plates h and the square of applied voltage is normalized by a constant $C = 2kh^3/\epsilon_0 S$. Since $\delta < h$, V^2 should be less than V_{p}^2.

Now the flexural deformation of beam structures should be discussed. The deformation of the beam structure is governed by the following equation [1]:

$$\rho A\frac{\partial^2 u}{\partial t^2}-\mu\frac{\partial^2 u}{\partial y^2}+\frac{\partial^2}{\partial y^2}\left(EI\frac{\partial^2 u}{\partial y^2}\right)=f(y,t) \tag{C.5}$$

where ρ is the beam density, A is the cross-sectional area of the beam, u is the displacement of the beam, t is the time, μ is the tension in the beam, y is the axial coordinate, E is the Young's modulus, I is the cross-sectional area moment of inertia, and $f(y,t)$ is the load on the beam.

The steady-state deflection ($\partial u/\partial t=0$) of double-clamped bridge structures with uniform load as represented in Fig. C.3 can be expressed as

$$EI\frac{\partial^4 u}{\partial y^4}=-p \tag{C.6}$$

where p is the applied uniform load per length unit. Note that we assume $\mu=0$, i.e., neglecting the effects of tension in the bridge. As shown in Fig. C.3, both ends of the bridge at $y=0$ and $y=l$ are fixed, where l is the length of the bridge. The appropriate boundary conditions are

$$u(0)=\frac{\partial u}{\partial y}(0)=\frac{\partial u}{\partial y}(l/2)=\frac{\partial u}{\partial y}(l)=u(l)=0. \tag{C.7}$$

Integrating Eq. (C.6), the following equation can be obtained:

$$u(y)=-\frac{1}{24}\frac{p}{EI}y^4+\frac{c_0}{6}y^3+\frac{c_1}{2}y^2+c_2y+c_3. \tag{C.8}$$

$u(y)$ can be expressed as follow by applying the boundary conditions:

$$u(y)=-\frac{pl^4}{24EI}\left(\frac{y}{l}\right)^2\left(\frac{y}{l}-1\right)^2. \tag{C.9}$$

The displacement of the beam at the center, i.e., $\delta=-u(l/2)$ is

$$\delta=\frac{pl^4}{384EI}. \tag{C.10}$$

The cross-sectional area moment of inertia I for rectangle cross section can be expressed as [2]

$$I=\frac{wd^3}{12} \tag{C.11}$$

where w is the width and d is the thickness of the bridge. Therefore δ can be given by

$$\delta=\frac{pl^4}{32Ewd^3}. \tag{C.12}$$

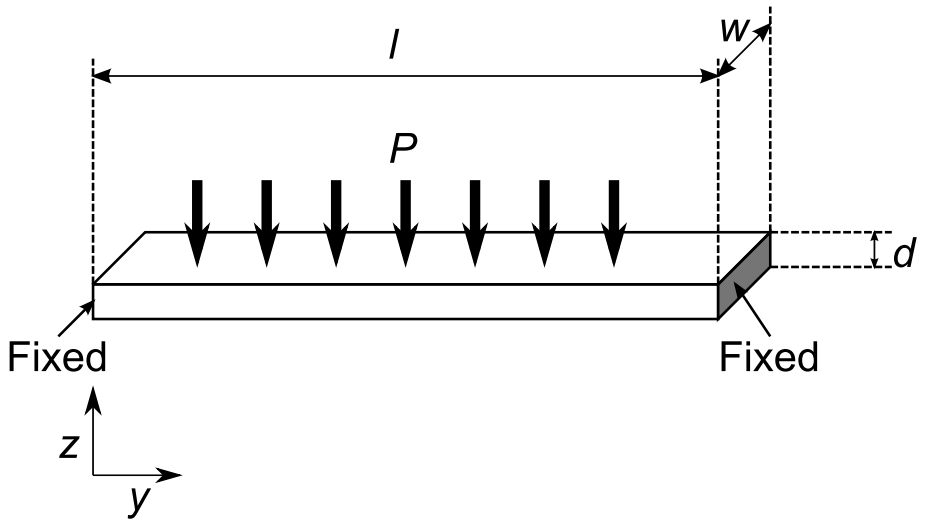

Figure C.3: Schematic drawing of double-clamped bridge with uniform load. The length, width, and thickness of the bridge are l, w, and d, respectively. P is the uniform load on the bridge.

Considering electrostatic deformation of the bridge, the applied load on the bridge $P = pl$ is equivalent to the Coulomb force as expressed in Eq. (C.2). Introducing F_{e} into Eq. (C.12), the following equation can be obtained:

$$\delta = \frac{1}{64}\frac{\epsilon_0 l^4}{d^3(h-\delta)^2 E}V^2. \tag{C.13}$$

When the displacement is the stability limit $\delta = h/3$, the applied voltage is given by this equation:

$$V_{\mathrm{p}} = \left(\frac{256 d^3 h^3 E}{27\epsilon_0 l^4}\right)^{\frac{1}{2}}. \tag{C.14}$$

C.2 Flexural Vibration of Beam Structure

Flexural Vibration of beam structures can be derived from Eq. (C.5). Assuming $\mu = 0$ and $f(y,t) = 0$, Eq. (C.5) can be written as

$$EI\frac{\partial^4 u}{\partial y^4} = -\rho A\frac{\partial^2 u}{\partial t^2}. \tag{C.15}$$

Assuming harmonic time dependence for the displacement, i.e., $u(y,t) = u(y)\exp(-j\omega t)$, the following differential equation should be satisfied:

$$\frac{\partial^4 u(y)}{\partial y^4} = \frac{\rho A}{EI}\omega^2 u(y). \tag{C.16}$$

Furthermore, assuming spatial dependence of the form $u(y) = \exp(\kappa y)$, the solutions will be $\kappa = \pm\beta, \pm j\beta$ where

$$\beta = \left(\frac{\rho A}{EI}\right)^{\frac{1}{4}}\omega^{\frac{1}{2}}. \tag{C.17}$$

Hence, the general solution in the term of real functions only will have the form

$$u(y) = C_1\cos(\beta y) + C_2\sin(\beta y) + C_3\cosh(\beta y) + C_4\sinh(\beta y). \tag{C.18}$$

The boundary conditions for the double-clamped bridge structure are

$$u(0) = \frac{\partial u}{\partial y}(0) = \frac{\partial u}{\partial y}(l) = u(l) = 0, \tag{C.19}$$

suggesting that $C_1 = -C_3$, $C_2 = -C_4$, and β should satisfy the following condition:

$$\cos(\beta_n l)\cosh(\beta_n l) - 1 = 0. \tag{C.20}$$

The solutions of β_n can be obtained numerically, with $\beta_n l = 4.730, 7.853, 10.996, 14.137, \ldots$ Note that $\beta_n l = 0$ is discarded since this solution is trivial. The corresponding frequencies, i.e., the resonant frequencies are given by

$$f_n = \frac{\omega_n}{2\pi} = \frac{\beta_n^2}{2\pi}\sqrt{\frac{EI}{\rho A}} = X_n \frac{d}{2\pi l^2}\sqrt{\frac{E}{\rho}} \tag{C.21}$$

where $X_n = (\beta_n l)^2/\sqrt{12}$.

As for single-clamped cantilever structures, the boundary conditions are

$$u(0) = \frac{\partial u}{\partial y}(0) = \frac{\partial^2 u}{\partial y^2}(l) = \frac{\partial^3 u}{\partial y^3}(l) = 0, \tag{C.22}$$

resulting in $C_1 = -C_3$ and $C_2 = -C_4$ in Eq. (C.18), and β should satisfy the following condition:

$$\cos(\beta_n l)\cosh(\beta_n l) + 1 = 0. \tag{C.23}$$

From the condition, the solutions $\beta_n l = 1.875, 4.694, 7.855, 10.996, \ldots$ for single-clamped cantilever structures can be derived. We can obtain the resonant frequencies of a cantilever structure by introducing these solutions into Eq. (C.21).

References

[1] J. A. Pelesko and D. H. Bernstein, *Modeling MEMS and NEMS*, (Chapman and Hall/CRC, Boca Raton, 2003).

[2] A. N. Cleland, *Foundations of Nanomechanics: From Solid-State Theory to Device Applications*, (Springer, Berlin, 2003).

List of Publications

A. Full Length Papers and Letters

1. Naoki Watanabe, Tsunenobu Kimoto, and Jun Suda, "The Temperature Dependence of the Refractive Indices of GaN and AlN from Room Temperature up to 515°C," J. Appl. Phys. **104**, 106101 (2008).

2. Jun Suda, Naoki Watanabe, Katsuhiko Fukunaga, and Tsunenobu Kimoto, "Electrostatic-Actuated Suspended Ribbon Structure Fabricated in Single-Crystalline SiC by Selective Photoelectrochemical Etching," Jpn. J. Appl. Phys. **48**, 111101 (2009).

3. Naoki Watanabe, Tsunenobu Kimoto, and Jun Suda, "4H-SiC pn Photodiodes with Temperature-Independent Photoresponse up to 300°C," Appl. Phys. Express **5**, 094101 (2012).

4. Naoki Watanabe, Tsunenobu Kimoto, and Jun Suda, "Thermo-Optic Coefficients of 4H-SiC, GaN, and AlN for Ultraviolet to Infrared Regions up to 500°C," Jpn. J. Appl. Phys. **51**, 112101 (2012).

5. Kohei Adachi, Naoki Watanabe, Hajime Okamoto, Hiroshi Yamaguchi, Tsunenobu Kimoto, and Jun Suda, "Single-Crystalline 4H-SiC Micro Cantilevers with a High Quality Factor," submitted to Appl. Phys. Express.

6. Naoki Watanabe, Tsunenobu Kimoto, and Jun Suda, "Temperature Dependence of Optical Absorption Coefficient of 4H- and 6H-SiC from Room Temperature up to 300°C," in preparation.

7. Naoki Watanabe, Tsunenobu Kimoto, and Jun Suda, "Temperature Dependence of Reverse Leakage Current up to 500°C in 4H-SiC pn Junction Mesa Diodes with Different Passivation Processes," in preparation.

B. Conference Proceedings

1. Naoki Watanabe, Tsunenobu Kimoto, and Jun Suda, "Temperature Dependence of the Refractive Indices of GaN and AlN up to 515°C," Phys. Stat. Sol. C **6**, S776 (2009).

2. Naoki Watanabe, Tsunenobu Kimoto, and Jun Suda, "Thermo-Optic Coefficients of SiC, GaN, and AlN up to 512°C from Infrared to Ultraviolet Region for Tunable Filter Applications," Proc. SPIE **7926**, 792604 (2011).

3. Naoki Watanabe, Tsunenobu Kimoto, and Jun Suda, "Fabrication of Electrostatic-Actuated Single-Crystalline 4H-SiC Bridge Structures by Photoelectrochemical Etching," Proc. SPIE **7926**, 79260B (2011).

C. Papers Presented at International Conferences

1. Naoki Watanabe, Tsunenobu Kimoto, and Jun Suda, "Temperature Dependence of the Refractive Indices of GaN and AlN up to 515°C," International Workshop on Nitride Semiconductors (IWN) 2008, We5-P15, Montreux, Switzerland, Oct. 2008.

2. Naoki Watanabe, Tsunenobu Kimoto, and Jun Suda, "Thermo-Optic Coefficients of SiC, GaN, and AlN up to 512°C from Infrared to Ultraviolet Region for Tunable Filter Applications," SPIE Photonics West 2011, 7926-03, San Francisco, California, USA, Jan. 2011.

3. Naoki Watanabe, Tsunenobu Kimoto, and Jun Suda, "Fabrication of Electrostatic-Actuated Single-Crystalline 4H-SiC Bridge Structures by Photoelectrochemical Etching," SPIE Photonics West 2011, 7926-11, San Francisco, California, USA, Jan. 2011.

4. Naoki Watanabe, Tsunenobu Kimoto, and Jun Suda, "Temperature-Independent Photoresponse in 4H-SiC pn Photodiodes by Applying Reverse-Bias Voltage," 2011 International Conference on Silicon Carbide and Related Materials (ICSCRM), Th-3B-2, Cleveland, Ohio, USA, Sept. 2011.

5. Naoki Watanabe, Tsunenobu Kimoto, and Jun Suda, "Optical Absorption Coefficients of 4H- and 6H-SiC at Elevated Temperatures for Photodetector Design," 9th European Conference on Silicon Carbide and Related Materials (ECSCRM), MoP-84, Saint Petersburg, Russia, Sept. 2012.